Universidade do Minho
Escola de Engenharia

Rafael Alexandre Antunes Vilarinho

Natural growth of light harvesting nanostructures from microalgae for bioinspired energy solutions

〈October〉, 〈2022〉

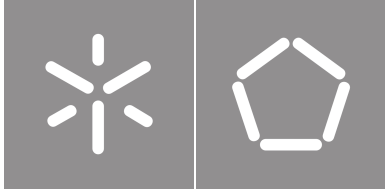

Universidade do Minho
Escola de Engenharia

Rafael Alexandre Antunes Vilarinho

Natural growth of light harvesting nanostructures from microalgae for bioinspired energy solutions

Master Thesis
Master in Physics Engineering
⟨Devices, Microsystems and Nanotechnologies⟩

Work developed under the supervision of:
Dr. Martin Lopez-Garcia
Dr. Mário Rui Cunha

⟨October⟩, ⟨2022⟩

Acknowledgements

To say that these past five years were tiresome would be an understatement. They were full of pain and hard work. Nonetheless, these five years have past and here I am now, writing my Thesis document.

I would like to thank my supervisors, Dr. Martín Lopez Garcia and Prof. Mário Rui Cunha Pereira for accompanying me through this journey and for their piece of advice and share of knowledge. It really improved my way of thinking and working during this year, while also opening the horizons for new challenges.

The whole Thesis was carried out at the International Iberian Nanotechnology Laboratory, INL, in a partnership with Universidade do Minho, which I take the opportunity to thank for the magnificent infrastructures and the wonderful stay, and let's hope one day I can come back. I would also like to thank Fundação para a Ciência e Tecnologia for support through grant no. PTDCBTA-8TA20612021, in the project NASCADIA - Natural Photonic Nanostructures: From Implications in Diatoms towards Next Generation Nanobiodevices, in which I also take the opportunity to thank Universidade de Aveiro.

To the NAPS group, Natural and Artificial Photonic Structures and Devices, where I was part of, I personally thank: Francisca Guedes for her knowledge in biochemistry and help in chemical experiments and expertise on how to be at a laboratory, Miguel Castillo for his tremendous knowledge in photonics and for the explanations about the setup and how to work with it, Pedro Braga for mutual sharing of information about diatoms and also for his patience on working with me in lots of useful measurements displayed throughout the document, and José Gama, a good old colleague of mine, whom also gave me advices and helped me integrate well on the group.

I cannot forget to thank Dr. Johannes Goessling for his expertise in diatoms and for providing me with so many tips and information that really helped me through the year, and also for supervising me in the NASCADIA project. The share of knowledge throughout this year was amazing. I would also like to thank Dr. Laura Rodriguez Lorenzo for providing the titanium dioxide nanoparticles and for helping with the DLS measurements.

Last, but certainly not the least, I would really like to thank my family for supporting me throughout, not only these five years, but through all my academic journey.

STATEMENT OF INTEGRITY

I hereby declare having conducted this academic work with integrity. I confirm that I have not used plagiarism or any form of undue use of information or falsification of results along the process leading to its elaboration.

I further declare that I have fully acknowledged the Code of Ethical Conduct of the Universidade do Minho.

_____, _____

(Place) (Date)

_____

(Rafael Alexandre Antunes Vilarinho)

"Learning never exhausts the mind." (Leonardo Da Vinci)

Abstract

Natural growth of light harvesting nanostructures from microalgae for bioinspired energy solutions

Light, the most widely available source of energy, enables the development of devices that are under constant studying of optimization and improvement. Nowadays, due to the miniaturization of components, nanoscale technologies are at an all-time high.

Photonic crystals, nanostructures characterized by defined periodic wavelength-scale patterns, e.g. pore lattices filled with a different refractive index than that of the bulk material, have the ability to manipulate light at ease. This periodicity induces a periodic dielectric function that gives rise to the so-called photonic bandgaps, a set of wavelengths/energies and crystallographic directions for which propagation within the photonic crystal is forbidden. Photonic crystals are commonly produced in cleanrooms involving precise nanofabrication techniques. The demand for a high reproducibility of such structures can, in a long term, become cost-unfriendly, not to mention the environmentally hazardous methods some techniques may require.

Recent researches confirmed that natural photonic crystals exist in the silicon dioxide exosqueletons of diatoms, abundant microalgae that precipitate silicid acid from water. This Thesis focuses on the study of a specific part of those exosqueletons: the girdles. The highly ordered lattices these structures exhibit create photonic bandgaps with preserved and well defined photonic properties, paving the way for their utilization as environmentally friendly photonic materials.

This Thesis shows, through theoretical and experimental studies, the preparation and modification of these photonic structures by tailoring the refractive index contrast with the deposition of higher refractive index materials, aiming to fine tuning of the photonic properties, thus presenting diatom biomass as a highly available photonic crystal with well preserved photonic properties.

Potential applications are not restricted to devices that rely on light, but also involving sensing by colorimetry or refractive index change detection.

Keywords: light, photonic crystals, nanoscale, wavelength, refractive index contrast, photonic bandgap, diatoms, girdles, biomass

Resumo

Crescimento natural de nano-estruturas de captação de luz a partir de microalgas para soluções energéticas bioinspiradas

Luz, a maior fonte de energia disponível, permite o desenvolvimento de dispositivos que se encontram sob estudo constante em termos de otimização e aprimoramento. Nos dias de hoje, devido à miniaturização de componentes, tecnologias à nano-escala têm se destacado cada vez mais.

Cristais fotónicos, nano-estruturas caracterizadas por padrões periódicos definidos à escala do comprimento de onda, por exemplo redes de poros preenchidas com um índice de refração diferente do material que compõe a estrutura, são capazes de facilmente manipular a luz. Esta periodicidade induz uma função dielétrica periódica que dá origem aos hiatos fotónicos, um intervalo de comprimentos de onda/energias e direções cristalográficas nos quais a propagação de luz no cristal fotónico é proíbida. Cristais fotónicos são regularmente produzidos em ambiente de sala limpa envolvendo técnicas de nanofabricação precisas. A exigência de elevada reprodutibilidade de tais estruturas pode, a longo prazo, tornar-se um processo dispendioso, para não falar dos métodos perigosos para o ambiente que algumas técnicas possam requerir.

Pesquisas recentes confirmaram a existência de cristais fotónicos naturais nos exoesqueletos de dióxido de silício de diatomáceas, microalgas abundantes que precipitam ácido silícico da água. Esta Tese foca-se no estudo de uma parte específica destes exoesqueletos: as girdles. As redes altamente ordenadas que estas estruturas exibem criam hiatos fotónicos com propriedades bem definidas e preservadas, abrindo caminho para a sua utilização como materiais fotónicos amigos do ambiente.

Esta Tese demonstra, com recurso a estudos teóricos e experimentais, a preparação e modificação destas estruturas periódicas através da modulação do contraste de índice de refração com deposição de materiais de elevado índice de refração, com o objetivo de modificar as propriedades fotónicas, e assim apresentar a biomassa proveniente de diatomáceas como cristais fotónicos altamente disponíveis e com propriedades fotónicas altamente preservadas.

As possíveis aplicações não se restringem apenas a dispositivos que trabalhem diretamente com luz, mas também envolvendo deteção por colorimetría a deteção de mudanças no índice de refração.

Palavras-chave: luz, cristais fotónicos, nano-escala, comprimento de onda, contraste de índice de refração, hiato fotónico, diatomáceas, girdles, biomassa

Contents

List of Figures

List of Tables

Glossary

Brownian Motion random movement from particles in a solution resultant from collisions with solvent molecules 75

chromophores region in a molecule responsible for its coloration. The resultant colour depends on the energy difference between two consecutive orbitals; when visible light hits the chromophore, an electron is excited to the upper energy level, with the released energy being equal to the colour observed. 1

complexes also designated light-harvesting complexes, are groups of chromophores responsible for photosynthesis 1

functionalization modification of the surface chemistry of a sample 41

Förster Resonance Energy Transfer mechanism that describes energy transfer between two chromophores. A donor chromophore in an electronic excited state transfers energy to an acceptor chromophore through non-radiative dipole-dipole coupling. 1

hydrodynamic size size of a sphere that diffuses at the same rate as the particle is being measured 75

plasma state of matter that contains a significant portion of charged particles, i.e. ions and/or electrons 77

polydispersity index measure of the heterogeneity of sizes of particles in a mixture. 42

slow-photon also known as slow light, is the propagation of an optical mode at a very low group velocity, due to interactions with the medium in which propagation takes place. 4, 16

zeta potential electrical potential difference between the dispersion medium and the stationary layer of fluid attached to the dispersed particle. 41

Acronyms

BPLCs blue-phase liquid crystals 6
BSE backscattered electrons 76

CCD charge-coupled device 36

DBR Distributed Bragg Reflector 3, 5
DLS Dynamic Light Scattering 41, 75
DSSC dye-sensitized solar cells 2, 8, 50

EDX Energy Dispersive X-Ray 34, 35, 42, 43, 45, 75, 77

FDTD Finite-Difference Time-Domain 11, 12, 21, 40, 43, 47, 50
FFT Fast Fourier Transform 34, 45
FIS Fourier Image Spectroscopy 35, 36, 49, 74
FWHM full width at half-maximum 18, 21, 22, 29

IBZ Irreducible Brillouin Zone 19

LC liquid crystals 6
LEDs light-emitting diodes 5
LUMO lowest unnocupied molecular orbital 1

NA numerical aperture 36, 37
NIR near infrared 9, 15, 18, 21, 22, 44
NPs nanoparticles 41, 42, 43, 44, 49, 51, 74

PBG photonic bandgap 19
PBGs photonic bandgaps 3, 4, 5, 6
PDDA poly(diallyldimethylammonium chloride) 42
PECVD Plasma-Enhanced Chemical Vapour Deposition 41, 45, 49, 77
PhC photonic crystal 4, 5, 6, 8, 10, 18, 19, 21, 22, 29, 50, 51
PhCs photonic crystals 3, 4, 5, 6, 9, 10, 11
pPBG pseudo-photonic bandgap 3, 9, 14, 15, 16, 18, 19, 20, 21, 22, 23, 24, 25, 29, 40, 43, 44, 47, 49, 50, 51

SE secondary electrons 76
SEM Scanning Electron Microscopy 13, 26, 34, 40, 42, 43, 45, 47, 75
SERS Surface Enhance Raman Spectroscopy 8
sPhC slab photonic crystal 5, 9, 15, 16, 18, 20, 22, 24, 29, 30, 36, 41, 44, 47, 50, 51
sPhCs slab photonic crystals 5

TFPV thin-film photovoltaics 2

VCELs vertical-cavity surface-emitting lasers 5

Symbols

Al	aluminum 42
$CaCO_3$	calcium carbonate 34
Cd	cadmium 2
CdTe	cadmium telluride 2
CIGS	copper indium gallium sellenide 2
CoFeB	cobalt iron boron 5
c-Si	crystalline silicon 2, 4, 50
GaAs	gallium arsenide 2
HCl	hydrochloric acid 34, 73
$KMnO_4$	potassium permanganate 33, 34, 73
NaCl	sodium chloride 42
$(COOH)_2$	oxalic acid 33, 34, 73
Pb	lead 3
Si	Silicon 14, 16, 18, 22, 24, 25, 51
Si_3N_4	Silicon Nitride 14, 16, 18, 20, 21, 22, 23, 24, 25, 41, 43, 45, 47, 49, 51, 77
H_2SO_4	sulphuric acid 33, 34

Ti titanium 42

TiO_2 Titanium Dioxide 14, 16, 18, 22, 24, 25, 41, 42, 43, 49, 51, 74

1 Introduction

1.1 What is light harvesting?

The planet gets constantly irradiated by a huge source of light, the Sun. Converting sunlight into energy provides an opportunity to make solar power a massive source of renewable energy, since the energy provided by the Sun is consumed worldwide [1]. Light harvesting, the ability some materials or systems (complexes) have to capture photons from solar light and convert them into chemical energy through photochemical processes [2], is the core of solar power conversion into usable energy and studies about the subject have been increasing throughout the years (see Figure 1.1).

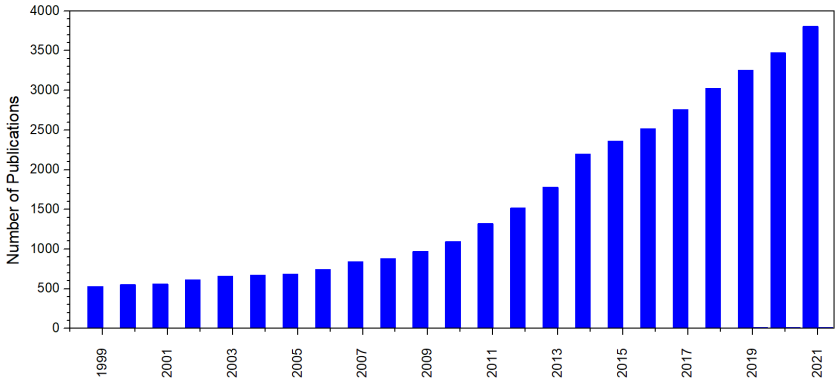

Figure 1.1: Evolution of the number of publications about the subject of "light harvesting". Data provided by Web Of Science.

Light harvesting is based in energy transfer from donor to acceptor molecules (chromophores). This principle is synthesized in Figure 1.2: the donor molecules act as antennas for the incoming excitation light. The absorbed photon will excite an electron with a certain spin orientation to a higher state and generate an exciton, a quasi-particle consisted of an electron and a hole attracted by Coulomb's force. The exciton is transported to a donor-acceptor heterojunction by Förster Resonance Energy Transfer (FRET) or by diffusion in donor and acceptor materials [3], in which it will be separated into an electron and a hole: the electron from the excited state, or the lowest unnocupied molecular orbital (LUMO), is transferred to the LUMO of the acceptor, resulting in the formation of electron-hole pairs.

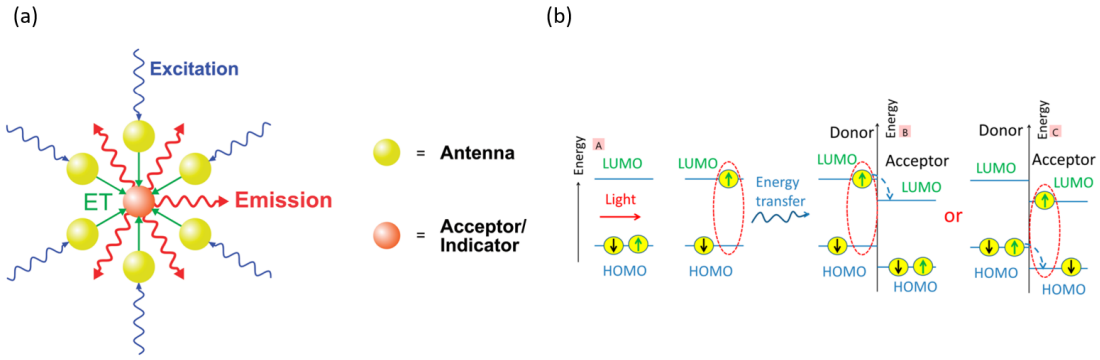

Figure 1.2: (a) Light harvesting principle. Reprinted from Mayr *et al* [2]. (b) Schematic of photoinduced electron transfer. Reprinted from Hedley *et al* [3]

The rate of electron transfer, k_{ET}, was studied in Li *et al* [4] and it was concluded that it decays exponencially with the distance between the donor and the acceptor, R_{DA}, decreasing the efficiency on light harvesting in the process:

$$k_{ET} = k_0 e^{-\beta R_{DA}} \tag{1.1}$$

where k_0 the electron transfer when the donor and acceptor are in contact and β is an attenuation coefficient. The efficiency on energy transfer in light harvesting systems/materials can be enhanced by decreasing this distance, for example reduce disorder in the system [5], or by increasing the donor-to-acceptor ratio, i.e. increasing the number of donor molecules per acceptor [6, 7]. Synthetic and photosynthetic biological systems capable of producing chemical energy from sunlight have a number of applications in photovoltaics such as photovoltaic systems that produce voltage and current upon photon absorption [8], brightness enhancement of luminescent sensors [2], improvement of dye-sensitized solar cells (DSSC) efficiency [9], photocatalysis in water splitting [10] and devices able to mimick photosynthesis [11].

Nowadays, solar technology devices are the mainstream generators of energy from incoming sunlight, in which the efficiency is directly related the the constituent solar cells [12]. Despite their ubiquitousness, solar cells can only convert a small percentage of light into usable energy. Conventional c-Si solar cell designs treat light as rays, giving different wavelengths the same treatment, in which the efficiency is way lower compared to the thermodynamic efficiency limit. One method to increase the efficiency of a solar cell is to increase its thickness in order to absorb more light; this, however, would result in increased bulk recombination [13], which would not contribute to energy conversion. In addition to limited efficiency values, ray-optics based solar cells are costly mainly due to the requirement of highly pure thick c-Si. An alternative to the silicon solar cells is thin-film photovoltaics (TFPV), or thin-film solar cells, with direct bandgap materials, such as GaAs [14], CIGS [15], CdTe [16] and perovskite [17], in contrast with silicon that an indirect bandgap. Although thinner, TFPV have yet to achieve an efficiency as great as conventional c-Si cells, not to mention the toxicity of materials such as Cd. The expensive nature of GaAs is also a downside on TFPV production, despite its high efficiency of 29.1% [14], and the slow production of CIGS is also a downgrade on the fabrication of these devices. Perovskite and organo-lead cells have shown efficiency increase throughout the years [18], with a multi-junction perovskite silicon tandem achieving

an efficiency record of 28.1% [13]. However, the low stability and environmental hazards associated with Pb overpower the advantages of perovskite cells. Hence, a new, less costly, low-loss, state-of-the-art approach to increase the efficiency is needed and the solution can be found on structures that treat specific wavelengths differently. This problem can be overcome by the implementation of photonic crystals (PhCs) [19].

1.2 Photonic Crystals

Photonic crystals are optical nanostructures composed by periodically separated regions of high and low refractive index in the wavelength scale. Discovered by E. Yablonovitch [20] and S. John [21] in 1987, although studied earlier by Lord Rayleigh in 1887, PhCs arouse high interest in optical and photonic applications due to their ability to control and manipulate light, as well as being low-loss dielectric media. Light propagation in a photonic crystal is affected by its properties: periodic refractive index, type of lattice, geometry and lattice parameter. The most interesting characteristic of PhCs is the existance of photonic bandgaps (PBGs), the gap between two adjacent photonic band structures caused by Bragg scattering when light passes through. Wavelengths within the range of the photonic bandgap are prohibited from propagating through certain directions of the crystal, due to destructive interferences resultant from multiple reflections at the high-low refractive index interfaces. PBGs can be divided into two types: full photonic bandgaps (Full PBGs), where a certain range of frequencies/wavelengths of any polarization cannot propagate in the crystal through any direction (also called omni-directional PBG) [22] and pseudo-photonic bandgap (pPBG), where the inhibition of mode propagation is restricted only to a certain direction. PBGs can be modulated by changing the parameters of the photonic crystal, such as the lattice constant, refractive indices of the constituent dielectrics and its thickness [23]. The concepts of PhCs are similar to those of conventional crystals, namely the wave treatment both light and electrons receive, respectively. Table 1.1 shows the main comparisons between both types of crystals [24, 25].

Table 1.1: Conventional crystals vs Photonic crystals

	Conventional Crystal	**Photonic Crystal**
Periodic arrangement	Atoms or Molecules	Macroscopic media
Periodic function	Periodic Potential Function	Periodic Dielectric Function
Differential equation	Schrödinger's Equation	Maxwell's Equations
Propagation	Electrons	Photons
Bandgap function	Electrons of certain energies cannot propagate in certain directions	Light of particular frequencies cannot propagate in some (if not all) directions

According to the direction of their periodicity, PhCs can be one-, two- or three-dimensional (see Figure 1.3). One-dimensional PhCs can be produced by thin-film depositions of two periodically stacked materials with different refractive indices; one example of this structure is the Distributed Bragg Reflector (DBR). The

resultant PBG of this structure is given only at a certain direction, normal to the surface of the material light is focused on. Two-dimensional PhCs are periodic in two dimensions and ideally infinite in the third; they may consist of rods of some material suspended in air or air-holes in a dielectric slab. This architecture of photonic crystal (PhC) is used in photonic crystal fibers [26]. Three-dimensional PhCs are capable to produce a full photonic bandgap, since modes within this range are prohibited to propagate in all directions. These types of PhCs can have many structures such as arranged inverse opals, woodpile and the Yablanovite, inverse cylindrical holes arranged in a diamond lattice, which showed the first 3D photonic bandgap in 1991 by E. Yablonovitch [27].

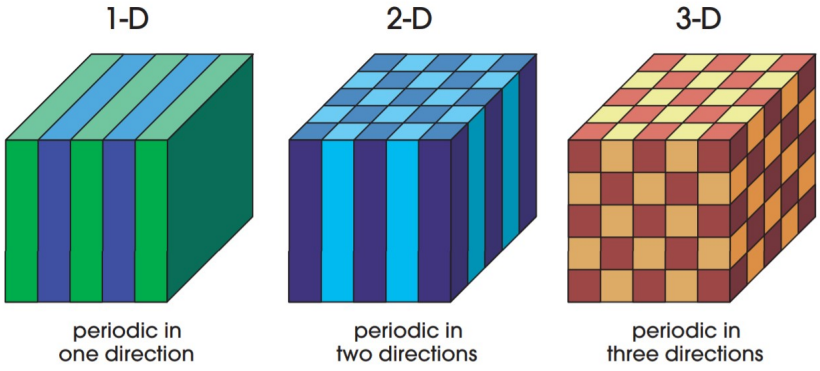

Figure 1.3: One-, two- and three-dimensional photonic crystals. Reprinted from Joannopoulos [28]

The use of PhCs in solar cells has been increasing throughout the years, not only due to reduced dimensions in contrast to thicker c-Si solar cells and decreased recombination but also due to PBGs and slow-photon effect [29]. Liu *et al* [22] displays and demonstrate the use of all three types of PhCs and their role in solar cells, such as back-reflectors in the case of one-dimensional PhCs, as well as a decrease in the rate of bulk recombination and increase the retention time of photons. A more efficient way to enhance light trapping in solar cells is the use of back-reflectors coupled to diffraction gratings from one- and two-dimensional PhCs, respectively, or with 3D inverse opals [12, 30, 31]. Studies were also made for 2D perovskite PhCs with the aim to enhance light absorption, with the main focus being solar cells [17]. Various photonic crystal patterns were also studied and demonstrated to increase solar cell efficiency, such as regular inverted pyramids [6, 32], surpassing the theoretical efficiency in silicon solar cells or Labertian limit, and the moth-eye pattern for an absorption enhancement in poorly illuminated environments [33]. Applications involving PhCs are not restricted only to light trapping-based devices; they can also be incorporated in sensing devices such as biosensors [34, 35], optical sensors [36] and even chemical sensors [37].

2D PhCs can be fabricated by injecting a two-dimensional periodic arrangement of a given refractive index into a planar dielectric that acts as a waveguide. Despite presenting advantages over 3D PhCs, such as easier fabrication processes and more compatible for integrated photonics and microelectronics, they are designed for in-plane control of light, but cannot control light in the perpendicular direction (out-of-plane), leading to diffraction losses [38].

Here enters a new type of PhC capable to manipulate light in three dimensions without a three-dimensional geometry designated 2.5 dimensional PhCs. These types of PhCs exhibit in-plane waveguiding like their 2D counterparts, as well as a two-dimensional PBG, but they can also control and confine light out-of-plane, i.e. in a direction perpendicular of propagation, like a 3D PhC, by index guiding, or total internal reflection. A very good example is shown in P. Viktorovitch *et al* [39], where a two-dimensional periodic membrane is coupled with a DBR, providing control of light in three directions. State-of-the-art 2.5D PhC, and even PhCs in general, for light confinement are the slab photonic crystals (sPhCs) [40]. A slab photonic crystal (sPhC) consists on a dielectric slab that acts as a waveguide over which a periodic arrangement, of a different refractive index, is patterned and responsible to modify light propagation and for the appearence of PBGs. The thickness of the slab plays a huge role in the detection of higher order modes, as well as the radius of the pores and the lattice constant of the periodic arrangement [41]. 2.5D PhCs have been studied for their use in laser applications such as in vertical-cavity surface-emitting lasers (VCELs) [42], ultra-thin photovoltaic cells [40], color-selective holograms for sensing [43] and efficiency enhancement for light-emitting diodes (LEDs) [44].

It is of great interest being able to manipulate the properties of a photonic crystal in order to tune the photonic bandgap to different wavelenghts, as well as to increase/narrow its bandwidth, therefore changing its photonic response. This can be obtained modifying its properties, such as its periodicity, the filling fraction and effective refractive index. The effective refractive index of a photonic crystal can by modulated by insertion of new materials in the structure [45, 46]. Figure 1.4 shows a 2D PhC consisting of nanoholes of aluminum with a deposited thin-film of CoFeB, with a higher refractive index, and the variation of the structural color as the thickness of the thin-film increases.

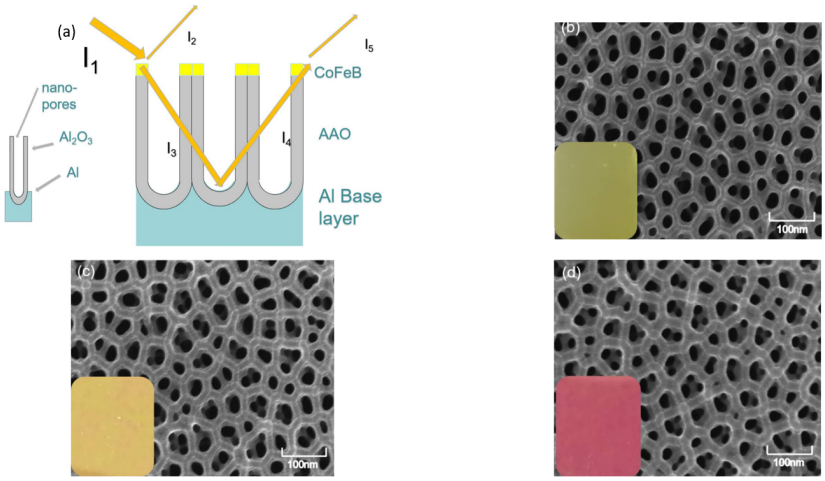

Figure 1.4: (a) Sketch of light path in CoFeb-coated aluminum oxide nanopores. SEM images for the aluminum oxide coated PhCs for different thicknesses: (b) 16.3 nm, (c) 32.7 nm and (d) 49.0 nm. Reprinted from Zhu *et al* [45].

A modification on the lattice constant was demonstrated in B. Suthar *et al* [47] in one-dimensional PhC by modifying the thickness of consecutive stacks, obtaining broader reflectances as well as significant shifts. Studies have also shown the tuning of PBGs by applying external stimuli of electrical fields on

charged colloids [48] and electric and magnetic fields alternate layers of silver and titanium dioxide [49]. Recent studies have demonstrated a dynamic control of PBGs in blue-phase liquid crystals (BPLCs) by applying electrical stimuli. BPLCs are a phase of liquid crystals (LC) with a periodic cubic lattice that exhibit selective reflection of visible light controlled by the orientation of light shining on different families of planes [50]. This selectivity is due to the anisotropic nature of LC molecules. The PBG is located in the visible range and its tuning can be dynamic by applying electrical stimuli, since LC molecules are also very responsive to electric fields [51]. R. Manda *et al* [52] prepared BPLCs consisting of a mixture of LC, a chiral dopant, a mesogenic monomer, a nonmesogenic monomer, and a chiral monomer. Controlling the concentration of chiral monomer concentration and LC-to-chiral dopant ratio, in addition to adjusting the electric field strength, allows the control of the PBG over a wide range with a high color purity (i.e. narrow bandwidths). This allows for dynamic tunable PBG materials that can be of great interest in tunable lenses [53] and gratings [54]. Liquid crystals are very sensitive to temperature changes, so that their properties may change and thus tuning the photonic response of the system. This study was demonstrated in R. Ozaki *et al* [55] for ferroelectric LC. Hydrogel photonic crystals also present great photonic tunability. Their periodicity can be modified through swelling and diswelling of the particles with the aid of external stimuli, like temperature for example, paving the way to fast responsive bio and chemical sensors. Park *et al* [56] achieved a rapidly tunable hydrogel photonic crystal highly reflective through the whole visible range.

Conventional PhCs are produced using nanofabrication techniques in cleanroom facilities, but they also exist in nature and can serve as models to be recreated as artificial PhCs with the same properties [57, 58]. Light harvesting structures with photonic crystal-like arrangements have been studied and demonstrated their behaviour in previous publications: the iridoplasts from *Begonia* plants, composed by periodic stacks of thylakoid tissues [59, 60], opal-like PhCs in brown algae [61] and naturally produced silica PhCs in diatom microalgae [62]. The latter is the case of study of this Thesis and is discussed in the next section. Some animals also present structures with PhC proterties, like the scales in some species of beetles [63], the wings of butterflies [64] and the scales of chameleons [65], albeit designed more towards structural coloring, camouflage, communication and UV protection rather than light harvesting itself.

1.3 Diatoms: what makes them special?

Diatoms are thought to have been in existence since the Jurassic period, i.e. for at least 200 million years [66]. They are a group of unicellular microscopic algae found in oceans, rivers and grasslands in the world, making up for a huge portion of the Earth's overall biomass [67]. Counting for at least 200 000 different species of various shapes (see Figure 1.5.a) [68], diatom microalgae produce about 20-50% of the oxygen produced on the planet every year [69]. The size of individual diatoms usually ranges from 2 to 200 µm [70]. Like plants, diatom microalgae harvest light to produce chemical energy through photosynthesis. Diatom microalgae possess a unique feature: they develop silica (SiO_2) exosqueletons (or shells),

called frustules, by precipitating silicic acid from water that, due to their highly porous nanostructures, are responsible for their coloration. There are two main morphologies of diatoms regarding the shape of the frustule: the elongated bilaterally-symetrical (or pennate) and the round and radially-symetrical (or centrics) [68]. The frustule is composed by two overlapped thecae (more commonly known as valves) in a Petri-dish-like orientation, with one being slightly larger than the other, and two silica bands called girdle bands, that hold the thecae together [68]. Figure 1.5.b shows a diatom from the species *Coscinodiscus granii* and its two different silica parts.

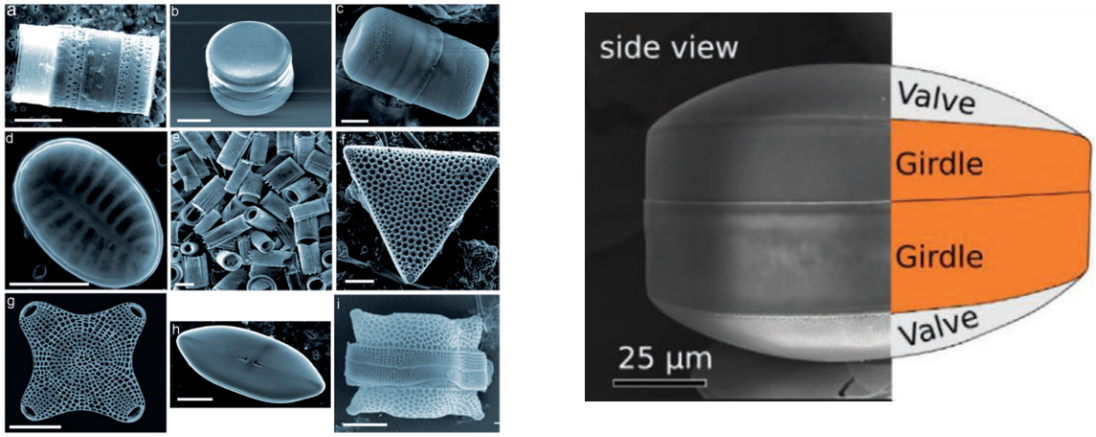

Figure 1.5: (a) Diverse shapes of diatom microalgae. (b) Side view of *Coscinodiscus granii* species, displaying the building blocks of the frustule: girdles and valves. Reprinted from [71] and [62], respectively.

In the presence of an adequate medium and enough sunlight, diatom cultures can double their population within 24 hours in the first stage of reproduction. Reproduction of diatom microalgae can be separated in two main stages: the asexual reproduction stage proceded by sexual reproduction (see Figure 1.6). First, diatoms undergo asexual reproduction, where the cell divides itself into two daughter cells with the same genetic information. Each daughter cell will inherit one theca from the mother cell, one with the epitheca (the larger one) and the other with the hypotheca (the smaller one), with each forming one girdle band (more can be formed over time) [72]. Cells that inherit the epitheca develop frustules that are always the same size of their mother cells', whereas frustules from the ones that inherit the hypotheca will be smaller than their predecessors. The stage of asexual reproduction will occur until the size of the frustule reaches a minimum. Henceforth, the cell undergoes sexual reproduction involving other cells by releasing gametes. This stage includes the formation of auxospores in order to restore the cell to the original size [73].

It was observed in previous studies that frustules provide high mechanical strength, being able to resist to stress values of 1-7 N mm^{-2} for valves, while also exhibiting high elasticity for girdle bands, capable of withstanding up to 560 N mm^{-2} of mechanical stress [72]. The pores also play a role in chemical communication with the environment, which would be of interest in microfluidic chips [74], and prevent harmful agends to enter the cell via size exclusion [62, 75]. The frustule has a highly periodic

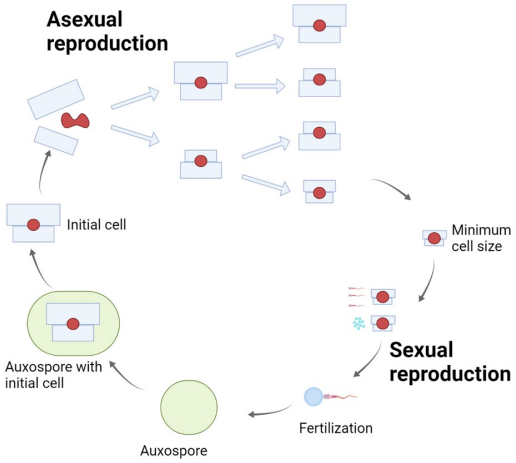

Figure 1.6: Reproduction cycle of diatoms

porous nature that plays a role in photosynthesis, as well as modulation of light-cell interactions [67], resembling photonic crystal nanostructures. These PhC-like properties make diatoms a huge source of nano-photonic materials, wether for direct use or for biomimetics. Diatom frustules have been incorporated in lots of applications over the years on account of on their good diffusion and scattering properties, using them as templates for electrodes for supercapacitors [76], incorporation in anodes for lithium-ion batteries [77], gain medium for random lasers [78], efficiency enhancement of DSSC [79], substrates for Surface Enhance Raman Spectroscopy (SERS) [80, 81], bio- and chemosensors [82, 83] and drug delivery systems [84]. T. Vasileiou *et al* [33] have used the hierarchical porous layers of frustules as designs for biomimetics for light absorption in triple junction solar cells. Valves (or thecae) display a hexagonal arrangement of pores with lattice parameter ranging from 900 to 950 nm [85]. Valve optical properties have had more focus due to their diffraction of light and intersting porous networks, composed by a hexagonal arrangement of pores in a hierarchical order. Girdle bands, however, have been largely understudied over the years. Studies from Goessling *et al* [62, 72] display comparisons of the optical properties between valves and girdle bands of the same species, *C. granii*, and a complete study of the optical properties of girdle bands, respectively. Girdle bands, or simply girdles, consist of circular silica slabs with radii ranging from 40 to 200 µm for the species *C. granii*. Girdles present intriguing features in their morphology: they are composed by a periodic lattice of inter-connected cylindrical micropores that perforate the bulk silica slab, intersecting a central rhombic chamber (see Figure 1.7.b). The most known periodic arrangements are the square and hexagonal lattices for the species *C. granii* and *C. wailesii* respectively [86]. It has been shown in Goessling *et al* [62] that the periodicity for *C. granii* species is about 285 nm, with a surface area of 7500 μm^2 and a slab thickness between 745 and 800 nm. An intersting feature regarding the porosity network of diatoms is that the periodicity, otherwise known as lattice constant, is highly preserved within a certain species, but changes for different species. For the species *C. wailesii* the lattice constant was measured to be about 330 nm [86]. The volume occupied by the micropores accounts for 25-30 % of a unit cell and defines the void that will be filled with medium, i.e.

the void filling fraction f_i. The void filling fraction will cause refractive index contrast relatively to the bulk silica, consequently manipulating the photonic response of the system by changing the effective refractive index of the girdle band, n_{eff}, as stated by Equation 1.2:

$$n_{eff} = \sqrt{f_i n_i^2 + (1 - f_i) n_{bulk}^2} \tag{1.2}$$

where n_{bulk} is the effective refractive index of the bulk girdle band. The internal structure and material

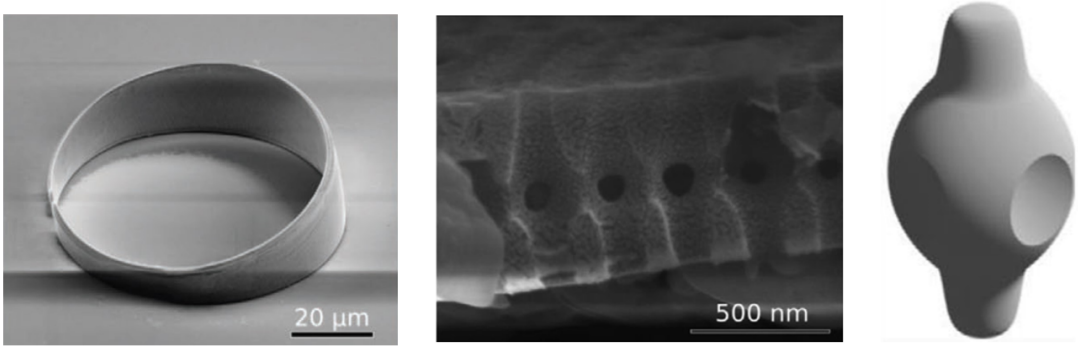

(a) (b) (c)

Figure 1.7: Girdle band morphology. (a) Circular shape with a split ring spacing. (b) Cross section of the pores. (c) 3D model displaying the volume occupied by one pore (void filling fraction). Reprinted from [62].

properties of the girdle slab show interesting photonic response when immersed in water, i.e. at low refractive index contrast showing the existence of a pPBG in the near infrared (NIR) region when light is incident at normal incidence, as well as a blue-shift at larger angles, as seen in Goessling *et al* [62]. The existence of a pPBG and in-plane diffraction of modes due to the waveguiding nature of the bulk silica slab promotes girdle bands as an example of naturally produced 2.5 dimensional sPhC. To tune the photonic response of the system independently of the immersion medium, the bulk of the girdle band must be modified in order to change its effective refractive index, changing in the process the effective refractive index of the sPhC. The position of the pPBG, described by the central wavelength of the reflectance peak shows a dependence not only on the effective refractive index of the sPhC but also on the angle of incidence, the distance between planes where light is focusing on and the immersion medium. These dependences are described by Bragg-Snell's Law for PhCs [87]:

$$\lambda_c = 2D\sqrt{n_{eff}^2 - n_i^2 \sin^2 \theta_{in}} \tag{1.3}$$

where λ_c is the central wavelength of the reflectance peak and the spectral position of the pPBG, D is the interplanar spacing, n_{eff} is the effective refractive index of the sPhC, n_i the refractive index of the immersion medium and θ_{in} is the angle of incidence.

1.4 Framing and Motivation

Notwithstanding the usefulness of photonic crystals in light trapping devices like solar cells, the high need of reproduction may turn out to be an inconvinience. The fabrication of PhCs for these devices involves advanced cleanroom processes, not to mention the precision and accuracy on desired dimensions, which can become time-consuming and costly in the long run. An eco-friendly alternative like microalgae biomass would certainly be an improvement in the production of energy from renewable sources as, aside from being already an improvement from fossil fuels, it would be an upgrade from conventional solar cells and cells incorporated with nano-fabricated PhCs.

The motivation of this Thesis is to present a new material with PhC properties made of microalgae biomass, girdle bands from diatoms, as an alternative to fabricated PhCs and therefore open a window for their use in light harvesting devices, while also being environmentally-friendly as well as less costly. To date, there have been no technological devices where girdle bands are implemented due to the existence of very few studies on the subject.

1.5 Objectives

This Master Thesis aims to enhance light harvesting in diatom girdles by tailoring the refractive index contrast of said structures. For such, the following steps will be performed:

- **Step 1:** the first step of this project will be based on simulating the photonic response of modified diatom girdles, i.e. funcitonalized with other materials, with the approximated dimensions (discussed in Chapter 2);
- **Step 2:** measure the photonic response of clean girdle bands, i.e. without any modification made whatsoever;
- **Step 3:** use of diatom girdles as scaffolds for either the growth of conformal optical materials in the cleanroom or functionalization with nanoparticles, in a way to fine tune experimentally its intrinsic optical properties;
- **Step 4:** study the photonic response with the resulting samples from Step 3.

1.6 Structure

The present Thesis document is composed by four chapters with the following descriptions:

- **Chapter 1:** this chapter corresponds to the introduction of the Thesis. It consists of briefly explaining the concept of light-harvesting and some state-of-the-art technologies using photonic crystals as

light-trapping structures. It also introduces diatoms and the potential they have to replace conventional PhCs according to previous works and studies.

- **Chapter 2:** this chapter is relative to the theoretical study of the photonic response of girdle bands when higher refractive index materials of choice are inserted, via Finite-Difference Time-Domain (FDTD) simulations. The simulation setup is explained with detail, as well as how the various simulations are computed.

- **Chapter 3:** this chapter corresponds to the experimental section of the Thesis. It contains the optical and morphological characterizations of bare and modified girdle bands, as well as the processes of modification of these structures. The treatment of diatoms, such as culture nurturing and frustule cleanign processes, are also included.

- **Chapter 4:** this chapter is about the conclusions taken from the overall Thesis and future perspectives regarding the corresponding subject.

2

Theoretical Study of the Photonic Response

This Chapter shows simulations of the photonic response of a girdle-like structure with and without inserted materials, which will be called bare and coated structures, respectively. It is to point out that these simulations were executed before real measurements were carried out and thus some dimensions and results will differ slightly from the ones measured in Chapter 3. Furthermore, as it will be seen in Section 2.2.2, the explanation of the photonic response of a modified structure is given for only one material with one specific thickness, aside from comparisons with other thicknesses and materials also simulated; the remaining simulations are displayed in Appendix A.

2.1 Simulation Setup

As seen in Chapter 1, diatom girdles are circular silica slabs with a periodic arrangement of pores that display a complex geometry (see Figure 1.7). The lattice, characterized by an intrinsic lattice constant, $a = |\vec{a}|$, gives rise to a periodic dielectric function in the structure, $\epsilon(\vec{r}) = \epsilon(\vec{r}+\vec{a})$, where $\vec{r}$ is the position of some point in the lattice.

The system's optical properties are related to its effective refractive index [28, 62] which can be tuned by altering the surface of the bulk silica slab, by introducing new materials all over the surface and inside the pores, for example. The deposited material will change the girdle's effective refractive index, altering the refractive index contrast between the bulk and the surrounding medium (which can be air, water or other fluid) in the process.

To study the photonic response of the system toward a change in the refractive index contrast, Finite-Difference Time-Domain (FDTD) numerical methods from the commercial tool Lumerical were used to simulate these properties on a girdle-like structure with some inserted material of a given thickness. The girdle-like structure was built knowing that it consists of a silica slab with periodically separated pores: the slab corresponds to a silica rectangle (n_{SiO_2} = 1.44), with a thickness of approximately 800 nm. Dimensions used in these simulations are based on previous works that simulated the same structure [62]. The pores were considered to be cylinders intersecting spheres, with radii of 91 and 176 nm, respectively.

The lattice constant was considered to be 285 nm, the average value of the *C. granii* species, whose girdle bands exhibit a square lattice and the main case of study of this Thesis.

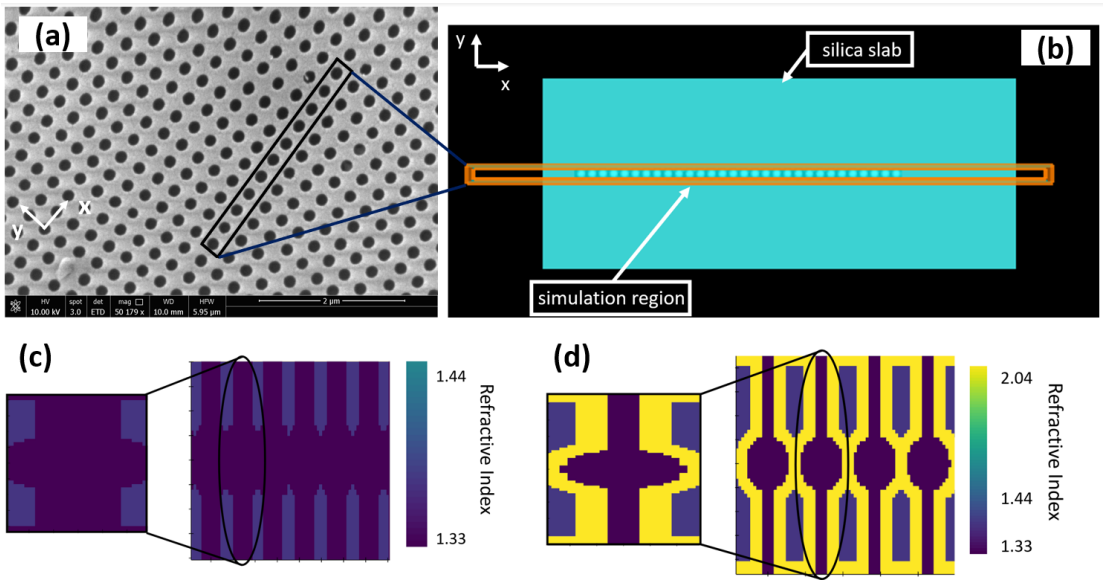

Figure 2.1: Girdle-like structure. (a) SEM view of a real girdle band, displaying its 2D arrangement of pores. (b) Top view of the girdle-like structure. Cross section view in the XZ-plane of the structure, with water as the immersion medium, displaying one unit cell: (c) bare structure (purple corresponds to water and dark-blue to silica. (d) structure with deposited material with Si_3N_4 (purple corresponds to water, dark-blue to silica and yellow to Si_3N_4.

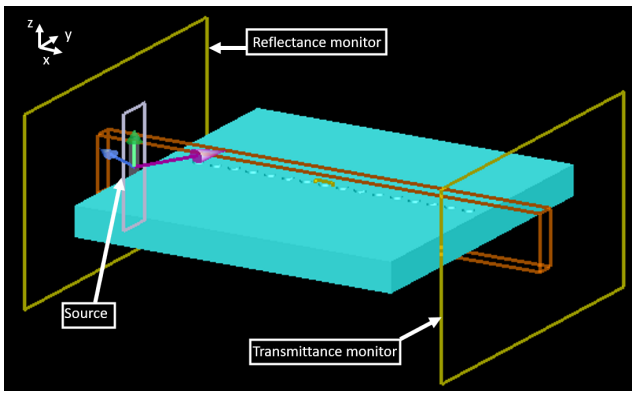

Figure 2.2: Full simulation setup.

Figure 2.1.a shows a Scanning Electron Microscopy (SEM) image of a flat girdle band and Figure 2.1.b displays the top-view of the girdle-like structure and the orange stripe corresponds to the simulation region. The simulation region has the same width as the structure's periodicity and has Bloch Boundary conditions on the $y-$direction in order to replicate the array of pores throughout the slab in the $+y$ and $-y$ directions, thus inducing a 2D lattice with less simulation running time; $z-$ and $x-$directions have PML layers on the respective ends in order for radiation to vanish and mitigate the effect of back-reflectances. Figure 2.1.c shows the cross section of a set of pores from the structure as well as a refractive index gradient, showing all constituents: the bulk silica (n_{SiO_2} = 1.44) in dark-blue and water (n_{H_2O} = 1.33) in purple, acting as

the surrounding medium. Building a structure with a deposited material in it follows the same steps as building the bare one; however the thickness of the material must be considered, considering a conformal deposition. For example, for a 60 nm thick film, the slab with the material will have to be 60 nm thicker than the silica's upwards and downwards, as well as the dimensions of the pores. Figure 2.1.d shows a cross sectional view in the XZ-plane of a structure with a 60 nm thick conformal film of Si_3N_4 deposited over the surface and inside the pores: water in purple, silica in dark-blue and Si_3N_4 in yellow. It is clear the difference in the refractive indices of all materials. With this configuration, a periodicity in the dielectric function in the structure is ensured.

Figure 2.2 displays the full setup used for the simulations. Monitors collect the electric and magnetic fields, $\vec{E}$ and $\vec{H}$, respectively, normalized by the source and display the photonic response given by the system when light is incident. Reflectance and transmittance monitors must be large enough and placed not to distantly from both ends of the structure, in order to capture a considerable amount of radiation, providing conclusive results in the end. The electric field monitor is placed in a pore right in the middle of the structure. The positioning of this monitor is simply because it is desired to analyze the behaviour of radiation inside the structure, where in the first pore light will not have enough time to be influenced by the structure, whereas in the last pore the radiation will not be enough, since it will be lost throughout the whole structure.

2.2 Results

Simulations for reflectance and transmittance at normal incidence were carried out in order to study the properties of the pseudo-photonic bandgap (pPBG), such as its spectral position and width. The amount of electric field localized in a single pore in the structure is also simulated, in order to visualize the regions where it concentrates the most to further understand the pPBG region; this will also act as a way to determine the material thickness that enhances the localized field on the structure. The angular reflectance is also simulated to detect the shift of the central peak with light focusing at various angles of incidence.

Three materials with different refractive indices were used in these simulations to study the different photonic responses: Si_3N_4, TiO_2 and Si, with refractive indices of 2.04, 2.59 and 3.86, respectively, at $\lambda = 625$ nm (values were calculated from the respective dispersion formulas displayed in Appendix A. Dispersion formulas for each material were retrieved from K. Luke *et al* [88], J. R. DeVore [89] and B. Tatian [90], respectively). The thickness of these materials was also varied in order to study the effect of thickness variation on a fixed inserted material; values of 6, 30 and 60 nm were simulated (low, average and high material concentration, respectively). Higher values were not considered since the narrower regions of the pores would have been completely filled.

Simulations for the species *C. wailesii*, whose girdle bands exhibit hexagonal/triangular lattices, are also carried out in order to study the effect of lattice geometry on the photonic response of the system, as

well as to briefly study its photonic properties.

Finally bandstructures are also computed, as mentioned above, by placing a set of randomly distributed dipoles over a single unit cell of the structure with frequencies ranging from 60 to 700 THz in order to cover the whole visible spectrum and the near infrared (NIR). Bandstructures give a more complete analysis on the existence of the pPBG not only at normal incidence but also at a certain angle of incidence due to the waveguiding nature of the slab photonic crystal (sPhC) structure, as well as the optical modes that it can support. The bandstructures are calculated considering the complexity of the pores as regular cylinders that occupy 30% of a unit cell, as real pores do, with an effective refractive index that takes into account the weights of the deposited material and immersion medium (see Appendix A for the explanation).

2.2.1 Bare girdle band

First, simulations were performed for a bare girdle-like structure, i.e. without any material inserted and immersed in water. Figures 2.3.a and 2.3.b show the reflectance at normal incidence and at variable incident angle, respectively.

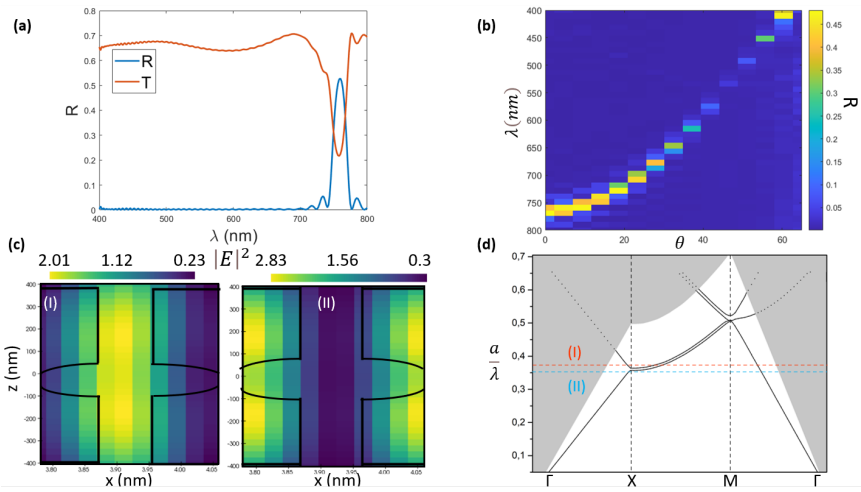

Figure 2.3: Simulated photonic response of a bare girdle immersed in water: (a) Reflectance (blue) and transmittance (orange) at normal incidence. The pPBG is displayed as a peak/dip in the reflectance/transmittance spectrum. (b) Angle-dependent reflectance. (c) Electric field intensity at high (I) and low (I) energy positions of the pPBG. (d) Bandstructure of the system displaying guided modes (solid lines) and modes that couple with radiation modes (dashed lines).

At normal incidence, the pPBG, given by the peak/dip on the reflectance/transmittance spectrum is located at approximately $\lambda = 760$ nm, in the NIR. The angular reflectance shows that the pPBG blue-shifts as the angle of incidence increases, in accordance the Bragg-Snell's equation (Equation 1.3). From this contour plot, for each angle that was computed in the simulation, the central wavelength at the reflectance peak was plotted and a linear fit was executed in order to obtain the effective refractive index of the sPhC, which was about 1.37. Figure 2.3.c shows the intensity of the electric field on a single pore

in the structure at the band edges of the pPBG: at high energy, $\lambda_+ = 744.1$ nm, in Figure 2.3.c.(I) and at low energy, $\lambda_- = 772.9$ nm, in Figure 2.3.c.(II), corresponding to normalized frequencies of $\omega_+ \approx 0.383$ and $\omega_- \approx 0.369$, respectively. The intensity of the electric field inside the pores is enhanced due to its confinement by total internal reflections. The colorbar corresponds to the ratio between the incident and absorbed electric fields, $|E_i|^2$ and $|E_o|^2$, respectively. At low energy, fields tend to stay in regions where the refractive index is higher, in this case where the silica is located (yellowish regions), and fields of lower intensity reside on regions where the refractive index is lower, like in water (blue/dark-blue regions). This fact is mathematically predicted by the electromagnetic variational theorem (Equation 2.1), which states that a mode on its fundamental state of energy, ω_0^2/c^2, concentrates a great portion of its electric field energy at regions where the dielectric function is higher in order to minimize its frequency [28]. This state is designated by dielectric band due to the aforementioned fact, and correspondes to the lowest mode on the bandstructure of the system. Similarly, the mode above is called air band, a mode of higher energy where the electric field is mostly concentrated in the lowest refractive index regions.

$$\left(\frac{\omega_0}{c}\right)^2 = \frac{\int \left|(\nabla \times \vec{E}(\vec{r}))\right|^2 d^3\vec{r}}{\int \epsilon(\vec{r})|\vec{E}(\vec{r})|^2 d^3\vec{r}} \tag{2.1}$$

The confinement of light is higher at the band edges due to the slow-photon effect, where the group velocity of guided modes tends to vanish due to a flattening in the bandstructure. This flattening happens at the symmetry point X, shown in Figure 2.3.d. Light being shone at normal incidence corresponds to the $\Gamma - X$ direction in the bandstructure. At the vicinity of point X the modes start to flatten and open a gap that correponds the pPBG present in the reflectance and transmittance simulation. From the bandstructure is possible to see that the structure supports a set of modes outside the light cone (white area), depicted by solid lines. These modes represent guided modes and are totally confined within the slab. In addition, there are also modes that lie inside the light cone, given by the dashed lines. This plot also displays the frequencies at which the electric fields of Figure 2.3.c were calculated: the dashed orange line corresponds to ω_+, which lies at the air band, and the blue dashed line to ω_-, which lies in the dielectric band. These modes are characteristic of 2.5D sPhC and can couple with radiation modes (from the outside), presenting a so-called leaky mode, with a finite lifetime.

2.2.2 Girdle band with material deposited

The simulation performed for a 30 nm thick film of Si_3N_4 will serve as a base to explain the photonic response of a girdle-like structre when deposited with a material. This thickness is chosen for the study since it gave more conclusive results, which facilitated the analysis of the photonic response relative to 6 and 60 nm. Si_3N_4 also has a relatively low refractive index (although higher than silica's), so that some effects that are seen in simulations for TiO_2 and Si are not manifested here in high extent, making analysis easier to understand.

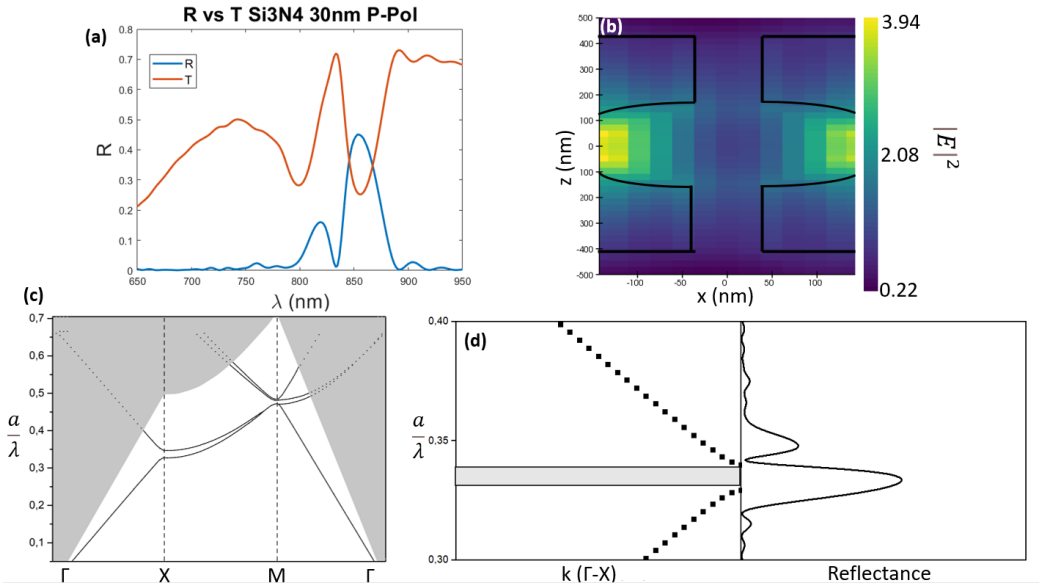

Figure 2.4: Simulated photonic response of a girdle band with a deposition of 30 nm of Si_3N_4. Incident light is *p*-polarized with water as the immersion medium. (a) Reflectance (blue) and transmittance (orange) at normal incidence. (b) Intensity electric field confined in one pore. (c) Guided TE modes along the IBZ (solid lines) and modes that couple to radiation modes (dashed lines). (d) Mapping between the dispersion relation in the $\Gamma - X$ direction and reflectance.

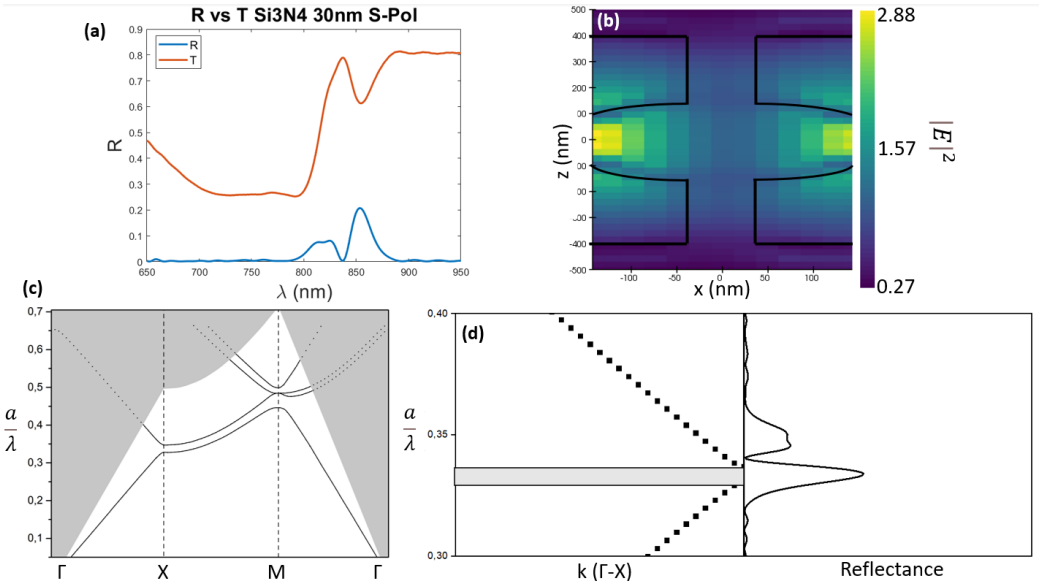

Figure 2.5: Simulated photonic response of a girdle band with a deposition of 30 nm of Si_3N_4 with water as the immersion medium. Incident light is *s*-polarized. (a) Reflectance (blue) and transmittance (orange) at normal incidence. (b) Intensity electric field confined in one pore. (c) Guided TM modes along the IBZ (solid lines) and modes that couple to radiation modes (dashed lines). (d) Mapping between the dispersion relation in the $\Gamma - X$ direction and reflectance.

Figures 2.4 and 2.5 show the simulated photonic response of the system at normal incidence for *p*- and *s*-polarization, respectively. The source is a plane wave, with wavelengths ranging from the whole visible spectrum and covering a small portion of the NIR. For simulations with TiO_2 and Si coatings, wavelengths cover mostly the NIR due to the resultant shifts to higher wavelengths (see Appendix A). The type of polarization light has is characterized by the polarization angle. This angle defines the orientation of the injected electric field and is measured with respect to the plane formed by the direction of propagation and the normal to the injection plane. Polarization angles of $0°$ and $90°$ define *p*- and *s*-polarized radiation, respectively (see Figure 2.6.a).

Figures 2.4.a and 2.5.a display the spectral position of the pPBG, depicted by peaks/dips in the reflectance/transmittance spectra. The pPBG for the coated girdle band structure at *p*-polarized light is located at $\lambda_c = 857.0$ nm and the one at *s*-polarization at $\lambda_c = 854.9$ nm; these values correspond to the central wavelength of the reflectance peak. In a perfect 2D photonic crystal (PhC), these values would have been the same; this dissimilarity is due to the asymmetry existant in the structure when the material is inserted and this effect is higher for higher refractive index materials (see Appendix A). Real girdle bands exhibit asymmetries even without inserted materials, mainly due to the existance of defects, which were not considered in this theoretical study. The pPBG for *p*-polarization also seems to be wider, with a full width at half-maximum (FWHM) of approximately 26 nm, while for *s*-polarization the FWHM is around 16.5 nm, inhibiting therefore a wider range of wavelengths/frequencies to propagate through the crystal. These values were calculated using a Gaussian fit, with two iterations from *OriginPro* software. The insertion of Si_3N_4 on the structure red-shifts the pPBG to higher wavelengths in the spectrum about 90 nm relatively to the bare structure, seen in the previous subsection, due to increasing the effective refractive index of the sPhC. The aforementioned graphs present a smaller peak adjacent to the pPBG. These can be designated as secondary oscillations, and may be interpreted as a result of back-reflections at both ends of structure, as well as a net of total internal reflections inside the structure. This effect is sensible to higher refractive index contrasts [62] and may have the same properties as the pPBG, which is further discussed in simulations at oblique incidence in Subsection 2.2.5. The intensity of the electric field on a single pore located in the middle of the structure is shown in Figures 2.4.b and 2.5.b. These plots were taken at wavelengths in which the confined electric field on the pore was maximum, at low energy near the band-edges of the respective pPBG as previously seen in the bare girdle structure. The electric field is enhanced relatively to the bare sample since the insertion of Si_3N_4 will increase the refractive index contrast, which in turn will increase the amount of total internal reflections inside the pores, and therefore the confinement of light will also increase. It is apparent the gradient of localized field throughout the pore. The electric field seems to concentrate its energy at the edges of the pore, i.e. the pore-pore interface, that is covered by Si_3N_4, agreeing with the electromagnetic variational theorem since the dielectric function is higher at these regions.

Figures 2.4.c and 2.5.c show TM and TE modes propagating in the structure, i.e. guided modes, respectively, represented by solid lines. The vertical axis represents energy in reduced units of a/λ, where a is the lattice constant and λ the wavelength of light in vacuum, while the horizontal axis corresponds to the

set of all wavevectors from the reciprocal space that belong to the square lattice's Irreducible Brillouin Zone (IBZ)(Figure 2.7.a). It is important to mention that, while TM and TE modes are usually associated with *p*- and *s*-polarization, respectively, in a PhC this convention is the other way around: TE modes are those where E-fields oscillate in the direction where the PhC is infinite, i.e. in-plane, while in TM modes E-fields oscillate in the direction of the height of the crystal (in this case, the thickness of the membrane), i.e. out-of-plane. These orientations are depicted in Figure 2.6, also displaying the aforementioned orientations for both polarizations at the source. The calculation of bandstructures serves as a prediction of the system's

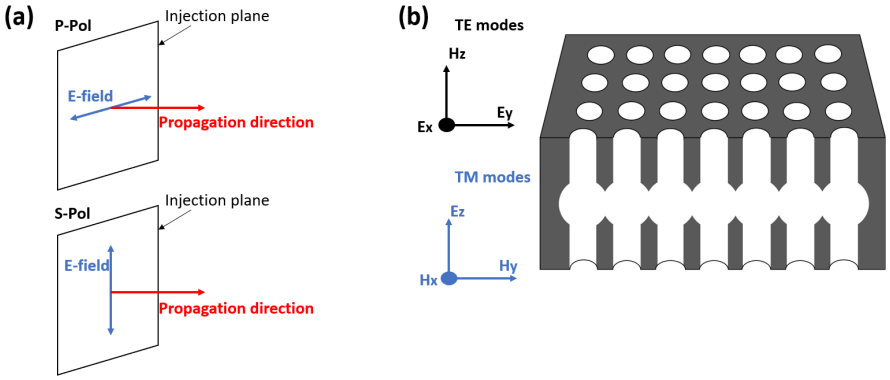

Figure 2.6: Conventional orientations for polarization of light vs convention used in photonic crystals. (a) Convention for polarization of light in the light source, according to the orientation of the electric field relative to the injection plane. (b) Convention of polarization for photonic crystals.

optical properties, since they display the number of modes propagating in a certain direction, as well as the existence of a pPBG or even a Full photonic bandgap (PBG). Photonic bandstructure engineering is also interesting since photonic crystals may be used in applications based solely on the existence of the PBG or the propagation of modes along allowed bands [91]. For this structure, there are two guided modes at the $X-$point that lie below the light cone and four at the $M-$point for both polarizations. Zooming in the $\Gamma - X$ direction (Figures 2.4.d and 2.5.d), the dispersion relation is approximately linear, with bands displaying a low curvature at the vicinity of the $X-$point, opening a gap of frequencies. This gap exists only in the $\Gamma - X$ direction, disallowing light within that range of frequencies to propagate along this direction, hence why it is designated as a pseudo-photonic bandgap. As a consequence, a peak in the reflectance spectrum appears at the set of frequencies the pPBG ranges, mapping the dispersion relation at the band edges. In these regions, the optical modes are slowed down, since the group velocity tends to vanish due to the low curvature at the band-edges

$$\frac{d\omega}{dk} \longrightarrow 0 \tag{2.2}$$

leading to an enhanced radiation-matter interaction. At the vicinity of the $X-$point in the dielectric band, i.e. at ω_-, interference of modes travelling forward and backwards will create a standing wave with antinodes at high-index regions and nodes a low-index regions, where for the air band, at ω_+, occurs exactly the opposite effect. Simulations from Figures 2.4.b and 2.5.b state that the electric field is enhanced for longer wavelengths, i.e. near the longer wavelength that makes up the pPBG. It is also noticeable a gap at

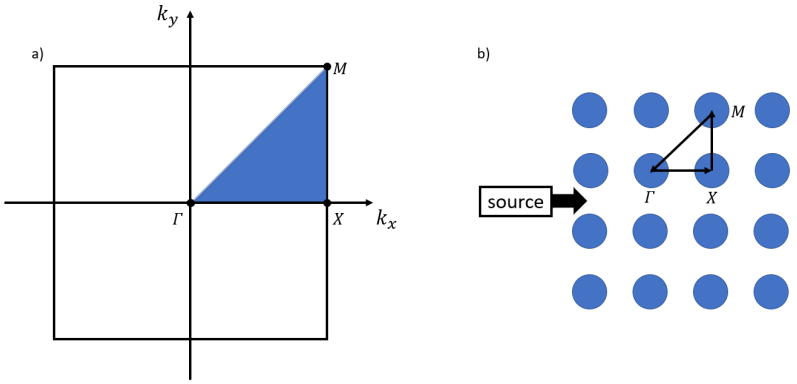

Figure 2.7: (a) IBZ of a square lattice. (b) Visualization of the path bandstructures are computed.

the symmetry point M. This feature is seen at oblique incidence (see Subsection 2.2.5), and shows the same properties as the standard pPBG. The existance of this gap is due to the two dimensional waveguiding nature of the structure, i.e. the 2D periodicity contained in the waveguide slab. This is further explained in Subsection 2.2.5.

2.2.3 Variation with thickness

After a more general understanding of the system's photonic properties, the thickness of the Si_3N_4 coating was changed in order to study the effect of coating thickness on the photonic response of the system. Reflectance at normal incidence was simulated for 6 and 60 nm, in addition to the aforementioned 30 nm, for both polarizations. These results are presented in Figure 2.8.

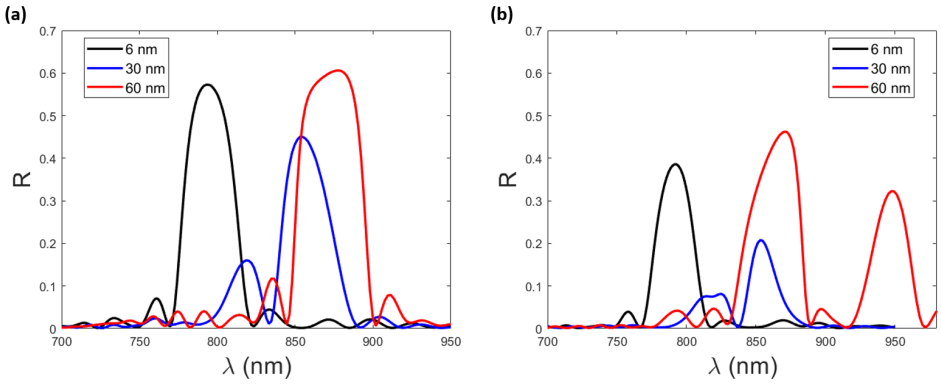

Figure 2.8: Reflectance at normal incidence for different Si_3N_4 thicknesses and water as the immersion medium with (a) *p*- and (b) *s*-polarized light: 6 nm (black), 30 nm (blue) and 60 nm (red).

It is noticeable, by analysing Figure 2.8, the red-shift on the central wavelength for both polarizations as the coating thickness increases, since the effective refractive index of the sPhC also increases, which agrees with Bragg-Snell's Law. This, however, does not necessarily change the size of the pPBG significantly, since it is directly related to the refractive index contrast between the bulk of the crystal and the medium filling the pores [28], and since materials do not change, the width of the pPBG varies only slightly.

Figure 2.8.b shows this behaviour for *s*-polarized light; it is noticeable the rise of the peak adjacent to the central peak, especially for 60 nm. Since the FDTD simulates a perfect photonic crystal, i.e. without irregularities on the surface so no surface effects are taken into account, this can be explained by numerous internal reflections throughout the whole structure, mainly in in the silica-Si_3N_4 and Si_3N_4-pore interfaces, in addition to the net back-reflections at both ends of the structure, accounting for the growth of the peak. Figure 2.9 demonstrates the mapping of the spectral position of the pPBG with the central reflectance peaks at the symmetry point X. It is clear the shift of the pPBG to lower energies, furthering the fact that it shifts to the NIR. A special mention must be made to the graph of 60 nm of *s*-polarization, since it shows two identical peaks, which could induce in error when analyzing the actual position of the pPBG. The mapping with the dispersion relation proves that this pPBG correponds to the first peak (at a higher energy) instead of the second one, which may be a result of cumulative back-reflections. A slight difference on the width of the gaps and on the position is seen since bandstructures are computed assuming the complex geometry of the pores as cylinders with an weighted-average refractive index. Notwithstanding that, the results show consistency and match the observations that were previously expected. Table 2.1 shows the properties of the pPBGs extracted from the simulations. The results given by the simulations are a bit counterintuitive in terms of the size of the FWHM since, in the usual knowledge of PhC theory, these should increase when the effective refractive index increases.

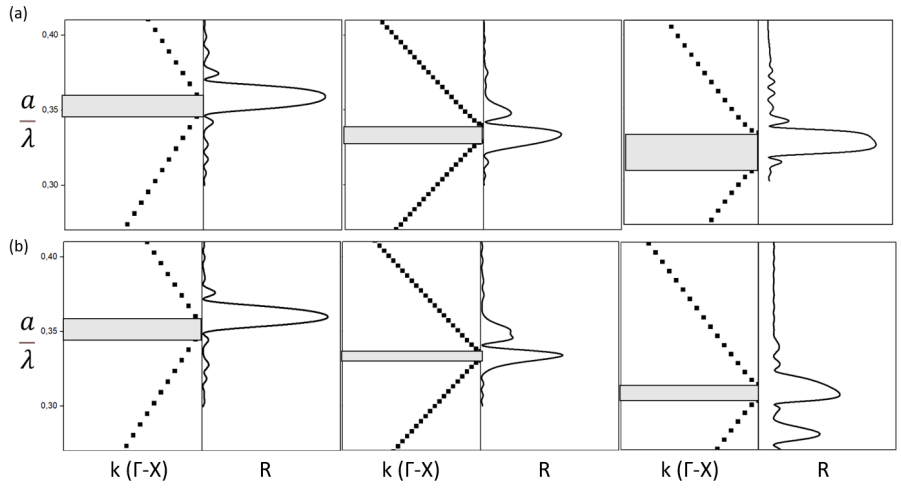

Figure 2.9: Mapping of the dispersion relation at the vicinity of the symmetry point X for girdle band structures coated with Si_3N_4. a) *p*-polarization and b) *s*-polarization for all three thicknesses: 6 nm (left), 30 nm (middle) and 60 nm (right).

Table 2.1: Simulated pPBG properties for Si_3N_4-coated girdles

p-pol	6 nm	30 nm	60nm
λ_c (nm)	794.9	857.0	872.7
FWHM (nm)	29.9	26.0	37.8

s-pol	6nm	30nm	60nm
λ_c (nm)	791.5	854.9	863.9
FWHM (nm)	25.8	16.5	35.9

2.2.4 Variation with material

Coating the girdle band structures with higher refractive index materials red-shifts the pPBG; at the same time, it increases significantly the FWHM due to higher refractive index contrasts. To study this effect, the previously studied 30 nm coating of Si_3N_4 will be taken as a reference for comparisons with to coatings of the same thickness of TiO_2 and Si. Figure 2.10 displays the reflectance at normal incidence for all three materials.

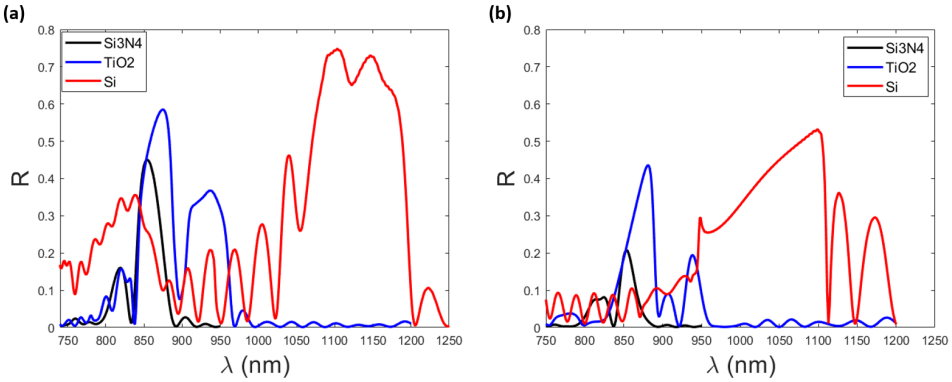

Figure 2.10: Reflectance at normal incidence for all three coating materials with a thickness of 30 nm and water as the immersion medium: Si_3N_4 (black), TiO_2 (blue) and Si (red). a) *p*- and b) *s*-polarization.

It can be seen that the FWHM of the reflectance peak widens when increasing the refractive index of the inserted material in both polarizations. In addition, the central wavelength of the reflectance peak red-shifts to higher wavelengths in the NIR region, meaning a pPBG located at lower energies with inhibition of a wider range of light modes, thus concluding that a PhC with higher refractive index materials leads to wider photonic bandgaps as stated in Gyu Han *et al* [48]. The reflectance also increases with the refractive index of the crystal, a result that agrees with Fresnel's equations for reflectance at normal incidence, where the reflection coefficient r depends on both media where light is propagating (Equation 2.3), in this case would be water inside the pores and the modified bulk, and increases with the refractive index contrast.

$$r = \left(\frac{n_{H_2O} - n_{sPhC}}{n_{H_2O} + n_{sPhC}} \right)^2 \tag{2.3}$$

The Si-coated sPhC displays a wide pPBG in the NIR which can be of interest for applications such as optical communication and telecommunication [92]. Introducing materials with higher refractive indices seems to also increase the number of internal reflections due to the modification made to the diffraction grating nature of the sPhC, since light is dealing with three different dielectrics, as it is noticeable for the cases of TiO_2 and Si. These secondary oscillations may be interpreted as Fabry-Perot fringes due to internal reflections, not only by both ends of the structure but also within the refractive index gradient in the pores. Table 2.2 displays the results of the photonic response relatively to the plots above.

Table 2.2: Simulated properties for all three materials

p-pol	Si_3N_4	TiO_2	Si
λ_c (nm)	857.0	868.1	1126.2
FWHM (nm)	26.0	35.6	134.3

s-pol	Si_3N_4	TiO_2	Si
λ_c (nm)	854.9	872.3	1061.7
FWHM (nm)	16.5	36.2	163.5

2.2.5 Angular incidence

All simulations from the three previous subsections were carried out with light focusing on the girdle band structure at normal incidence. Varying the angle of incidence reveals some features that normal incidence is unable to display, such as a blue-shift in the spectral position of the pPBG [62, 87] and higher order reflectance patterns, multiple of the Bragg frequency [93]. As stated from Equation 1.3, the spectral position of the pPBG blue-shifts as the absolute value of the angle of incidence increases, meaning the it will be located at higher energies in the bandstructure, since the wavevector changes according to the angle of incidence. It is also expected a decrease on reflection for *p*-polarization and consequently an increase for *s*-polarization for angles above the Brewster's angle [94]. Figure 2.11 shows the reflectance as a function of wavelength and angle of incidence for the 30 nm thick Si_3N_4-coated girdle band structure.

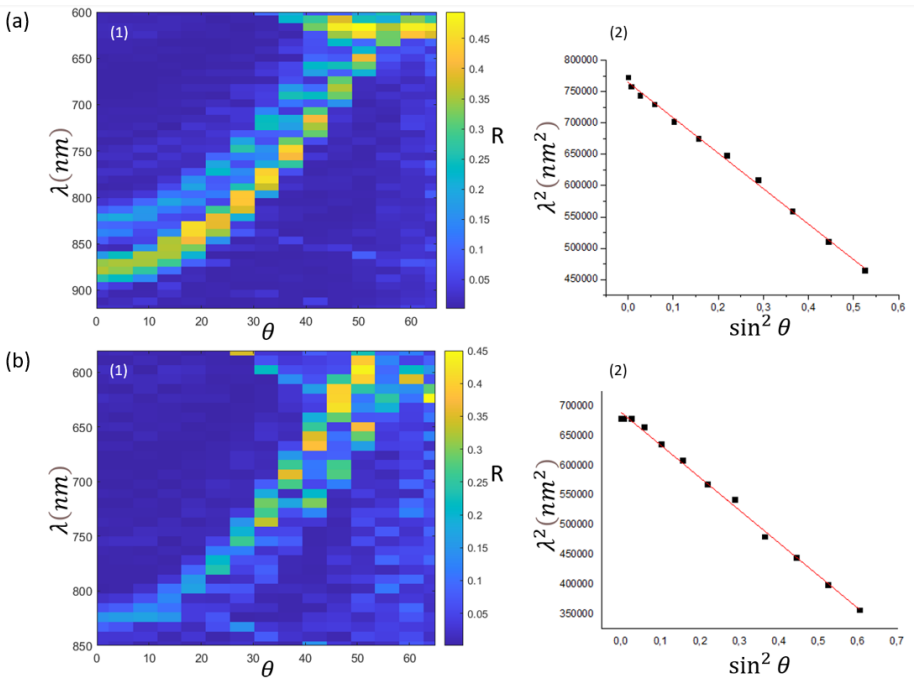

Figure 2.11: Angle-dependent reflectance for a 30 nm deposition of Si_3N_4 with water as the immersion medium. a) *p*-polarization. b) *s*-polarization. Items (1) and (2) correspond to the simulated angular reflectance of the structure and linear fit of all central wavelengths at all computed angles, respectively.

By analysing the contour plots from Figs. 2.11.a and 2.11.b, it can be seen that the spectral position of the pPBG blue-shifts when increasing the angle of incidence as predicted in Equation 1.3. Furthermore,

the reflectance values of the central peak decrease as the angle increases for *p*-polarized light, reaching a minimum at the Brewster's angle, where from this angle on the reflectance for *s*-polarized light keeps rising; for smaller angles, though, reflected light is mostly *p*-polarized, in which explains the difference in the width of the peaks in Figures 2.4.a and 2.5.a. For both polarizations, the previously mentioned peak adjacent to the central peak shows the same behaviour as the latter, in terms of angular dependence and even increased/decreased reflectance values. Since the software considers a smooth surface, this second peak is probably not due to a surface effect but rather a combination of higher order modes and internal reflections, which shows the same optical features as the pPBG. This effect is particularly sensitive to high refractive index contrasts [62], which could explain the increased reflectance as the thickness and refractive index of the inserted material increases. The graphs on the right column of Fig. 2.11 plot the squared values of the central wavelength of the reflectance peak respective to the squared sine of the simulated angles of incidence, $\lambda^2 = \lambda^2(\sin^2\theta)$. A linear fit of these values, shown in red, corresponds to the theoretical Bragg-Snell's Law, shows a very reliable fit to plotted data. From this fitting, the effective refractive index of the sPhC was extracted, with a value of 1.50 ± 0.04 for the 30 nm thick Si_3N_4-coated girdle structure, considering both polarizations. This value is higher than the one calculated for the bare girdle band structure, confirming a higher sPhC effective refractive index. With this value, the Brewster's angle, θ_B, can be calculated, since

$$\theta_B = \arctan\left(\frac{n2}{n1}\right) \tag{2.4}$$

where n_1 is the incident medium, water, and n_2 the effective refractive index of the sPhC, obtaining $\theta_B \approx 48°$, which shows a close result when comparing with the contour plots of Figure 2.11. A secondary pattern appears around $\theta_i \approx 40°$ at lower wavelengths, crossing the pPBG at $\theta_i \approx 50°$. This pattern results from the two dimensional waveguiding of the sPhC, in which in-plane diffraction of guided modes over the period in the $y-$direction is happening. Similarly to the reflectance peak at normal incidence mapping the pPBG at the band-edges in the $\Gamma - X$ direction, this feature represents another pPBG that is opened between the set of guided modes at the vicinity of the $M-$point. This feature is also present for the other simulated materials, concluding that is only noted for light focusing at oblique incidence, i.e. in the $\Gamma - M$ direction or vice-versa. These simulations were also carried out for TiO_2 and Si, as well as the effective refractive index approach, obtaining values of $n_{eff} = 1.565 \pm 0.012$ and $n_{eff} = 1.925 \pm 0.004$, respectively, for 30 nm thick coatings.

2.2.6 Thickness optimization through enhanced confined electric field

The study made on this subsection focuses on finding out the thickness of each deposited material where confinement of light is enhanced the most by simulating the electric field intensity that concentrates inside the pores. The intensity evaluated is the ratio of the incident electric field $|E_i|^2$ and the electric field inside the pores, $|E_o|^2$.

As stated before, the electric field concentrates most of its energy at the regions where the dielectric function is higher, at ω_- in the dielectric band, and the confinement of modes is enhanced for wavelengths near the band edges due to the low group velocity of light when propagating on the crystal. For that reason every plot shown in Figure 2.12 corresponds to wavelengths where the field inside the pores is enhanced the most. Simulations for all three materials with the previously mentioned thicknesses, at both polarizations, have shown an overall preference for thicknesses of 60 nm for Si_3N_4 and TiO_2 and 30 nm for Si in terms of light confinement. From these simulations, when changing the deposited material to another with a higher refractive index, the intensity of electric field inside is higher, which may suggest a more efficient trapping of modes with greater lifetimes.

The fact that a coating of 30 nm of Si may improve light trapping than a 60 nm coating can be explained by its low absorption coefficient at higher wavelengths, since the pPBG for the latter lies well beyond 1100 nm, wavelength at which silicon becomes transparent and thus does not absorb light at all. Table 2.3 shows the results taken from this analysis, as well as the wavelengths where these plots were retrieved.

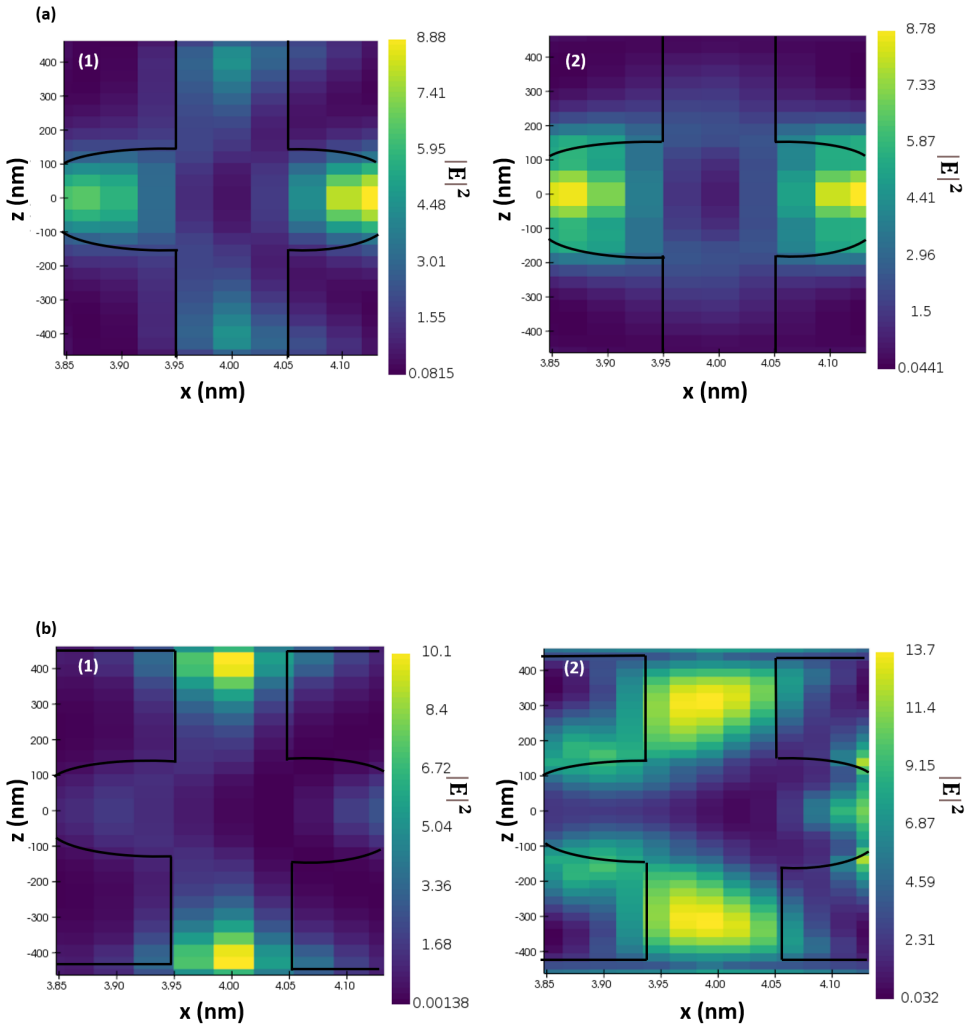

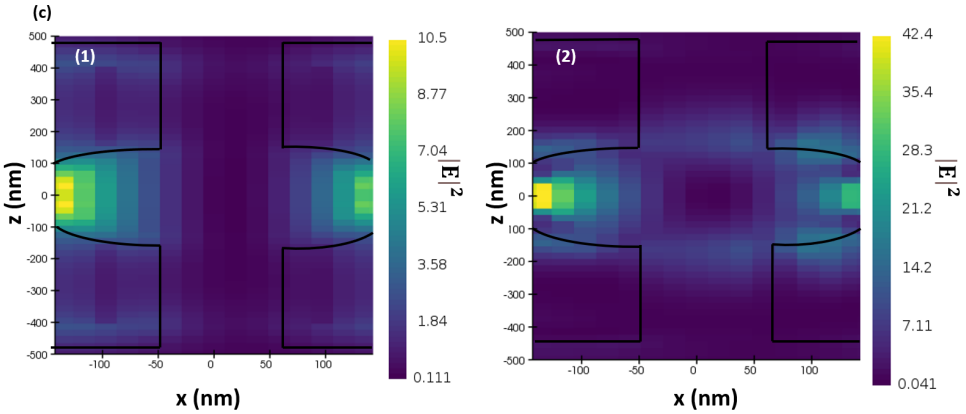

Figure 2.12: Confined electric field within a pore simulated for all three materials. The plots here displayed are only for thicknesses where the enhancement of confined electric field was maximum. (a) 60 nm of Si_3N_4. (b) 60 nm of TiO_2. (c) 30 nm of Si. Items (1) and (2) for each material correspond to *p*- and *s*-polarization, respectively.

Table 2.3: Results from simulated electric fields confined within the girdle band structure.

p-pol	Si_3N_4	TiO_2	Si
Thickness (nm)	60	60	30
λ (nm)	904.1	1042.2	1119.0
$\|E\|^2$	8.88	10.10	10.50

s-pol	Si_3N_4	TiO_2	Si
Thickness (nm)	60	60	30
λ (nm)	891.4	1021.4	1119.5
$\|E\|^2$	8.78	13.70	42.40

2.2.7 Effect of the lattice geometry

Simulations above were carried out for *C. granii* girdle bands, which exhibit square lattices, as already mentioned. This section takes care of studying the effect geometry of the arrangement of pores has on the photonic response of the system. *Coscinodiscus wailesii* is a diatom species whose girdle pores are arranged in a hexagonal pattern with a lattice constant of approximately 330 nm [62, 86]. Figure 2.13.a corresponds to a SEM image, reprinted from Wardley *et al* [86], of a flat girdle band of *C. wailessi* species, exhibiting in great detail its highly arrange hexagonal pattern of pores. The scale bars are 10 µm for the left image and 1 µm for the one that displays the pore arrangement, on the right. Figure 2.13.b corresponds to a cross sectional view of the pores from Kucki *et al* [95], in which the geometry shows similarities with that from the *C. granii* girdle bands. The diameter of these pores can normally be bigger than the diameter of pores of *C. granii* girdle bands, although for this theoretical study the same dimensions were used in order to simplify the effect of the geometry of the lattice. The lattice constant was assumed to be 330 nm and the immersion medium is water.

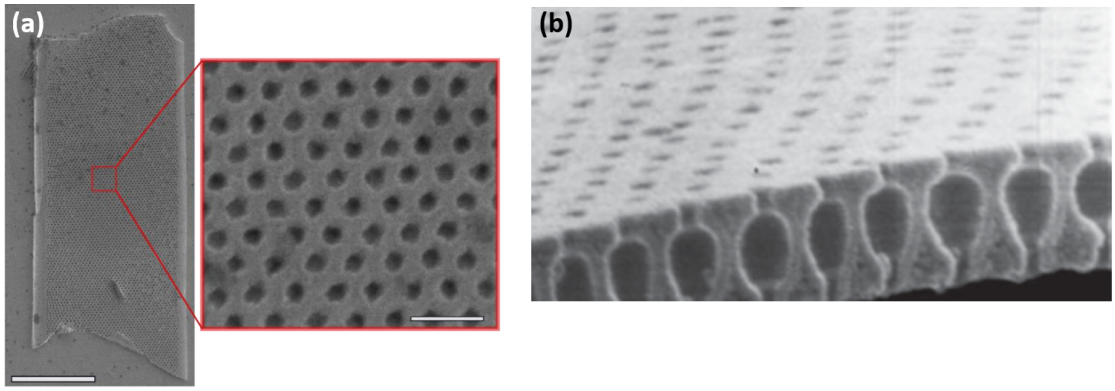

Figure 2.13: SEM images of *Coscinodiscus wailesii* girdle bands. (a) Geometry of a flat girdle band, showing its highly ordered hexagonal pattern. (b) Cross section showing the geometry of the pores. Images were reprinted from Wardley *et al* [86] and Kucki *et al* [95], respectively.

Bragg-Snell's Law states that the central reflectance peak is directly proportional to the lattice's interplanar spacing D, at normal incidence. However, the latter depends on the orientation of the lattice towards the incident light as it can be seen in Figure 2.14.a, corresponding to Orientation 1, and Figure 2.14.b, corresponding to Orientation 2, where incoming light is perpendicular to the family of planes (110) and (100), respectively.

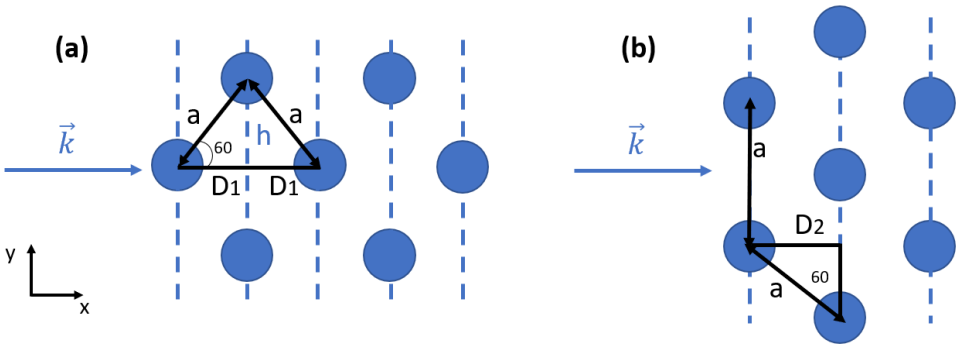

Figure 2.14: Orientations of the girdle band structure at which light was shone. (a) Oriantation 1. (b) Orientation 2.

The lattice constant of a hexagonal lattice can be decomposed by two projections in the x and y axis; these projections are indeed the correponding distances between the planes that intersect each set of pores in the z axis. A geometrical analysis of Figure 2.13 concludes that the respective interplanar distances are $D_1 = a\cos 60 = 165$ nm and $D_2 = a\sin 60 \approx 285.8$ nm. These values agree with the general expression for the interplanar spacing between a family of planes (hkl) for hexagonal lattices:

$$\frac{1}{d_{hkl}^2} = \frac{4}{3}\frac{h^2 + hk + k^2}{a^2} + \frac{l^2}{c^2} \tag{2.5}$$

where h, k and l are the Miller indices.

These differences in central peaks are depicted in Figure 2.15, alongside comparisons with simulations made for the bare *C. granii* girdle band structure presented in Subsection 2.2.1. The direction of light shining at these structures is such that the lattice constant for the *C. granii* girdle bands matches the interplanar distance. It is noticeable the difference between the peaks obtained for both geometries as a consequence of the interplanar spacing: Orientation 1 displays a reflectance peak at $\lambda = 677.8$ nm whereas light shining on Orientation 2 gives rise to a reflectance peak at $\lambda = 786.9$ nm, thus agreeing with Bragg-Snell's Law.

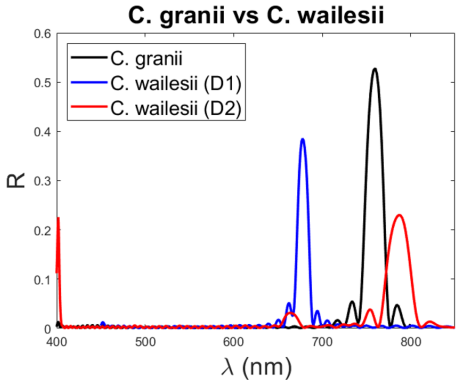

Figure 2.15: Comparison between both orientations for girdle band structures from *C. wailesii* (Orientation 1 in blue and Orientation 2 in red) and *C. granii*, in black. Simulations were made with water as the immersion medium.

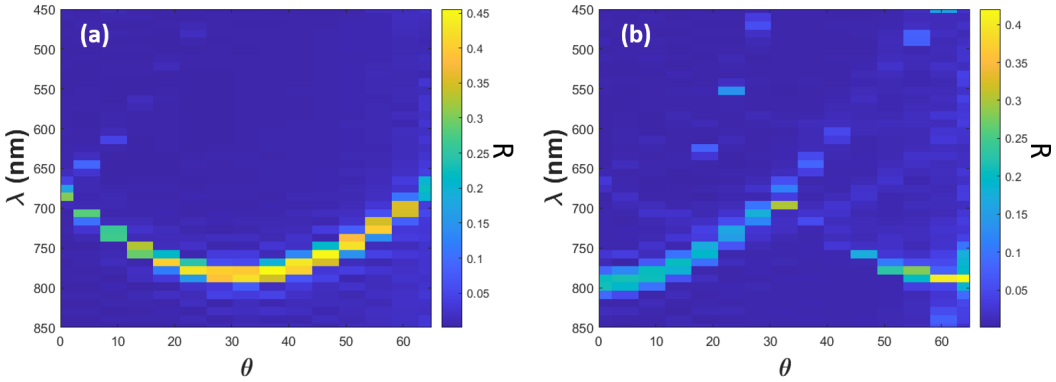

Figure 2.16: Angular reflectance for both Orientations. (a) Orientation 1. (b) Orientation 2. Simulations were made with water as the immersion medium.

Focusing light on the crystal at Orientation 1 is not a new discovery. Figure 2.16.a shows the angular dispersion at this orientation. It is seen a red-shift on the central position of the reflectance peak towards a maximum at $\theta \approx 30°$, which is a rather odd behaviour. However, this only means that shining light at this orientation would simply be equivalent at shining light at Orientation 2 with an angle of $30°$. Moreover, this means that light is shining towards the $\Gamma - M$ direction or vice-versa, which is $30°$ tilted relatively to the $\Gamma - K$ direction (Figure 2.17), i.e. direction at which light is focused at Orientation 2.

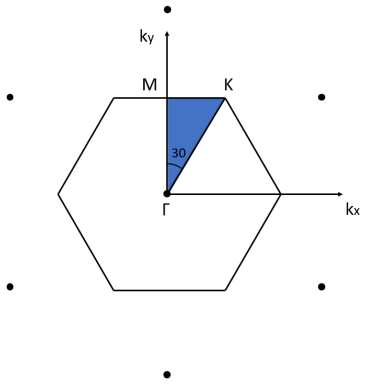

Figure 2.17: IBZ for hexagonal lattice.

2.3 Conclusions

This Chapter showed a theoretical study of the possible effects of introducing new materials on girdle bands that exhibit a square lattice of pores by simulating the photonic response and considering coatings as conformal thin films with the already mentioned thicknesses.

The main conclusion to take is the red-shift on the central wavelength when the effective refractive index of the sPhC increases. It was also noted that the FWHM of the reflectance peaks are wider when the refractive index contrast between the bulk of the sPhC and the immersion medium filling the pores is higher, thus leading to a higher photonic strength. The asymmetry of the structure was also proven, as differences at the central wavelengths for both polarizations, which are unusual in a conventional 2D PhC.

The study of band diagrams, or bandstructures, also served as a useful tool to further understand how and where the pseudo-photonic bandgaps in the $\Gamma - X$ direction are positioned. The mapping of the dispersion relation with the reflectance density of states showed to be a reliable and consistent one, despite the slight difference in the structure used for the calculations of bandstructures, showing nonetheless to be a good approach. Not only the existance of this gap was noted, but also a feature at the vicinities of symmetry point M. This feature was also seen at the angular-dependence contour plots, as reflectance patterns that would start to appear at larger angles. These patterns showed a behaviour similar to the standard pPBG according to Bragg-Snell's Law, thus proving the two dimensional waveguiding nature of the structure.

The electric field confined within the structure, due to total internal reflections, was analyzed at one pore (one unit cell) and was revealed to be enhanced for certain coating thicknesses; it was also noted that increasing the refractive index of the coating material would increase the amount of electric field confined.

Lastly, a brief study was made for a girdle band structure with a hexagonal arrangement of pores. This geometry is more complex than the square lattice, since the lattice constant can be composed by two orthogonal projections that correspond to the interplanar distance of each orientation light is shining on. Two different reflectance results at normal distance were obtained for light shining at orthogonal directions in the plane of the sPhC, as a consequence of the interplanar distance. This contrasts the square lattice,

where shining light on an orthogonal direction in the plane of the sPhC would give the same results as the ones studied in this Chapter.

3

Methods and Measurements

3.1 Treatment of diatoms

The diatom species *Coscinodiscus granii* was the case of study throughout the whole Thesis. This means that every measurement made and presented in this Chapter are relative to that species. This Section is about how diatoms were treated, from their culture and nurturing to the methods of removal of the organic part and separation of the pieces of the frustule, i.e. girdles and valves.

3.1.1 Diatom nurturing

Diatom species should be stored at an adequate medium, full of nutrients necessary to the formation of the silica walls, i.e. the frustules. Diatom cultures should also be stored in places with good light conditions and temperature so that reproduction can be as efficient as possible. In order to ensure these conditions, strain K-1834 of *C. granii* underwent a process of nurturing that involved the creation of other cultures of the same strain, increasing the reproducibility and keeping diatoms healthy. This process also served as a way to have enough supplies of diatoms to carry out further measurements. Figure 3.1 shows the first four cultures of diatoms. They can be found at the bottom of the flasks as brown coloured agglomerates, although some of them can be suspended in the liquid. The nurturing process goes as follows. A flask

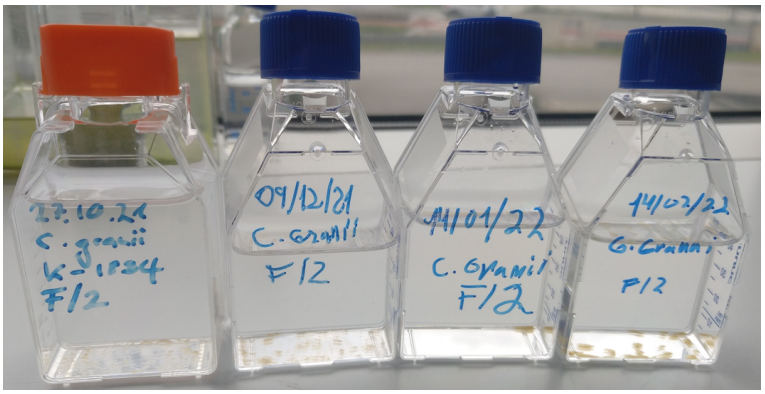

Figure 3.1: First four diatom cultures of strain K-1834 of *C. granii* species.

is filled, about 40 ml, with the medium suitable for diatoms. This medium is called L1 (or F/2, the one used and labeled in Figure 3.1) and is closely related to regular salt water from the sea, containing all the necessary nutrients diatoms need to develop their exosqueletons [96]. Then, 1 ml of diatoms, from a previous culture, is added to the new flask and stored in a place where sunlight shines as much as possible, which in this case was next to the window at the service corridor of INL, as well as a regulated temperature, about 19°C. This process is depicted in Figure 3.2.

It was noted that during the months of January and February growth was obviously slower, meaning it took some weeks to visualize the brown agglomerates at naked eye. This is in contrast to the following months, where they were already visible the day after the nurturing due to the good environmental conditions.

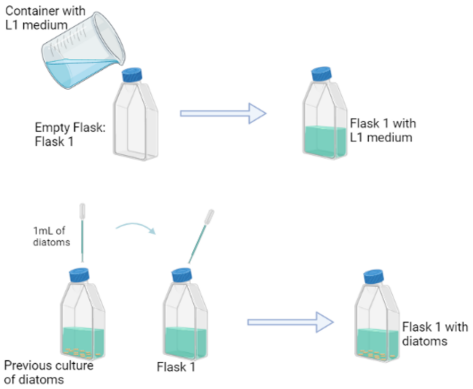

Figure 3.2: Diatom nurturing.

3.1.2 Diatom counting

A further analysis on the concentration of diatoms after the nurturing process was made. The resulting concentration of diatoms was calculated by counting the number of single specimen found in 1 ml. For this purpose a Sedgewick Rafter counting chamber, consisting of 1000 squares, in a 50 ×20 arrangement, of 1 µl each, and a microscope were employed. A total number of 50 random squares with and without diatoms were analyzed, counting the number of diatoms lying at each square. This process led to a value of *ca.* 3080 diatoms ml^{-1}, which is normally in accordance with previous studies.

3.1.3 Separation and cleaning of girdle bands and valves and removal of the organic part

In order to study the different silica constituents of diatoms, the frustule undergoes a cleaning process. To extract the silica constituents of frustules, the organic component of the cells, responsible for holding valves and girdles together, needs to be removed. After the removal of the organic matter valves and girdles eventually separate from each other. Two cleaning protocols were executed and are explained

down below. The final result was the same for both protocols and the proof of cleaned samples is shown only for one.

3.1.3.1 First protocol

20 ml of a stock diatom culture was poured into a beaker. Then, an equal volume of 30% H_2SO_4 was added and the sample was gently agitated throughout. Saturated potassium permanganate (7-8 grams of $KMnO_4$in 100 ml of MilliQ water, freshly made) was added afterwards a little at a time, while gently agitating. The sample bubbles up and turns brown at first; $KMnO_4$ kept being added until the sample reached a purple tint. This step is responsible for oxidizing the organic matter inside the cells. After that, saturated $(COOH)_2$ (10 g of $(COOH)_2$ in 100 ml of MilliQ water, freshly made) was added a little at a time while under gentle agitation, until the solution became transparent. Equation 3.1 summarizes the aforementioned oxidation process:

$$2\,KMnO_4 + 3\,H_2SO_4 + 5\,(COOH)_2 \longrightarrow K_2SO_4 + 2\,MnSO_4 + 10\,CO_2 + 8\,H_2O \qquad (3.1)$$

The resulting sample was then centrifuged at 3000 rpm for 20 min. The sample was concentrated to about 5 ml and the excess supernatant was discarded and replaced by the same volume of MilliQ water to resuspend the pellet. This centrifuge and rinse process was repeated several times until the sample was clean. To further proof the success of this protocol, 100 µl of cleaned sample was examined at the microscope. This cleaning protocol was adapted from Hasle [97]. Figure 3.3.(a,b) compares both states of the samples, before and after cleaning, respectively. It is clear the separation of the different parts of the frustule, as girdle bands appear almost perfectly round and the valves with the still-brownish colour. After the cleaning process, a drop of 1 ml of sample was analyzed in order to count the existant number of

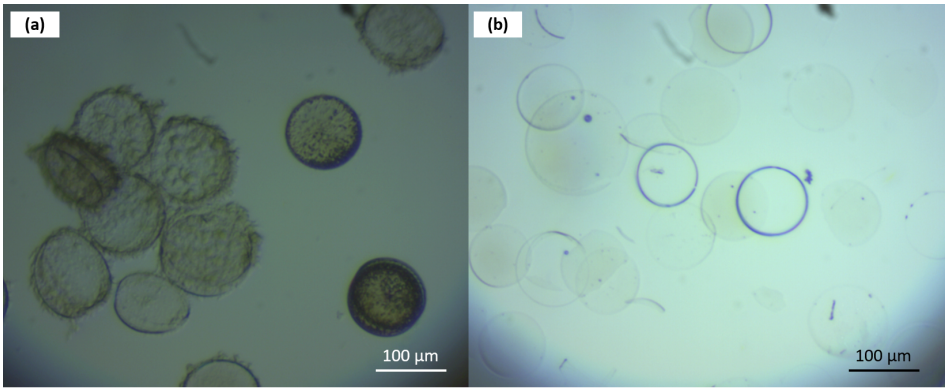

Figure 3.3: (a) Diatoms before cleaning process. (b) Diatoms after cleaning process. The separation between girdle bands and valves is clearly seen in detail.

valves and girdles, similar to the diatom counting process, in which was obtained 1040 girdle bands ml^{-1} and 2340 valves ml^{-1}, equivalent to a valve-to-girdle band ratio of 2.25. Theoretically, this disparity should have been lower, since the number of valves and girdle bands in a single diatom frustule are usually the

same. However, due to their larger size, valves tend to settle faster than girdle bands, who remain longer in the supernatant. The protocol involves a supernatant removal to replace the acid for water and thus some girdle bands may be lost in the process. This fact was also observed in Goessling *et al* [68].

3.1.3.2 Second protocol

To 10 ml of diatom solution, 1ml of 10% HCl was added, in order to remove $CaCO_3$ deposits that precipitate alongside the growth of the frustule [98]. Then, 2 ml of 30% H_2SO_4 were added, proceeded by 10 ml of saturated $KMnO_4$. The sample was left for 24 hours, with occasional agitations. After that, about 10 ml of $(COOH)_2$ was slowly added while agitating the sample until it becomes transparent. The sample fizzed and formed air bubbles in the process. The sample was centrifuged afterwards at 3000 rpm for 20 minutes, followed by discarding the supernatant and resuspension of the pellet with MilliQ water. This protocol was adapted from Christensen [99] and Lundholm *et al* [100]. The main difference between this protocol and the previous is the addition of HCl, which will neutralize the alkaline components of the frustule [101], the $CaCO_3$ deposits, revealing to be a more efficient method to clean diatom frustules, despite being slower, since it the sample needs to be at partial rest for a full 24 hours, which also differentiates this method to the first one.

Despite the successfulness of both protocols, the first was the one preferred to carry on measurements thereafter, due to its easier and safer manipulation alongside its great results.

3.1.4 Morphological characterization

Analysis on the morphology of girdle bands were made by means of SEM and Energy Dispersive X-Ray (EDX) measurements to visualize and study the periodicity and size of the pores, for further comparisons that are discussed in Section 3.2.

Clean girdle bands were coated with 10 nm of gold by sputtering before the morphological characterization. This thin layer of gold provides a better sample conduction without charging the silica structures and a homogeneous surface for analysis and imaging [102]. Figure 3.4 corresponds to a SEM image of a flat girdle band taken with an applied potential of 5 kV. The scale bar for this image is 5 µm. It is clearly visible the highly ordered porosity arranged in a square lattice, also prove by the Fast Fourier Transform (FFT) (lower left corner), which was processed by *ImageJ* software. The periodicity of this girdle band was calculated in the $x-$ and $y-$ directions, a_x and a_y respectively, by counting the distance between 10 pores from 10 random rows in the respective axis and dividing the result by 10, in order to reduce the final error. The measured lattice constants were $a_x = 290 \pm 1$ nm and $a_y = 293 \pm 2$ nm. These values are typical for girdle bands of *C. granii* species, and compatible with values obtained in the literature [62]. The radii of the pores were obtained by calculating the effective area of 20 random pores and approximating them as perfect circles of radius r. The value obtained was $r = 83 \pm 6$ nm, also in the range for this species.

Figure 3.5 shows the EDX measurement on the same girdle band, with the main elements of silica having the highest peaks, oxygen and silicon, as well as the detection of gold as an indicator of the aforementioned sputtering process. Elements like potassium and sodium are also detected with considerable peaks. The presence of these elements must be due to some remnants of the medium diatoms were immersed in, even before the cleaning process.

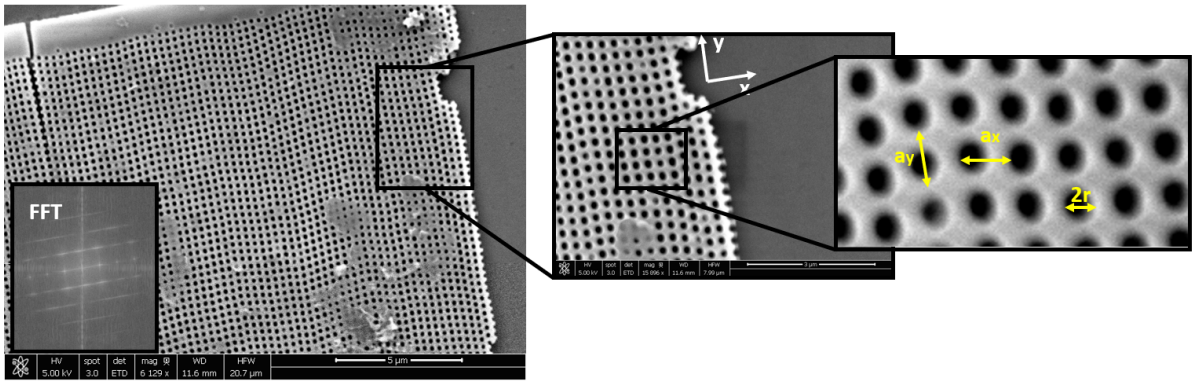

Figure 3.4: SEM image of a clean girdle band lying flat. The lower left corner shows the processed FFT of the structure, displaying the ordered square lattice. The image on the middle shows a close view of the area where pores were measured, with the image on the right showing the lattice constants on the $x-$ and $y-$ directions and the radius of one pore. Scale bars displayed in the image on the left and in the middle one correpond to 5 and 3 µm, respectively.

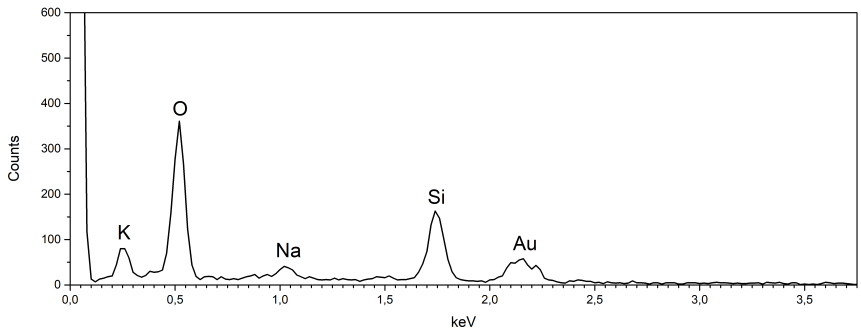

Figure 3.5: EDX measurement of a clean girdle band. The main elements of the silica structure are displayed with the highest peaks, as well as the gold coating. K and Na peaks may be some remnants of the medium diatoms were previously immersed in.

3.1.5 Optical characterization of bare girdle bands

The visualization and analysis of the photonic response of girdle bands (bare and coated) was carried out using a Fourier Image Spectroscopy (FIS) setup (Figure 3.7). The optical characterization done throughout this Thesis consisted on measuring the reflectance of the girdle bands at normal incidence, as well as the angular dispersion. Every measurement was carried out at unpolarized light.

3.1.5.1 Fourier Image Spectroscopy

The Fourier setup, sketched in Figure 3.7, was designed to operate in the visible region, as well as in a small portion of the NIR, range of ~ 400-800 nm. The focal length of the lenses are represented as double-sided arrows with the exception of the objectives, since these are not thin lenses. The setup starts by coupling white light from a tungsten halogen lamp to a multimode optical fiber. The diameters available on the laboratory for this type of fiber were of 25, 50, 105 and 400 µm and they will determine the size of the spot that is focused on the sample. A fiber of 50 µm was coupled to the lamp and into the system, producing a spot of *ca.* 2 µm that focused on the sample (see Figure 3.8.b). This fiber size was chosen since it is desired to characterize only one girdle band, mitigating the effects of neighbouring structures. Light is then collimated with an objective lens and heads towards the microscope (depicted as a microscope cage in Figure 3.7) - *Nikon Eclipse Ti2*. This scheme is simplified, since light operates in the normal direction, creating a 3D system. Through a 50/50 beam splitter, light is normally focused into the sample and then headed into two irises. The first iris regulates the size of the real image and the second acts as a low-pass filter, having the same purpose as the first one but this time in the Fourier space. The polarizer is used to select the polarization of transmitted light. Through two more beam splitters, light is directed to four different detectors: three charge-coupled device (CCD) cameras ((A), (B) and (C)) and a spectrometer. CCD camera (C) is coupled to a monochromator inside the black box and cameras (A) and (B) capture the image in the real and Fourier spaces, respectively. L_6 is used to translate the real plane to a 2f distance away to reach one of the two aforementioned detectors. With the flip mirror on, i.e. up, light is focused onto an optical fiber connected to the spectrometer. When the flip mirror is down, light is headed to the spectrograph, that is composed by the CCD camera (C) and the monochromator, providing a 2D array of sensors for wavelength reflection measurements with angular resolution. The spectrograph used was the *Acton SpectraPro SP-1250*, the fiber-coupled spectrometer is the *USB2000+ Spectrometer* and the CCD camera (C) is a *QImaging Retiga R6 USB3.0 Colour*. Measurements were carried out with a 100x oil immersion lens. This technique allows to increase the resolving power of the microscope. Using the immersion oil between the objective lens and the glass slide that holds the sample allows for light rays to propagate evenly, without significant refractions, since the immersion medium has a refractive index close to that of the glass slide, providing a higher numerical aperture (NA) (about 1.44, higher than 0.95 for state-of-the-art objectives with air as the medium). Without the use of the immersion medium, light rays at oblique incidence would be refracted at the glass-air interface and would not enter the objective lens, resulting in the loss of information. The immersion medium employed was the *Cargille Laboratories* immersion oil with a refractive index of 1.5150 ± 0.0002. Figure 3.8.a is a sketch describing the direction of focused incident light on the girdle band, shining in the plane of the sPhC, i.e. in-plane, rather than on top of the pores (i.e. on a flat girdle, out-of-plane), as simulated in Chapter 2. This is also because previous studies concerning the photonic properties of girdle bands also had the structures in this orientation. Every measurement made throughout this Thesis, wether girdle bands were clean or modified, was carried out in this orientation. Figure 3.8.b is an image of a water-immersed girdle band observed in the FIS setup

with a 100x oil immersion lens with a high NA and a 50 µm multimode optical fiber. It is clearly visible, under these illumination conditions, the waveguiding nature of the gridle band of green light.

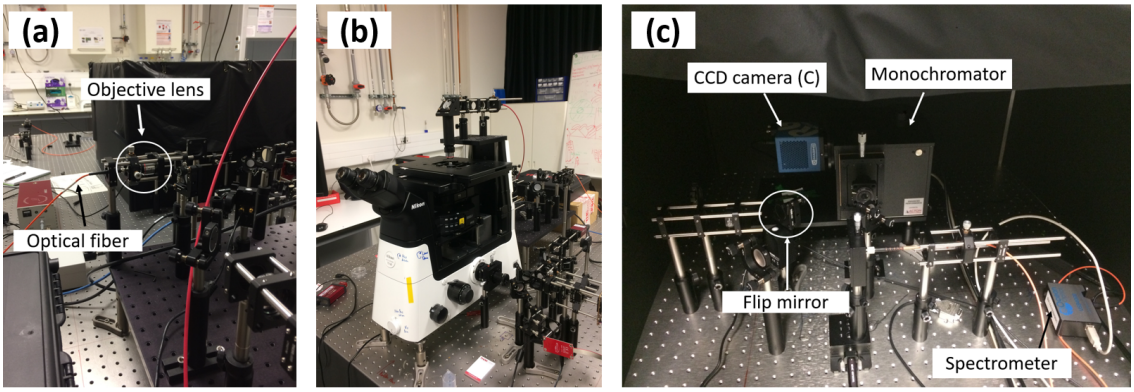

Figure 3.6: Fourier Image Spectroscopy setup. (a) Multimode optical fiber coupled to the objective lens for light collimation. (b) Inverted microscope (microscope cage). (c) Black box content. The main components are labeled: flip mirror, spectrometer, CCD camera (C) and monochromator.

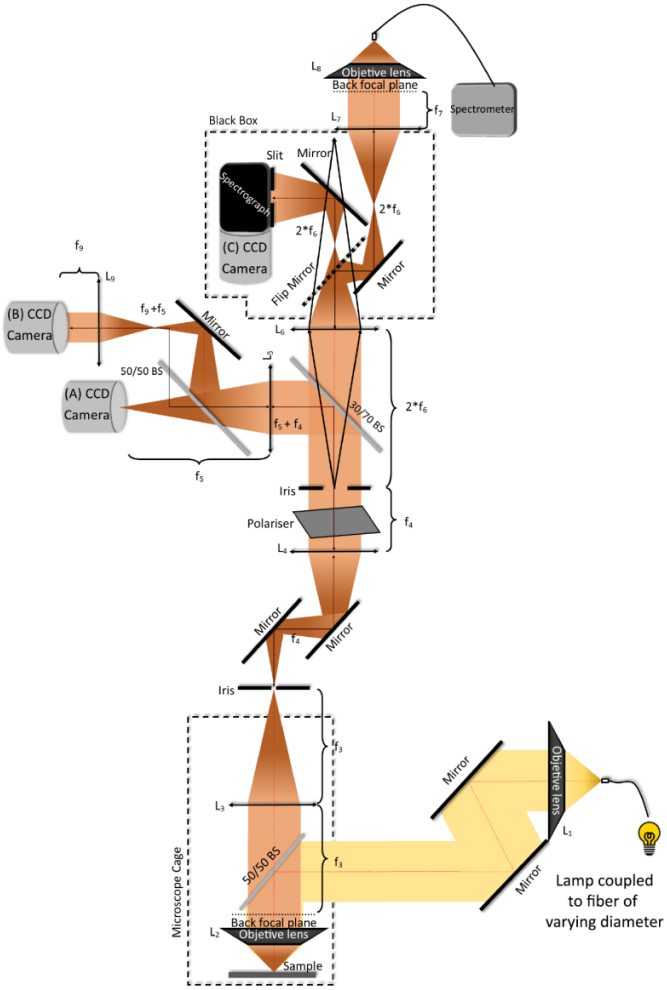

Figure 3.7: Schematic of the Fourier Image Spectroscopy used for optical characterization.

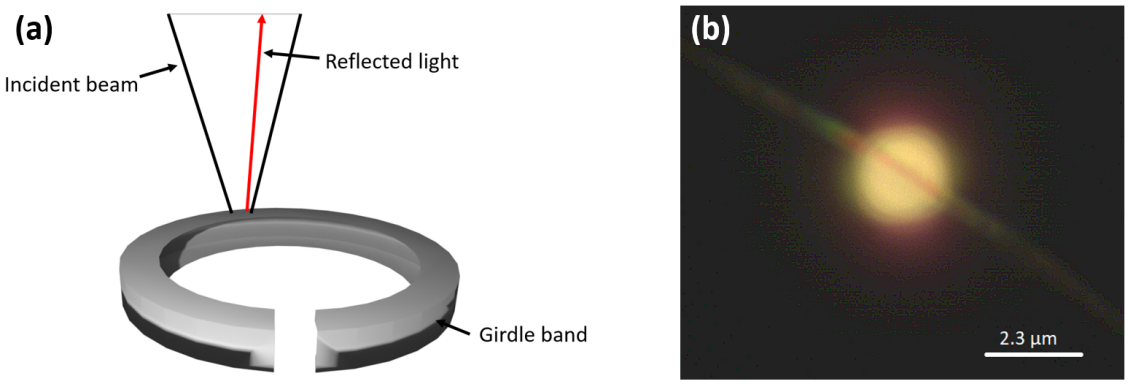

Figure 3.8: Measurement of girdle bands. (a) Orientation of the girdle band when light is focused. (b) Girdle band, in water, observed with a 100x oil immersion lens and a 50 µm multimode fiber, with a numerical aperture of 1.44. The spot focused on the girdle is about 2 µm.

Measurements at normal incidence

At normal incidence, $\theta_{inc} = 0°$, the intensity of the reflected light is detected by the spectrometer and plotted with respect to the wavelength of light. Aside from the reflection of the sample, r_{sample}, a measurement on a reference, r_{ref}, should also be made for normalization, obtaining the actual reflectance of the sample, R. For these measurements, the employed reference was a silver mirror, since it shows a high reflectiviy in the visible spectrum [103]. The optical background noise, N, is removed in the *Spectrasuite* software, by inhibiting light to the spectrometer. Two measurements alongside noise removal are required in obtaining the desired result:

$$R = \frac{r_{sample} - N}{r_{ref} - N} \tag{3.2}$$

The acquired data is then processed in *OriginLab* software. The exposure time was of 5 seconds, since the spot is small, thus taking a longer time to obtain a significant result. This parameter could be increased until before the reference reflection spectrum saturates.

Angular measurements

These measurements consist on focusing a light beam on the surface of a sample and obtain the angular distribution of the reflected beam using Fourier optics [104]. The spectrograph available at INL is only able to capture a wavelength range of approximately 32 nm at at time. For a wider range of wavelengths, a *MATLAB* script was employed to couple and process the data from each of the intervals. As before, the reflection measured from the sample must be normalized by one reference to obtain the reflectance of the sample. The same silver mirror was used. The optical background noise is also considered. This time, three measurements are required to obtain the result given by Equation 3.2: sample and reference reflections and dark, the latter by inhibiting light to the spectrograph. The exposure time on these measurements was of 10 seconds, since a lot of light is required due to the small spot given by the fiber.

Sample Preparation

In order to proceed with the optical measurements, it is necessary to prepare the samples beforehand. This preparation involves immobilizing the girdle bands and valves on a 24 × 50 mm glass slide. Polylysine is an organic compound of lysine cationic polymers, containing positively charged amino groups at pH 7. Polylysine is normally used as a coating in tissue culture, providing good cell adherence when they are attached to the coated surface [105] due to the electrostatic interactions between the positively charged compound and negatively charged cells. This compound was then proposed to neutralize the surface of the glass slide, facilitating the adsorption of girdle bands and valves.

The protocol of sample preparation goes as follows. First, 500 µl of polylysine is poured on the glass cover slide and spread it all over the glass surface in order to get a larger immobilization area. After that, the glass slide was let at rest for 5 minutes. After that, the residual liquid was disposed with the aid of an air gun, since the compound should already be attached to the glass surface. Then, 100 µl of stock solution of girdle bands and valves was poured on top of the immobilization area of the glass surface and let it settle for 5-10 minutes.

Every optical measurement presented in this Thesis was made with MilliQ water as the immersion medium. After a couple of hours, the water present in the sample eventually dries out; to carry on with the measurements, 100 µl of MilliQ water is poured on top of the sample and let it rest for about 30 minutes, so that it can infiltrate into the pores. Figure 3.9 represents a schematic showing the steps of the protocol.

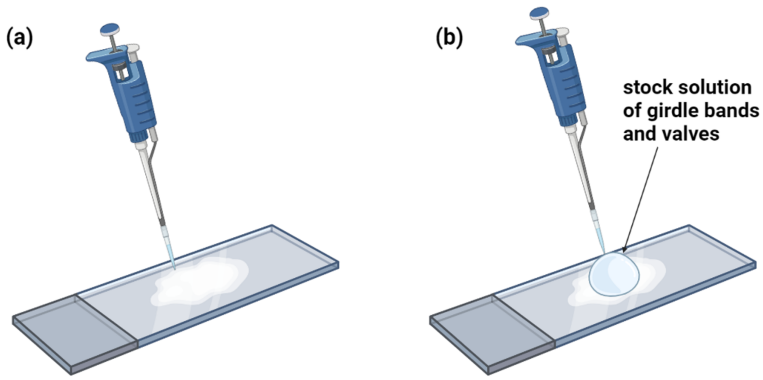

Figure 3.9: Sample preparation for optical measurements. (a) Immobilization of the glass surface with polylysine. (b) Sample is deposited on top of the immobilized area.

After attaching the silica structures to the glass slide, optical characterization of said structures proceeded. First, and in order to have control samples for further comparisons, clean girdle bands immersed in water underwent optical characterization. The microscope employed is an inverted microscope and thus sample was placed on the microscope platform facing upwards, so that the immersion oil does not harm the silica structures as well as to prevent harming the objective lens (see Figure 3.10). Several girdle bands were measured, at different points. Figure 3.11 shows the photonic response measured on this sample, in comparison with simulations from Chapter 2. The graph in Figure 3.11.a shows the reflectance

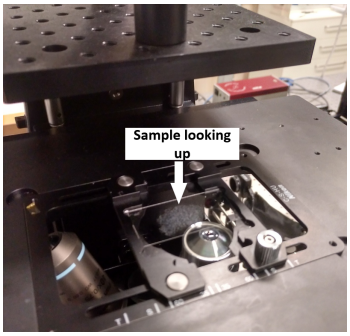

Figure 3.10: Sample placed on the platform.

at normal incidence ($\Gamma - X$ direction) of three different girdle bands (in black) in comparison with the FDTD simulation of the girdle-like structure (in blue). The measurement showed an average central wavelength of 754.4 ± 0.6 nm. The central wavelength was obtained by fitting a Gaussian function using *OriginLab* software. This approach applies also for measurements with modified girdle bands. The position of this peak usually floated between 750 and 755 nm for other samples of clean girdle bands, showing a high conservation of the position of the pPBG. This result matches very well the central wavelength obtained from the simulated structure, which was ∼ 760 nm.

Figure 3.11.b shows the angle-dependence of the pPBG, as a measurement of reflectance as a function of the angle of incidence and wavelength. As expected, the pPBG appears at lower wavelengths at higher angles of incidence, as predicted by Bragg-Snell's Law. Reflectance colorbars correspond to the simulation and measurement halves of the graph; however, the maximum value (given in bright yellow in the simulation and light blue in the measurement) is approximately the same. The angle-dependence of the pPBG also matches the one given by the simulation. Hence, these measurements proved the theoretical response given in Chapter 2 for clean girdle bands, whose structures had a highly ordered arrangement of pores, thus corroborating the ordered porosity on the actual structures, in addition to the SEM measurements in Figure 3.4.

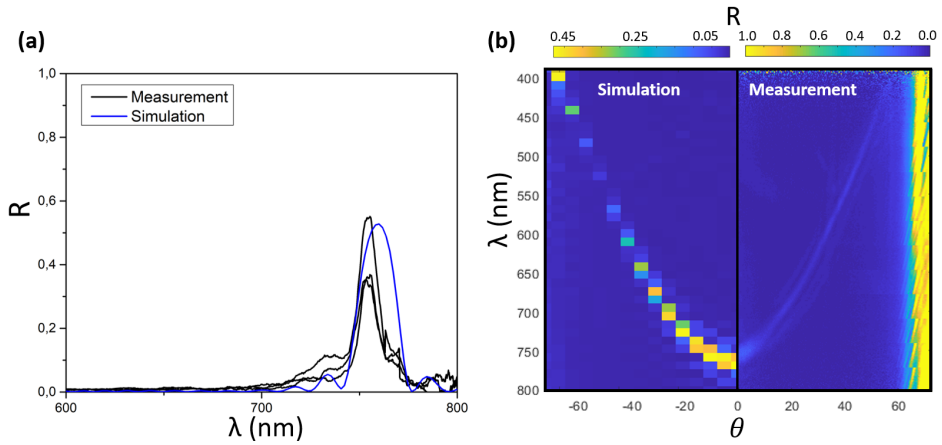

Figure 3.11: Photonic response of clean girdle bands, immersed in water. (a) Measurement and FDTD simulation of the reflectance at normal incidence. (b) Angle-dependence of the pPBG shown by reflectance as a function of angle of incidence and wavelength of light.

3.2 Modification of girdle bands

As seen from Equation 1.3 and simulations from Chapter 2 the central wavelength of the reflectance peak shifts when the effective refractive index of the sPhC, n_c, is modified. The methodology to tune the effective refractive index of the sPhC was to obtain conformal growths of high refractive index materials of choice on the surfaces of girdle bands (external and internal). Here, the modification of girdle bands involved two methods: a functionalization process involving TiO_2 nanoparticles (NPs) and a conformal growth using Plasma-Enhanced Chemical Vapour Deposition (PECVD) of a Si_3N_4 thin-film, each on separate samples of clean girdle bands.

3.2.1 Titanium dioxide functionalization of girdle bands

As a first approach to manipulate the effective refractive index, girdle bands are funcionalized with TiO_2 NPs. Due to its efficient photoactivity, previous studies have reported the functionalization of TiO_2 on diatom frustules for their use in photocatalysis applications, such as air purification [106]. Modification using TiO_2 was also reported to have been made *in vivo*, i.e. TiO_2 was incorporated in diatoms while they were growing their frustules [107].

In the functionalization process used here, the NPs are attached to the surface following an adsorption protocol involving a cationic polyelectrolyte monolayer. This monolayer will facilitate the electrostatic interactions between the silica surface and the NPs since they are both negatively charged and hence enhance the adsorption of the NPs (see Figure 3.12), since silica and silicate glass surfaces have been reported to acquire a negative surface charge density when immersed in water, due to the dissociation of silanol groups (see Equation 3.3) [108].

$$SiOH \rightleftharpoons SiO^- + H^+ \tag{3.3}$$

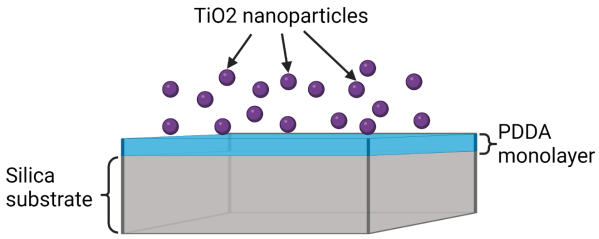

Figure 3.12: Sketch of the adsorption of the nanoparticles in the surface with the aid of the polyelectrolyte monolayer.

A solution of 0.2 mg ml^{-1} of 15 nm TiO_2 NPs suspended in a citrate buffer was used for the attachment process. Previous studies have reported a negative surface charge of the same solution in the same conditions by zeta potential measurements. Five Dynamic Light Scattering (DLS) measurements were

executed in order to measure the average diameter of the NPs. The measured diameter was of 67 ± 8 nm and a polydispersity index of 0.78. The size of the NPs suggests that they might not only get attached to the surface of the girdle bands, but also enter the internal surface of the pores, i.e. the filling void, and remain attached there. The reported polyelectrolyte best suited for the attachment of the nanoparticles to the girdle bands was the poly(diallyldimethylammonium chloride) (PDDA). The attachment protocol is described as follows. First, 272 µl of a 1 mg ml^{-1} PDDA solution in 0.5 M of NaCl was added to 500 µl of a solution of clean girdle bands and valves. Then, it was placed on a vortex mixer at 500 rpm for 20 min. After that, the sample was centrifuged at 2600g for 30 min. After the centrifuge, the upper 600 µl of the supernatant were discarded and replaced by MilliQ water to resuspend the pellet. The latter and the centrifuge steps were repeated two more times; in the second repeat the pellet was resuspended in 1090 µl of TiO_2 NPs solution in sodium citrate. The sample was then placed back on the vortex mixer at 500 rpm for 180 min and centrifuged at 2600g for 30min afterwards. This time, the upper 700 µl of the supernatant were discarded and replaced by MilliQ water to resuspend the pellet, repeating the process two more times, as before, leaving the functionalized girdle bands and valves suspended in MilliQ water. The four main steps of this protocol are illustrated in Figure 3.13.

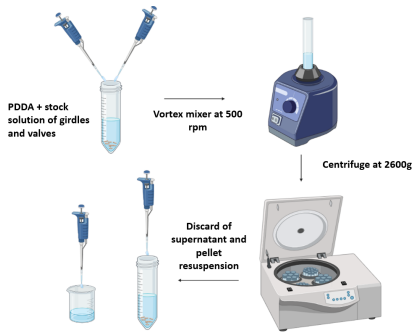

Figure 3.13: Main steps of the functionalization protocol.

The samples were then put on a glass cover slip (about 150 µl) and taken to the SEM-EDX laboratory for morphological characterization and detection of Ti. Figure 3.15 shows the elements present on the analyzed girdle band of Figure 3.14: this spectrum shows the existance of a Ti peak in the functionalized sample, meaning that the NPs have been attached to the surface. Wether the NPs were adsorpted (entered the pores) or just attached to the surface needed further analysis, shown in Figure 3.14: the analyzed girdle band in Figure 3.14.a is completely filled with NPs, suggesting a successful attachment and adsorption of NPs. The NPs, however, are more largely distributed on the valve, Figure 3.14.b, since the latter has a larger area. Some clusters were formed, but it can be seen the the NPs attached to the surface regardless. A peak of Al is also seen in this measurement; this is because the applied voltage had to be higher for the detection of Ti, leading to a detection of elements in deeper regions of the sample (see Appendix B for a brief explanation), including the stand that holds the samples, which is made of aluminum. It was, then, obvious the attachement and adsorption of the NPs on both structures. Unfortunately, girdle bands lying flat could not be found, which probably would have given a better picture of the adsorption of the NPs.

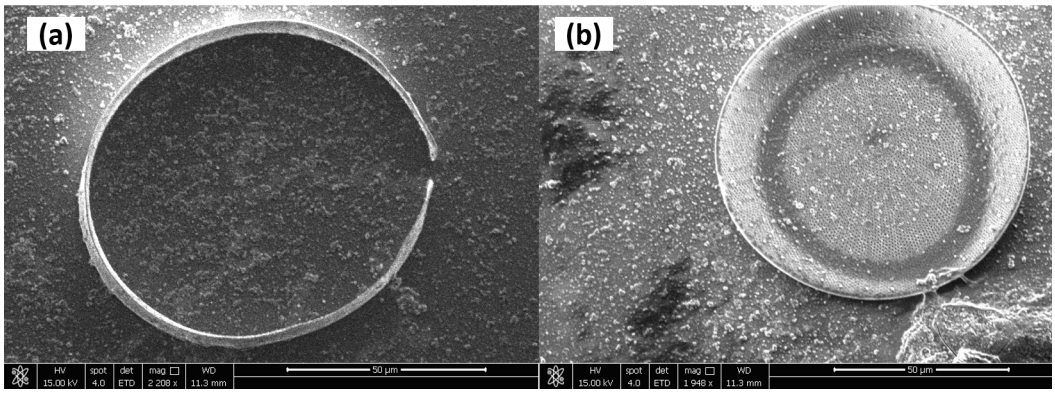

Figure 3.14: SEM of TiO_2 functionalized samples. (a) Girdle band. (b) Valve.

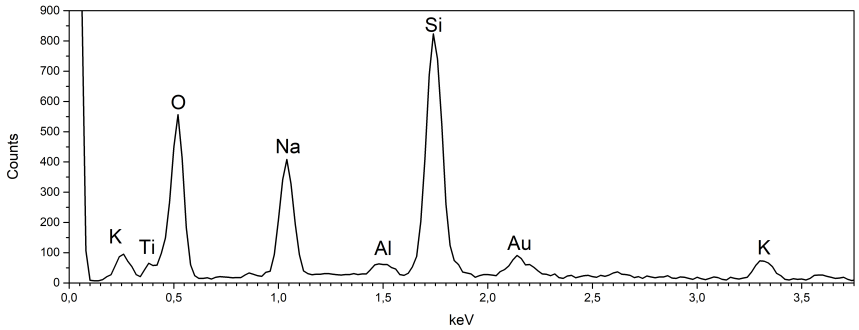

Figure 3.15: EDX measurements of a TiO_2 functionalized girdle band. The existance of a titanium peak ensures the success of the deposition.

3.2.2 Optical characterization of titanium dioxide functionalized girdle bands

Like on bare girdle bands, three different girdle bands, immersed in water, were measured. Figure 3.16 corresponds to the reflectance spectra obtained at normal incidence in comparison with the FDTD simulation, (a), and with the clean sample, (b). The simulation performed for this case considers TiO_2 NPs with a size of 67 nm randomly placed on top of the girdle-like structure, as well as inside the pores, instead of the conformal coating seen in Chapter 2 and Appendix A, therefore the difference in the results. Nonetheless, there is a good match between the simulation and the real measurements. More importantly, the average position of the central wavelength red-shifted $\sim$ 20 nm, in comparison with the clean sample, at an average central wavelength of 774 $\pm$ 3 nm, thus changing the position of the pPBG. This means that the surface has not only been successfully functionalized, as proven in the SEM-EDX measurements, but also that the photonic properties have been tuned.

Although a red-shift was detected, this was not as large as the Si_3N_4-coated girdle bands (analyzed in the next Subsection), despite the refractive index of titanium dioxide being greater than silicon nitride's. A couple of points might be the reason for this: the functionalization with TiO_2 is made with NPs instead of a thin-film. The Si_3N_4 thin-film is ideally coating the whole girdle band surface and even filling some

pores; the NPs, however, are randomly attached to the surface of girdle bands, which may leave some "empty" spots, i.e. without NPs, hence not fully coating the surface, leading to a rather low contribution on the part of the NPs to the effective refractive index of the sPhC. Also, the concentration of cleaned girdles and valves might not have been good enough, especially girdles. This can be improved, however: after every centrifuge and before the discard of the supernatant, the sample should settle at least 30-45 minutes in order for at least 70-80 % of present girdles to settle in the pellet. This also applies for the cleaning process.

Alternatively, the formation of clusters of NPs might also be a reason not only for the low red-shift, but also the low reflectance. These clusters are such that, when adsorpted at the surface of a girdle band, the pores are completely covered, thereby inhibiting the full sPhC nature of the structure. The utilised setup, that covers only a rather small portion of the NIR, only focusing on the visible range, can also be a factor, since it is inhibiting some potential features that these modified structures may exhibit in the NIR region.

Notwithstanding, the functionalization of the surfaces revealed to be successful, albeit some improvements will definately be needed. Figure 3.17 shows the angular dependency of the pPBG, showing the already expected blue-shift for higher angles of incidence, noticing that the second pattern does not appear in the measurement.

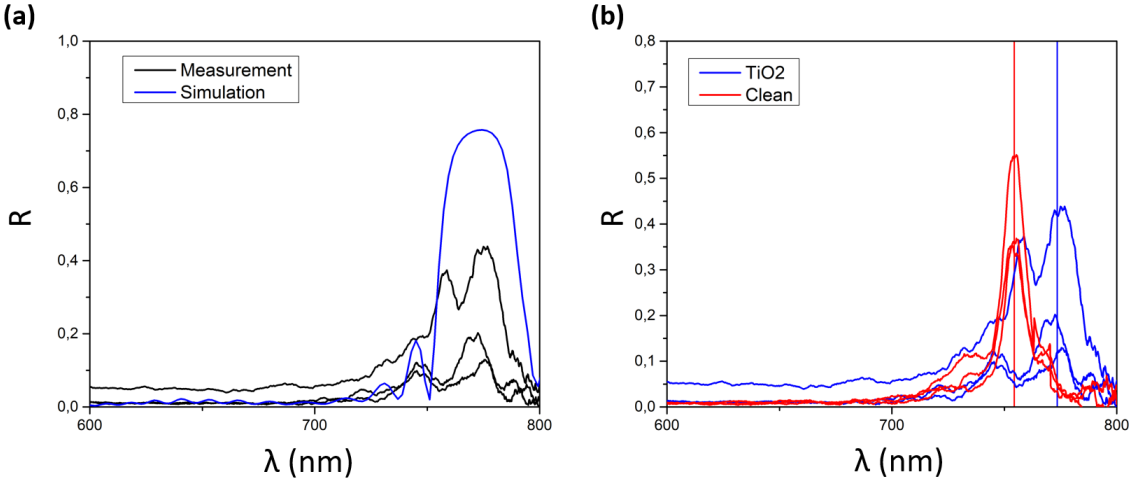

Figure 3.16: Experimental (a) and FDTD simulations (b) at normal incidence for TiO_2 functionalized girdle bands in water. The plot on the left compares the reflectance spectra of modified girdle bands TiO_2 NPs, in water, with the respective simulation. The dimensions and structure for the simulation were adapted with randomly placed nanoparticles all over the surface and inside the pores. The figure on the right compares the reflectance at normal incidence of modified girdle bands, with TiO_2 NPs, with clean girdle bands, both in water.

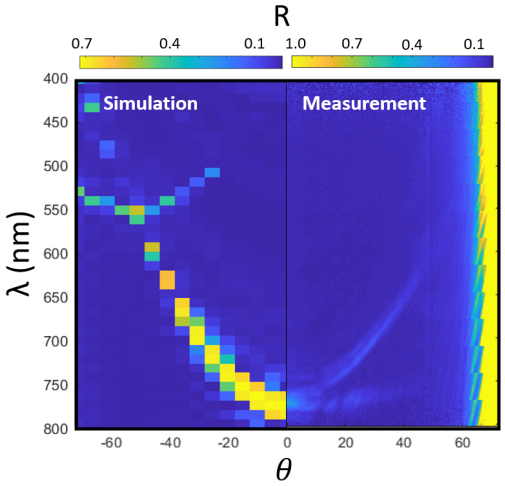

Figure 3.17: pPBG and in-plane diffraction of guided modes for TiO_2 functionalized girdle bands in water, shown by reflectance as a function of the angle of incidence and wavelength of light.

3.2.3 Silicon nitride coating

The second method was to grow a Si_3N_4 thin-film conformal to the external and internal (inside the pores) surfaces of girdle bands, as simulated in Chapter 2. The deposition was made by PECVD, because it allows us to have a conformal thin-film with a highly precise thickness. Moreover, the temperature achieved during the process is lower than regular CVD, since higher temperatures could permanently damage the silica structures. Four samples of clean girdle bands attached to a glass slide were placed on a silicon wafer with strips of kapton tape to ensure no air is between the sample and the wafer. Then, a thin-film of 30 nm was deposited, with a rate of growth of 45 nm/min and an associated error of 4%. This thickness was chosen based on the study of the theoretical photonic response in Chapter 2. The samples were then optically characterized (see Section 3.1.5), proceeded by 10 nm sputtering of gold for posterior SEM-EDX measurements.

Figure 3.18 corresponds to SEM images taken from a coated flat girdle band. Figure 3.18.a shows the measured coated flat girdle band and the corresponding FFT, displaying once again the ordered arrangement of the pores in a square lattice. Figure 3.18.b shows a closer view of the pores; here, the coating is clearly visible as thick rings around and slightly filling the pores. It is also noticed that some pores were completely filled, introducing some defects to the slab. The existance of silicon nitride in the structure is proven by the EDX measurements on Figure 3.19; the same elements are displayed in comparison with measurements made on the clean girdle, only this time with the addition of the nitrogen peak. It is also to be mentioned that two SEM measurements were made on this girdle band, with two different applied electrical potentials: 5 kV and 10 kV, since higher applied voltages allow to visualize the morphology underneath a certain material, as stated before.

This technique allowed to measure the thickness t of the silicon nitride film. Figures 3.18.c1 and 3.18.c2 show the same set of pores of the same girdle band, with applied potentials of 5 an 10 kV,

respectively. It is noticeable the difference in the pores, mainly the inexistance of the coating rings on the second image, corresponding thus to an image of "bare pores". The void radii, i.e. radii without any filling/coating, are r and R, respectively. The thickness of the film was measured by using the same approach as in the clear girdle band, only this time with a slight difference. The effective areas of 20 random pores were measured and the radius was obtained: $R = 82 \pm 3$ nm for the 10 kV measurement and $r = 54 \pm 3$ nm for the 5 kV one. This difference in the void radii confirms the pore filling with a thickness of $t = 28 \pm 6$ nm, which agrees with the value of 30 nm initially set for the deposition and the error associated.

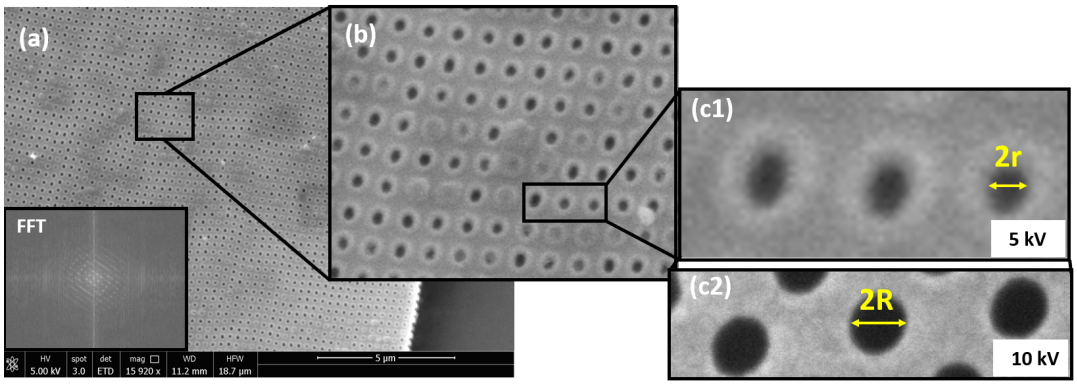

Figure 3.18: SEM of Si_3N_4-coated girdle bands. (a) SEM image of a silicon nitride coated girdle band lying flat and corresponding FFT. (b) Close view of the pores. It is clear the deposition, as thick rings on top of the pores. (c) Images taken at different applied voltages: 5 kV (c1) and 10 kV (c2).

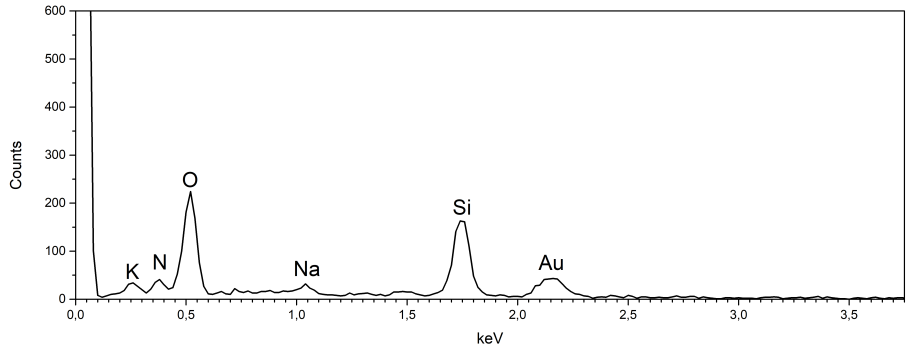

Figure 3.19: EDX measurements of a Si_3N_4-coated girdle band. The existance of a nitrogen peak ensures the success of the deposition.

3.2.4 Optical characterization of silicon nitride girdle bands

This Subsection takes a look at the optical measurements on the Si_3N_4-coated girdle bands. Figure 3.20 shows the reflectance at normal incidence for these samples in water, in comparison with the FDTD simulation (Figure 3.20.a) and with the clean girdle bands sample (Figure 3.20.b).

The FDTD simulation has a central wavelength, at the reflectance peak, at $\sim$ 790 nm; this simulation is slightly different from the particular case studied in Chapter 2, since it uses real parameters, extracted from the SEM measurements. It also considers the pores to not be completly filled, since the real geometry of diatom girdle bands displays a void that interconnects the pores on the inside (see Figure 1.7.b, the darker pores on the rhombic chambers of the pores). It is also worth to mention that these samples were optically characterized without the gold coating.

Three different girdle bands were measured, showing an average central wavelength of 787 $\pm$ 8 nm. The position of the pPBG red-shifted about 30 nm relatively to the clean girdle bands sample (Figure 3.20.b). This observation serves as a first proof that the insertion of materials on these silica structures modifies its optical properties. Since Si_3N_4 has a higher refractive index than silica, the effective refractive index of the sPhC increases, leading to the red-shift of the pPBG, as seen in Figure 3.20.b; the coloured vertical lines represent the mean central wavelength of clean (red) and Si_3N_4-coated girdle bands (blue). The disparity on the measurements between different girdle bands from the coated sample were a little bit higher, since this effect tends to be more sensible when the refractive index contrast between the bulk of the sPhC and the immersion medium is higher, as well as fact that some pores may have been completely filled and/or even the existance of defects, i.e. regions on the slab without pores.

In Figure 3.21, it is seen how the pPBG behaves at variable angles of incidence. As expected, it blue-shifts for higher angles of incidence. It is also noticeable the appearence of a second pattern at $\theta \approx 20^\circ$ that red-shifts towards a maximum at $\theta \approx 40^\circ$, crossing the pPBG, blue-shifting afterwards. The existance of this second pattern, also noted in the FDTD simulation, corresponds to the in-plane diffraction of guided modes and its behaviour is very similar to the pPBG. This must mean that this pattern is itself a pPBG that appears at oblique incidence, more precisely at $\Gamma - M$ direction or vice-versa. The appearence of this secondary pattern is also an indicative of the 2D symmetry of the girdle band and seems to also be an enhanced feature when the refractive index of the sPhC, and thus the refractive index contrast, is higher relatively to the clean sample, which does not exhibit said feature.

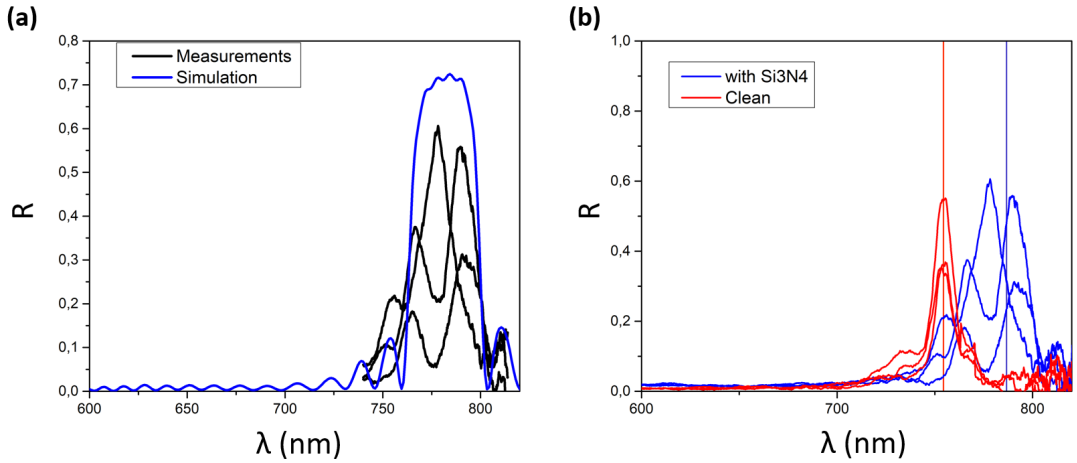

Figure 3.20: Experimental (a) and FDTD simulations (b) at normal incidence for Si_3N_4-coated girdle bands in water. The plot on the left compares the reflectance spectra of girdle bands covered with Si_3N_4, in water, with the respective simulation. The dimensions used for the simulation were adapted from the values given by the morphological characterization of the sample. The figure on the right compares the reflectance at normal incidence of Si_3N_4 covered girdle bands with clean girdle bands, both in water.

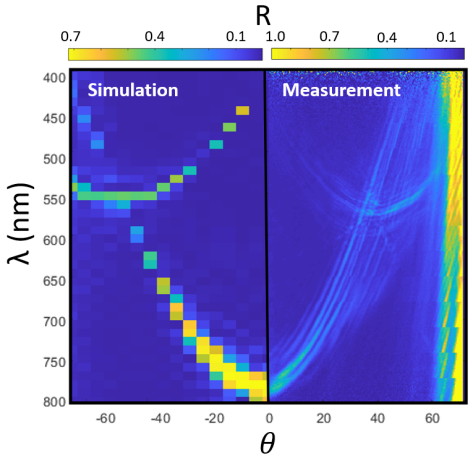

Figure 3.21: pPBG and in-plane diffraction of guided modes for Si_3N_4-coated girdle bands in water, shown by reflectance as a function of the angle of incidence and wavelength of light.

3.3 Conclusions

This Chapter contains the experimental portion of the Thesis, from the types of measurements performed throughout to the preparation of samples for such measurements, as well as the corresponding results. The very first step was to expand the diatom culture once a month in order to have enough samples, proceeded by counting the average number of healthy diatoms in 1 ml of solution. One of the most important steps was the cleaning of diatom frustules, involving the removal of the organic matter and separation of these silicate structures into girdle bands and valves. For this purpose, two successful protocols were employed. Clean samples were then morphologically characterized. After the treatment and study of clean samples, it was proceeded the modification of clean samples, with the main focus

being the girdle bands, in order to detect any changes in the photonic response. Si_3N_4 and TiO_2 were the selected materials for this purpose, since their relatively high refractive indices have the potential to modify with ease the photonic properties of girdle bands. The modification of girdle band surfaces was achieved with two different methods: a solution of clean girdle bands was functionalized with TiO_2 NPs following an adsorption protocol, while other clean samples were used as scaffolds for the growth of a thin-film of Si_3N_4 by PECVD. These samples, along with clean girdle bands as control samples, underwent optical characterization, using a FIS setup, to detect any difference on the position of the pPBG. The pPBG was studied by measuring the reflectance spectrum in the $\Gamma - X$ direction, i.e. at normal incidence, and as a function of the angle and wavelength of incident light. As expected, modified girdle bands showed considerable different photonic responses in comparison with the clean ones, mainly the red-shift on the central wavelength and thus on the pPBG itself. The average positions of the measured pPBG for each sample are in displayed in Figure 3.22, where it compares the spectral position of the pPBG of the three measured samples. The angular measurements showed a blue-shift for all measured samples, agreeing with Bragg-Snell's Law. These measurements also showed additional features that would only appear at oblique incidence, like the existance of a second reflectance pattern at higher angles and lower wavelengths, symbolizing the diffraction of in-plane waveguiding modes.

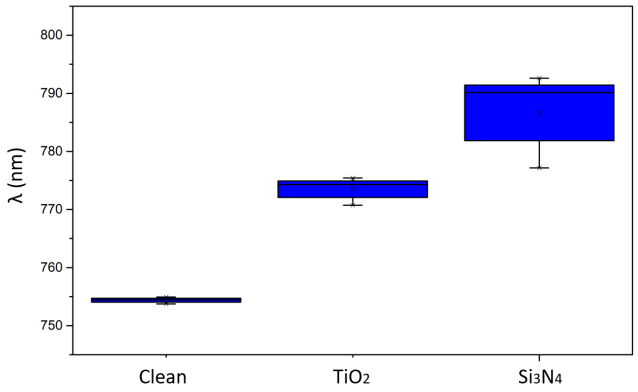

Figure 3.22: Spectral position of the pPBG, as a measurement of the central wavelength at the reflectance peak, for all three samples in water.

4

Conclusions and Future Work

4.1 Conclusions

This Thesis is focused on the study of naturally produced materials from microalgae biosilica for light harvesting applications. Photonic crystals have shown in previous works that they can be used as alternatives to thick c-Si films, as they possess reduced dimensions and are relatively less costly, not to mention the efficienct enhancement they provide due to their ability to manipulate light at ease. A high demand of production of these structures can be a negative point however, since fabrication of PhC involves advanced cleanroom techniques, and the requirements of highly rigorous dimensions can make the process time consuming and even a bit costly, which would be contradicting to one of their positive aspects.

Diatoms have previously been studied for photonic applications due to their high porous silica exosqueletons, i.e. frustules, and even implemented in dye-sensitized solar cells (DSSC), reavealing an efficiency enhancement. The work performed here, however, promotes the use of isolated girdle bands instead of the whole frustule or even valves themselves, as these have already been commonly reported in previous studies, wether for their use in photonic applications or others, whereas girdle bands have certainly been overlooked. The advantages of the use of girdle bands are that, aside from their small size in comparison to valves and whole frustules, they exhibit periodic patterns of pores that are highly preserved within different specimens of the same species. In an optical point of view, this results in preserved spectral responses within a specific diatom species at low refractive index contrasts, i.e. when immersed in water or other fluid with a refractive index close to silica's. Girdle bands, due to their structural nature, have been referred to as natural sPhC, where the pattern of pores leads to the creation of pPBG. The pPBG created by these structures were analyzed as reflectance measurements at normal and oblique incidence, with water as the immersion medium. This way, with a low refractive index contrast, allowed to only analyze the effect on changing the effective refractive index of the structures, without worrying about the size of the pores. Firstly, a theoretical study was made. FDTD simulations were carried out, simulating the photonic response of girdle-like structures. Bare and modified girdle bands were simulated. The modification of these girdle-like structures consisted on coating the structures with conformal films of higher refractive index materials of choice. This would lead to an increase on the effective refractive

index and consequently a change in the photonic response of the system. Once done, real measurements proceeded with clean girdle bands. After studying the real photonic response of clean girdle bands, it was proceeded the actual modification of said structures, by surface functionalization, in order to change the effective refractive index. From the simulations, this change leads to a different spectral position of the central wavelength at the reflectance peak. Firstly, girdle bands were functionalized with TiO_2 NPs following an adsorption protocol; then, samples of clean girdle bands were coated with a thin film of Si_3N_4. This latter technique has been performed in 2D PhC in previous studies. After morphological characterization to ensure the presence of these new elements, the modified samples underwent optical characterization. The obtained results, although not completely matching the ones from the simulations performed beforehand, revealed a red-shift on the central wavelength at the reflectance peak, meaning a change in the position of the pPBG to higher wavelengths.

Therefore, girdle bands from diatoms revealed to be highly suitable for photonic and sensing applications due to their sPhC optical response. The high availability of these structures, combined with the low-cost and facilitated and rapid production under controlled conditions, paves the way for the development of photonic devices with reduced cleanroom techniques, serving as alternatives to nanofabricated PhC.

Further investigations such as testing the operation of girdle bands on actual solar cell devices and the insertion of Si were not performed in this work but we believe that the results presented here pave the way for obtaining girdle bands whose optical properties can be tailored for such applications.

4.2 Future Work

As stated before, the study of the photonic properties of girdle bands from diatoms has been a bit overlooked, considering their fascinating and preserved sPhC properties under low refractive index contrast conditions. The work on these bio-nanostructures must then be taken to the next level.

Other species of diatoms, like *C. wailesii*, have been studied regarding their plasmonic properties. The work performed throughout this Thesis could also be applied to these latter species of diatoms, since the corresponding girdle bands exhibit an interesting hexagonal arrangement of pores.

Modification of lattice properties of these structures on-demand and during cell growth, for a certain specific application, would also be a huge boost on this field of research. To date, there has not been developments regarding actual manipulation of girdle bands lattice properties, since pores can have different sizes within a certain species, causing different optical responses, and the process of biosilification is still widely unknown. To overcome these two obstacles, other strategies can be explored, such as *in vivo* doping during frustule synthesis. This will alter the refractive index contrast of the bulk biosilica and induce teratological alterations to the structure. This latter approach could also mitigate the trip to the cleanroom for growing thin-films of higher refractive index materials on top of girdle bands, performed in this Thesis for simplification purposes.

Bibliography

[1] N. S. Lewis and D. G. Nocera. “Powering the planet: Chemical challenges in solar energy utilization”. In: *Proceedings of the National Academy of Sciences* 103.43 (2006), pp. 15729–15735. doi: 10.1073/pnas.0603395103.

[2] T. Mayr et al. “Light Harvesting as a Simple and Versatile Way to Enhance Brightness of Luminescent Sensors”. In: *Analytical Chemistry* 81.15 (2009). PMID: 19552422, pp. 6541–6545. doi: 10.1021/ac900662x.

[3] G. J. Hedley, A. Ruseckas, and I. D. W. Samuel. “Light Harvesting for Organic Photovoltaics”. In: *Chemical Reviews* 117 (Dec. 2016), pp. 796–837. doi: 10.1021/acs.chemrev.6b00215. (Visited on 08/09/2022).

[4] X. Li et al. “Photoinduced Electron Transfer and Hole Migration in Nanosized Helical Aromatic Oligoamide Foldamers”. In: *Journal of the American Chemical Society* 138 (Sept. 2016). doi: 10.1021/jacs.6b05668.

[5] X.-H. Jin et al. “Long-range exciton transport in conjugated polymer nanofibers prepared by seeded growth”. In: *Science* 360.6391 (2018), pp. 897–900. doi: 10.1126/science.aar8104.

[6] V. Vohra. “Natural Dyes and Their Derivatives Integrated into Organic Solar Cells”. In: *Materials* 11 (Dec. 2018), p. 2579. doi: 10.3390/ma11122579.

[7] L. Olejko and I. Bald. “FRET efficiency and antenna effect in multi-color DNA origami-based light harvesting systems”. In: *RSC Adv.* 7 (May 2017), pp. 23924–23934. doi: 10.1039/C7RA02114C.

[8] J.-L. Bredas, E. H. Sargent, and G. D. Scholes. 2017. doi: 10.1038/nmat4767.

[9] M. Grätzel. “Dye-sensitized solar cells”. In: *Journal of Photochemistry and Photobiology C: Photochemistry Reviews* 4.2 (2003), pp. 145–153. issn: 1389-5567. doi: https://doi.org/10.1016/S1389-5567(03)00026-1.

[10] B. Qiu et al. “Efficient Solar Light Harvesting CdS/Co9 S8 Hollow Cubes for Z-Scheme Photocatalytic Water Splitting”. In: *Angewandte Chemie (International ed. in English)* 56 (Jan. 2017). doi: 10.1002/anie.201612551.

[11] B. Liu et al. “Photocurrent generation following long-range propagation of organic exciton–polaritons”. In: *Optica* 9.9 (Sept. 2022), pp. 1029–1036. doi: 10.1364/OPTICA.461025.

[12] S. P. Sreenilayam et al. “Chapter 14 - Photonic crystals-based light-trapping approach in solar cells”. In: *Nano-Optics*. Ed. by S. Thomas et al. Micro and Nano Technologies. Elsevier, 2020, pp. 337–345. isbn: 978-0-12-818392-2. doi: https://doi.org/10.1016/B978-0-12-818392-2.00014-7.

[13] S. Bhattacharya and S. John. “Photonic crystal light trapping: Beyond 30% conversion efficiency for silicon photovoltaics”. In: *APL Photonics* 5.2 (2020), p. 020902. doi: 10.1063/1.5128664.

[14] M. A. Green et al. “Solar cell efficiency tables (Version 53)”. In: *Progress in Photovoltaics: Research and Applications* 27.1 (2019), pp. 3–12. doi: https://doi.org/10.1002/pip.3102.

[15] J. Ramanujam and U. P. Singh. “Copper indium gallium selenide based solar cells – a review”. In: *Energy Environ. Sci.* 10 (6 2017), pp. 1306–1319. doi: 10.1039/C7EE00826K.

[16] P. Sinha and A. Wade. “Addressing Hotspots in the Product Environmental Footprint of CdTe Photovoltaics”. In: *IEEE Journal of Photovoltaics* 8.3 (2018), pp. 793–797. doi: 10.1109/JPHOTOV.2018.2802786.

[17] J. Zou et al. “Rational Design and Simulation of Two-Dimensional Perovskite Photonic Crystal Absorption Layers Enabling Improved Light Absorption Efficiency for Solar Cells”. In: *Energies* 14 (Apr. 2021), p. 2460. doi: 10.3390/en14092460.

[18] W. S. Yang et al. “High-performance photovoltaic perovskite layers fabricated through intramolecular exchange”. In: *Science* 348.6240 (2015), pp. 1234–1237. doi: 10.1126/science.aaa9272.

[19] E. Yablonovitch. “Inhibited Spontaneous Emission in Solid-State Physics and Electronics”. In: *Phys. Rev. Lett.* 58 (20 May 1987), pp. 2059–2062. doi: 10.1103/PhysRevLett.58.2059.

[20] E. Yablonovitch. “Inhibited Spontaneous Emission in Solid-State Physics and Electronics”. In: *Phys. Rev. Lett.* 58 (20 May 1987), pp. 2059–2062. doi: 10.1103/PhysRevLett.58.2059.

[21] S. John. “Strong localization of photons in certain disordered dielectric superlattices”. In: *Phys. Rev. Lett.* 58 (23 June 1987), pp. 2486–2489. doi: 10.1103/PhysRevLett.58.2486.

[22] W. Liu, H. Ma, and A. Walsh. “Advance in photonic crystal solar cells”. In: *Renewable and Sustainable Energy Reviews* 116 (2019), p. 109436. issn: 1364-0321. doi: https://doi.org/10.1016/j.rser.2019.109436.

[23] F. Wang et al. “Effective modulation of the photonic band gap based on Ge/ZnS one-dimensional photonic crystal at the infrared band”. In: *Optical Materials* 75 (2018), pp. 373–378. issn: 0925-3467. doi: https://doi.org/10.1016/j.optmat.2017.10.053. url: https://www.sciencedirect.com/science/article/pii/S0925346717306869.

[24] N. Ashcroft and N. Mermin. *Solid State Physics*. Fort Worth: Saunders College Publishing, 1976.

[25] C. Kittel. *Introduction to Solid State Physics*. Wiley, 2004. isbn: 9780471415268.

[26] S. Singla, P. Singal, and P. Sidhar. “Orientation sensitivity of a hexagonal lattice photonic crystal fiber”. In: Dec. 2017, pp. 16–20. doi: 10.1109/CCUBE.2017.8394159.

[27] E. Yablonovitch. “Photonic Crystals: Semiconductors of Light”. In: *Scientific American* 285 (Jan. 2002), pp. 47–51, 54. doi: 10.1038/scientificamerican1201-46.

[28] J. D. Joannopoulos et al. *Photonic crystals: Molding the flow of light*. Second. Princeton University Press, 2008.

[29] J. I. L. Chen et al. “Amplified Photochemistry with Slow Photons”. In: *Advanced Materials* 18.14 (2006), pp. 1915–1919. doi: https://doi.org/10.1002/adma.200600588.

[30] P. Chen et al. “Optimal design of one-dimensional photonic crystal back reflectors for thin-film silicon solar cells”. In: *Journal of Applied Physics* 116.6 (2014), p. 064508. doi: 10.1063/1.4893180.

[31] P. Bermel et al. “Improving thin-film crystalline silicon solar cell efficiencies with photonic crystals”. In: *Opt. Express* 15.25 (Dec. 2007), pp. 16986–17000. doi: 10.1364/OE.15.016986.

[32] J. Krügener et al. “Photonic crystals for highly efficient silicon single junction solar cells”. In: *Solar Energy Materials and Solar Cells* 233 (2021), p. 111337. issn: 0927-0248. doi: https://doi.org/10.1016/j.solmat.2021.111337.

[33] T. Vasileiou et al. “Light absorption enhancement and radiation hardening for triple junction solar cell through bio-inspired nano-structures”. In: *Bioinspiration & Biomimetics* 16 (June 2021). doi: 10.1088/1748-3190/ac095b.

[34] H. Inan et al. “Photonic crystals: emerging biosensors and their promise for point-of-care applications”. In: *Chem. Soc. Rev.* 46 (2 2017), pp. 366–388. doi: 10.1039/C6CS00206D.

[35] F. Parandin et al. “Two-Dimensional photonic crystal Biosensors: A review”. In: *Optics & Laser Technology* 144 (2021), p. 107397. issn: 0030-3992. doi: https://doi.org/10.1016/j.optlastec.2021.107397.

[36] Y.-n. Zhang, Y. Zhao, and R.-q. Lv. “A review for optical sensors based on photonic crystal cavities”. In: *Sensors and Actuators A: Physical* 233 (2015), pp. 374–389. issn: 0924-4247. doi: https://doi.org/10.1016/j.sna.2015.07.025.

[37] C. Fenzl, T. Hirsch, and O. S. Wolfbeis. "Photonic crystals for chemical sensing and biosensing". In: *Angewandte Chemie (International ed. in English)* 53(13) (2014), pp. 3318–3335. doi: https://doi.org/10.1002/anie.201307828.

[38] E. Chow et al. "Three-dimensional control of light in a two-dimensional photonic crystal slab". In: *Nature* 407 (Nov. 2000), pp. 983–6. doi: 10.1038/35039583.

[39] P. Viktorovitch et al. "3D harnessing of light with 2.5D photonic crystals". In: *Laser & Photonics Reviews* 4.3 (2010), pp. 401–413. doi: https://doi.org/10.1002/lpor.200910009.

[40] C. Becker et al. "5 × 5 cm2 silicon photonic crystal slabs on glass and plastic foil exhibiting broadband absorption and high-intensity near-fields". In: *Scientific Reports* 4 (2014).

[41] R. Gansch et al. "Higher order modes in photonic crystal slabs". In: *Opt. Express* 19.17 (Aug. 2011), pp. 15990–15995. doi: 10.1364/OE.19.015990.

[42] A. I. Nashed et al. "Efficient Optical Modeling of VCSELs using Full-Vectorial FDFD method". In: *2019 International Conference on Numerical Simulation of Optoelectronic Devices (NUSOD)*. 2019, pp. 39–40. doi: 10.1109/NUSOD.2019.8806850.

[43] A. Yetisen et al. "Color-Selective 2.5 Dimensional Holograms on Large-Area Flexible Substrates for Sensing and Multilevel Security". In: *Advanced Optical Materials* 4 (June 2016). doi: 10.1002/adom.201600162.

[44] R. Poushimin and T. Jalali. "Radiation losses in photonic crystal slab waveguide to enhance LEDs efficiency". In: *Superlattices and Microstructures* 122 (2018), pp. 426–433. issn: 0749-6036. doi: https://doi.org/10.1016/j.spmi.2018.05.010.

[45] X. Zhu et al. "Structural Color Control of CoFeB-Coated Nanoporous Thin Films". In: *Coatings* 11.9 (2021). issn: 2079-6412. doi: 10.3390/coatings11091123.

[46] A. Lonergan, B. Murphy, and C. O'Dwyer. "Photonic Stopband Tuning in Metallo-Dielectric Photonic Crystals". In: *ECS Journal of Solid State Science and Technology* 10 (Aug. 2021), p. 085001. doi: 10.1149/2162-8777/ac19c5. (Visited on 09/25/2022).

[47] B. Suthar et al. "Tuning of photonic band gaps in one dimensional chalcogenide based photonic crystal". In: *Optics Communications* 285.6 (2012), pp. 1505–1509. issn: 0030-4018. doi: https://doi.org/10.1016/j.optcom.2011.10.047.

[48] M. G. Han et al. "Full Color Tunable Photonic Crystal from Crystalline Colloidal Arrays with an Engineered Photonic Stop-Band". In: *Advanced Materials* 24.48 (2012), pp. 6438–6444. doi: https://doi.org/10.1002/adma.201203211.

[49] E. Aluicio-Sarduy et al. *Structural color tuning in 1D photonic crystals with electric field and magnetic field*. 2018. doi: 10.48550/ARXIV.1804.04491. url: https://arxiv.org/abs/1804.04491.

[50] E. Otón et al. “Orientation control of ideal blue phase photonic crystals”. In: *Scientific Reports* 10 (June 2020). doi: 10.1038/s41598-020-67083-6.

[51] M. D. A. Rahman, S. M. Said, and S. Balamurugan. “Blue phase liquid crystal: strategies for phase stabilization and device development”. In: *Science and Technology of Advanced Materials* 16 (2015).

[52] R. Manda et al. “Electrically tunable photonic band gap structure in monodomain blue-phase liquid crystals”. In: *NPG Asia Materials* 12 (Dec. 2020). doi: 10.1038/s41427-020-0225-8.

[53] Y. Li and S.-T. Wu. “Polarization independent adaptive microlens with a blue-phase liquid crystal”. In: *Opt. Express* 19.9 (Apr. 2011), pp. 8045–8050. doi: 10.1364/OE.19.008045.

[54] R. Manda et al. “Ultra-fast switching blue phase liquid crystals diffraction grating stabilized by chiral monomer”. In: *Journal of Physics D: Applied Physics* 51.18 (Apr. 2018), p. 185103. doi: 10.1088/1361-6463/aab83f.

[55] R. Ozaki and H. Moritake. “Wavelength and bandwidth tunable photonic stopband of ferroelectric liquid crystals”. In: *Opt. Express* 20.6 (Mar. 2012), pp. 6191–6196. doi: 10.1364/OE.20.006191.

[56] J.-G. Park et al. “Photonic-crystal hydrogels with a rapidly tunable stop band and high reflectivity across the visible”. In: *Opt. Mater. Express* 7.1 (Jan. 2017), pp. 253–263. doi: 10.1364/OME.7.000253.

[57] H. Yin et al. “Amorphous diamond-structured photonic crystal in the feather barbs of the scarlet macaw”. In: *Proceedings of the National Academy of Sciences* 109.27 (2012), pp. 10798–10801. doi: 10.1073/pnas.1204383109.

[58] R. Vaz, M. F. Frasco, and M. G. F. Sales. “Photonics in nature and bioinspired designs: sustainable approaches for a colourful world”. In: *Nanoscale Adv.* 2 (11 2020), pp. 5106–5129. doi: 10.1039/D0NA00445F.

[59] M. Jacobs et al. “Photonic multilayer structure of Begonia chloroplasts enhances photosynthetic efficiency”. In: *Nature plants* 2.11 (Oct. 2016), p. 16162. issn: 2055-0278. doi: 10.1038/nplants.2016.162.

[60] E. Bukhanov et al. “The Role of Periodic Structures in Light Harvesting”. In: *Plants* 10.9 (2021). issn: 2223-7747. doi: 10.3390/plants10091967.

[61] M. Lopez-Garcia et al. “Light-induced dynamic structural color by intracellular 3D photonic crystals in brown algae”. In: *Science Advances* 4.4 (2018), eaan8917. doi: 10.1126/sciadv.aan8917.

[62] J. W. Goessling, W. P. Wardley, and M. Lopez-Garcia. “Highly Reproducible, Bio-Based Slab Photonic Crystals Grown by Diatoms”. In: *Advanced Science* 7.10 (2020), p. 1903726. doi: https://doi.org/10.1002/advs.201903726.

[63] J. W. Galusha et al. “Study of natural photonic crystals in beetle scales and their conversion into inorganic structures via a sol–gel bio-templating route”. In: *J. Mater. Chem.* 20 (7 2010), pp. 1277–1284. doi: 10.1039/B913217A.

[64] C. Barrera-Patiño et al. “Photonic effects in natural nanostructures on Morpho cypris and Greta oto butterfly wings”. In: *Scientific Reports* 10 (Apr. 2020). doi: 10.1038/s41598-020-62770-w.

[65] J. Teyssier et al. “Photonic crystals cause active color change in chameleons”. In: *Nature communications* 6 (Mar. 2015), p. 6368. doi: 10.1038/ncomms7368.

[66] Girard, Vincent et al. “Thai amber: insights into early diatom history?” In: *BSGF - Earth Sci. Bull.* 191 (2020), p. 23. doi: 10.1051/bsgf/2020028.

[67] R. Gordon et al. “The Glass Menagerie: diatoms for novel applications in nanotechnology”. In: *Trends in Biotechnology* 27 (2009), p. 116.

[68] J. W. Goessling et al. “Biosilica slab photonic crystals as an alternative to cleanroom nanofabrication?” In: *Faraday Discuss.* 223 (0 2020), pp. 261–277. doi: 10.1039/D0FD00031K.

[69] A. A. 1. J. 2014. *The Air You’re Breathing? A Diatom Made That*. livescience.com. url: https://www.livescience.com/46250-teasing-apart-the-diatom-genome.html.

[70] G. Hasle et al. *Identifying Marine Diatoms and Dinoflagellates*. Elsevier Science, 1996. isbn: 9780080534411.

[71] X. Sun, Y. Zhang, and D. Losic. “Diatom silica, an emerging biomaterial for energy conversion and storage”. In: *J. Mater. Chem. A* 5 (May 2017). doi: 10.1039/C7TA02045G.

[72] J. W. Goessling et al. “Differences in the optical properties of valve and girdle band in a centric diatom”. In: *Interface Focus* 9.1 (2019), p. 20180031. doi: 10.1098/rsfs.2018.0031.

[73] P. Assmy et al. “Auxospore formation by the silica-sinking, oceanic diatom Fragilariopsis kerguelensis (Bacillariophyceae)”. In: *Journal of Phycology* 42 (Sept. 2006), pp. 1002–1006. doi: 10.1111/j.1529-8817.2006.00260.x.

[74] Z. Wang, D. Gong, and J. Cai. “Diatom Frustule Array for Flow-Through Enhancement of Fluorescent Signal in a Microfluidic Chip”. In: *Micromachines* 12.9 (2021). issn: 2072-666X. doi: 10.3390/mi12091017.

[75] D. Losic et al. “Pore Architecture of Diatom Frustules: Potential Nanostructured Membranes for Molecular and Particle Separations”. In: *Journal of Nanoscience and Nanotechnology* 6 (May 2006), pp. 982–989. doi: 10.1166/jnn.2006.174.

[76] E. S. Karaman et al. “Fabrication of supercapacitors and flexible electrodes using biosilica from cultured diatoms”. In: *Materials Today Energy* 11 (2019), pp. 166–173. issn: 2468-6069. doi: https://doi.org/10.1016/j.mtener.2018.11.004.

[77] Z. Wang et al. “Cultured Diatoms Suitable for the Advanced Anode of Lithium Ion Batteries”. In: *ACS Sustainable Chemistry & Engineering* 9.2 (2021), pp. 844–852. doi: 10.1021/acssuschemeng.0c07484.

[78] F. de Matteis et al. “Photonic Application of Diatom Frustules”. In: *THERMEC 2016*. Vol. 879. Materials Science Forum. Trans Tech Publications Ltd, Feb. 2017, pp. 419–423. doi: 10.4028/www.scientific.net/MSF.879.419.

[79] T. M. W. J. Bandara et al. “Diatom frustules enhancing the efficiency of gel polymer electrolyte based dye-sensitized solar cells with multilayer photoelectrodes”. In: *Nanoscale Adv.* 2 (1 2020), pp. 199–209. doi: 10.1039/C9NA00679F.

[80] M. Villani et al. “Transforming diatomaceous earth into sensing devices by surface modification with gold nanoparticles”. In: *Micro and Nano Engineering* 2 (2019), pp. 29–34. issn: 2590-0072. doi: https://doi.org/10.1016/j.mne.2018.11.006.

[81] M. Pannico et al. “Electroless Gold-Modified Diatoms as Surface-Enhanced Raman Scattering Supports”. In: *Nanoscale Research Letters* 11 (Dec. 2016), p. 315. doi: 10.1186/s11671-016-1539-x.

[82] I. Rea and L. De Stefano. “Recent Advances on Diatom-Based Biosensors”. In: *Sensors* 19.23 (2019). issn: 1424-8220. doi: 10.3390/s19235208.

[83] K. Squire et al. “Multi-scale Photonic Crystal Enhanced Core-Shell Plasmonic Nanomaterial for Rapid Vapor-Phase Detection of Explosives”. In: *ACS Applied Nano Materials* XXXX (Jan. 2020). doi: 10.1021/acsanm.9b02399.

[84] S. Phogat et al. “Diatom mediated smart drug delivery system”. In: *Journal of Drug Delivery Science and Technology* 63 (2021), p. 102433. issn: 1773-2247. doi: https://doi.org/10.1016/j.jddst.2021.102433.

[85] T. Fuhrmann-Lieker et al. “Diatoms as living photonic crystals”. In: *Applied Physics B* 78 (Feb. 2004), pp. 257–260. doi: 10.1007/s00340-004-1419-4.

[86] W. P. Wardley, J. W. Goessling, and M. Lopez-Garcia. *Plasmonic crystals with highly ordered lattice geometries using continuous metal films on diatom bio-silica as both scaffolds and sources of tuneability*. 2021. url: https://arxiv.org/abs/2108.01602.

[87] G. Mayonado et al. “Investigation Of The Bragg-Snell Law In Photonic Crystals”. In: July 2015. doi: 10.1119/bfy.2015.pr.015.

[88] K. Luke et al. “Broadband mid-infrared frequency comb generation in a Si3N4 microresonator”. In: *Opt. Lett.* 40.21 (Nov. 2015), pp. 4823–4826. doi: 10.1364/OL.40.004823.

[89] J. R. DeVore. “Refractive Indices of Rutile and Sphalerite”. In: *J. Opt. Soc. Am.* 41.6 (June 1951), pp. 416–419. doi: 10.1364/JOSA.41.000416.

[90] B. Tatian. “Fitting refractive-index data with the Sellmeier dispersion formula”. In: *Appl. Opt.* 23.24 (Dec. 1984), pp. 4477–4485. doi: 10.1364/AO.23.004477.

[91] J. F. Galisteo-López et al. “Optical study of the pseudogap in thickness and orientation controlled artificial opals”. In: *Phys. Rev. B* 68 (11 Sept. 2003), p. 115109. doi: 10.1103/PhysRevB.68.115109.

[92] C.-J. Wu, Y.-C. Hsieh, and H.-T. Hsu. “Tunable photonic band gap in a doped semiconductor photonic crystal in near infrared region”. In: *Progress In Electromagnetics Research* 114 (Jan. 2011). doi: 10.2528/PIER11011808.

[93] A. Gevorgyan. “Effects of angle of incidence and polarization in the chiral photonic crystals”. In: *Optics and Spectroscopy (English translation of Optika i Spektroskopiya)* 105 (Oct. 2008), pp. 624–632. doi: 10.1134/S0030400X08100172.

[94] A. Lakhtakia. “General schema for the Brewster conditions”. In: *Optik* 90 (1992), pp. 184–186.

[95] M. Kucki and T. Fuhrmann-Lieker. “Staining diatoms with rhodamine dyes: control of emission colour in photonic biocomposites”. In: *Journal of The Royal Society Interface* 9 (2011), pp. 727–733.

[96] R. R. L. Guillard and P. E. Hargraves. “Stichochrysis immobilis is a diatom, not a chrysophyte”. In: *Phycologia* 32.3 (1993), pp. 234–236. doi: 10.2216/i0031-8884-32-3-234.1.

[97] G. R. Hasle and G. A. Fryxell. “Diatoms: Cleaning and Mounting for Light and Electron Microscopy”. In: *Transactions of the American Microscopical Society* 89.4 (1970), pp. 469–474. issn: 00030023.

[98] F. Gomez et al. “Calcium Carbonate Precipitation in Diatom-rich Microbial Mats: The Laguna Negra Hypersaline Lake, Catamarca, Argentina”. In: *Journal of Sedimentary Research* 88 (June 2018). doi: 10.2110/jsr.2018.37.

[99] T. Christensen. *Alger i naturen og i laboratoriet*. Nucleus, 1982. isbn: 9788787661379.

[100] N. Lundholm, N. Daugbjerg, and Ø. Moestrup. “Phylogeny of the Bacillariaceae with emphasis on the genus Pseudo-nitzschia (Bacillariophyceae) based on partial LSU rRDNA.” In: *European Journal of Phycology* 37 (Mar. 2002), pp. 115–134. doi: 10.1017/S096702620100347X.

[101] M. Abdollahi and S. Nikfar. “Hydrochloric Acid”. In: *Encyclopedia of Toxicology (Third Edition)*. Ed. by P. Wexler. Third Edition. Oxford: Academic Press, 2014, pp. 960–963. isbn: 978-0-12-386455-0. doi: https://doi.org/10.1016/B978-0-12-386454-3.00735-1.

[102] S. Leslie and J. Mitchell. “Removing gold coating from sem samples”. In: *Palaeontology* 50 (Sept. 2007), pp. 1459–1461. doi: 10.1111/j.1475-4983.2007.00718.x.

[103] T. Schmauder et al. “Applications of Highly Reflective Silver Coatings for Car Headlamp Reflectors”. In: (Oct. 2022).

[104] W. P. Wardley, J. W. Goessling, and M. Lopez-Garcia. “Measuring Photonics in Photosynthesis: Combined Micro-Fourier Image Spectroscopy and Pulse Amplitude Modulated Chlorophyll Fluorimetry at the Micrometre-Scale”. In: *Biomimetics* 7.3 (2022). issn: 2313-7673. doi: 10.3390/biomimetics7030107. url: https://www.mdpi.com/2313-7673/7/3/107.

[105] D. Mazia. “Adhesion of cells to surfaces coated with polylysine. Applications to electron microscopy”. In: *The Journal of Cell Biology* 66 (July 1975), pp. 198–200. doi: 10.1083/jcb.66.1.198.

[106] J. Ouwehand et al. “Titania-functionalized diatom frustules as photocatalyst for indoor air purification”. In: *Applied Catalysis B: Environmental* 226 (2018), pp. 303–310. issn: 0926-3373. doi: https://doi.org/10.1016/j.apcatb.2017.12.063.

[107] Y. Lang et al. “Integration of TiO2 into the diatom Thalassiosira weissflogii during frustule synthesis”. In: *Scientific reports* 3 (Nov. 2013), p. 3205. doi: 10.1038/srep03205.

[108] H.-P. Boehm. “The Chemistry of Silica. Solubility, Polymerization, Colloid and Surface Properties, and Biochemistry. VonR. K. Iler. John Wiley and Sons, Chichester 1979.” In: *Angewandte Chemie* 92 (Apr. 1980), pp. 328–328. doi: 10.1002/ange.19800920433.

[109] J. Stetefeld, S. A. McKenna, and T. R. Patel. “Dynamic light scattering: a practical guide and applications in biomedical sciences”. In: *Biophysical Reviews* 8 (2016), pp. 409–427.

[110] A. Abdullah and A. Mohammed. “Scanning Electron Microscopy (SEM): A Review”. In: Jan. 2019.

[111] N. Jain et al. “Metal Deposition: Plasma-Based Processes”. In: Jan. 2016, p. 19. doi: 10.1081/E-EPLT-120053919.

A

Simulations

Appendix A contains all simulations executed throughout the whole Thesis to study the photonic response of the girdle band structure when coated with different higher refractive index materials with different thicknesses. Such simulations presented down below include reflectance and transmittance at normal incidence, angular reflectance and the corresponding bandstructures. It is also explained the approach used for calculating the bandstructures in Section A.3. The refractive indices for Si_3N_4, TiO_2 and Si were calculated for $\lambda = 625$ nm using the following dispersion formulas:

$$n^2_{Si3N4} = 1 + \frac{3.0249\lambda^2}{\lambda^2 - 0.1353406^2} + \frac{40314\lambda^2}{\lambda^2 - 1239.842^2}$$

$$n^2_{TiO2} = 5.913 + \frac{0.2441}{\lambda^2 - 0.0803}$$

$$n^2_{Si} = 1 + \frac{10.6684293\lambda^2}{\lambda^2 - 0.301516485^2} + \frac{0.0030434748\lambda^2}{\lambda^2 - 1.13475115^2} + \frac{1.54133408\lambda^2}{\lambda^2 - 1104^2}$$

A.1 Normal incidence

- **Silicon nitride**

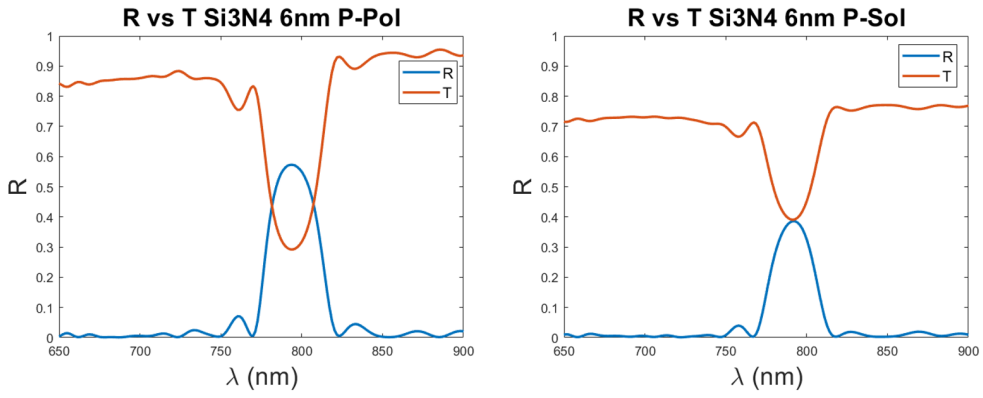

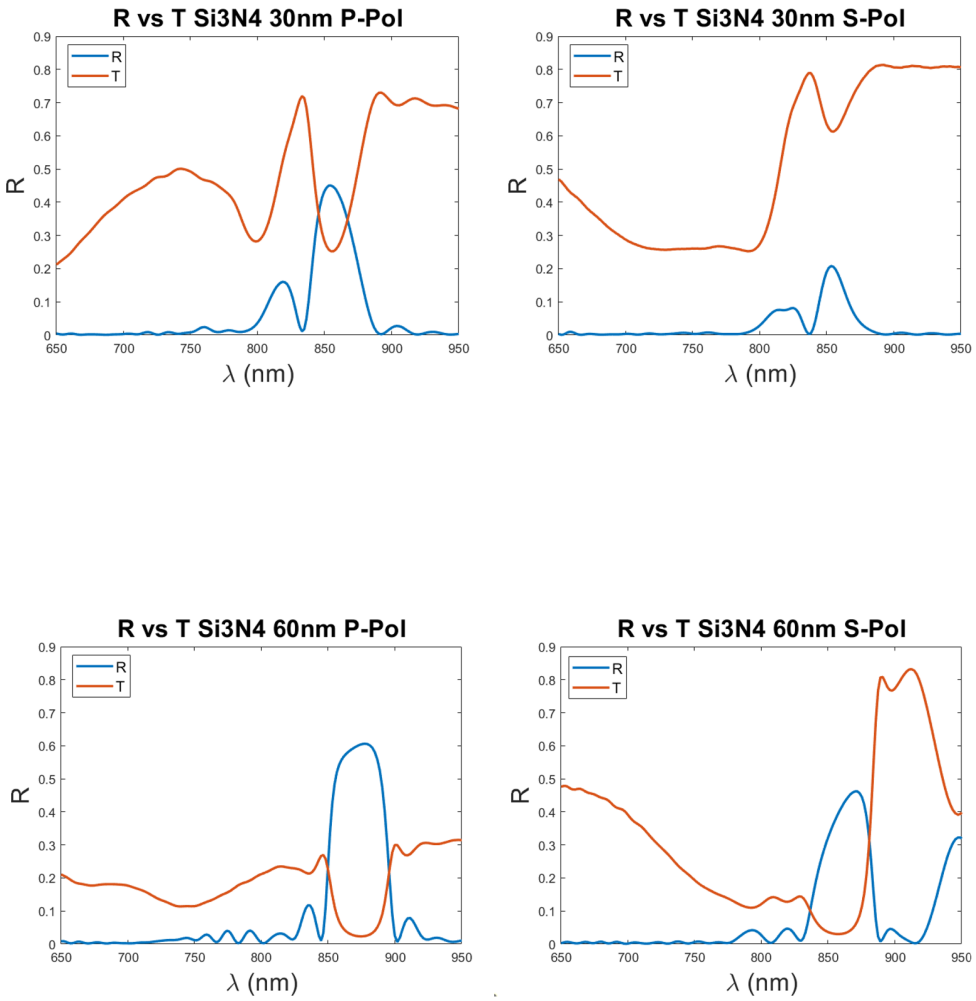

Figure A.1: Simulated reflectance (in blue) and transmittance (in orange) spectra for Si_3N_4 girdle band structures immersed in water for both polarizations and all three thicknesses.

- **Titanium dioxide**

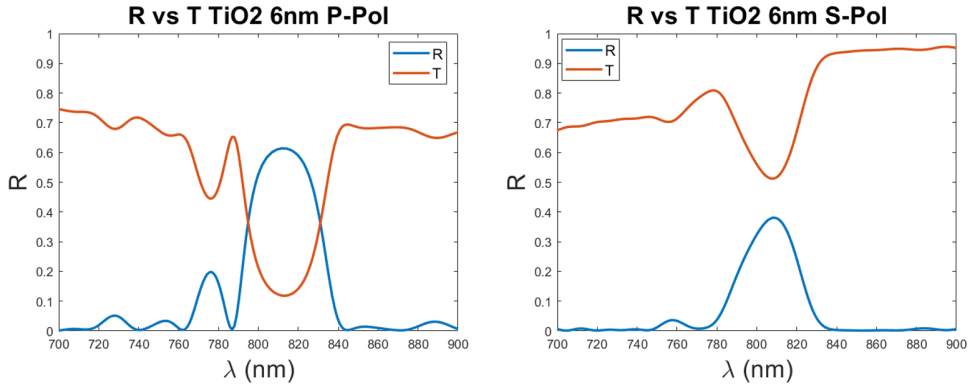

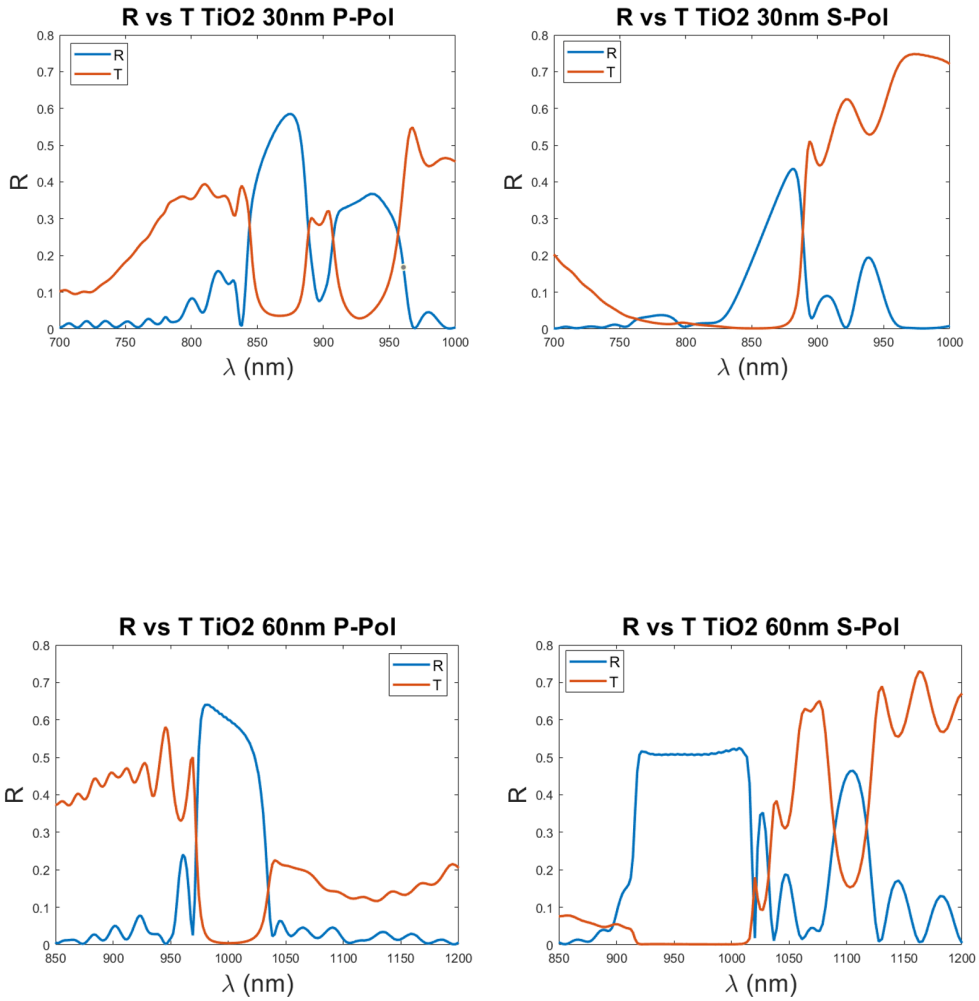

Figure A.2: Simulated reflectance (in blue) and transmittance (in orange) spectra for TiO_2 girdle band structures immersed in water for both polarizations and all three thicknesses.

- **Silicon**

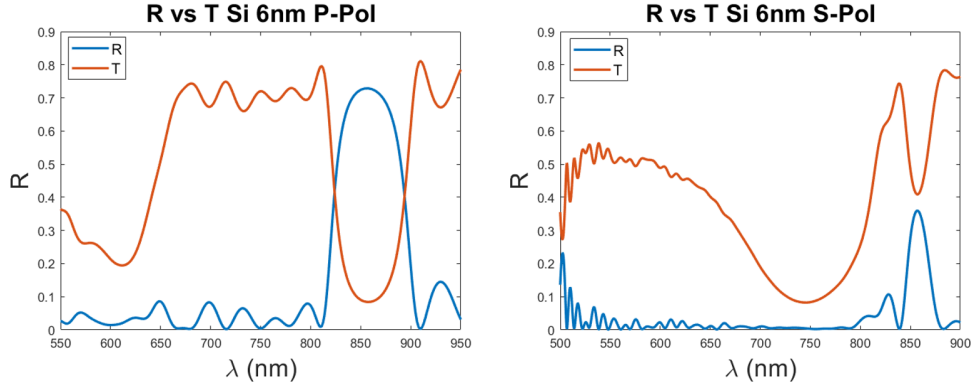

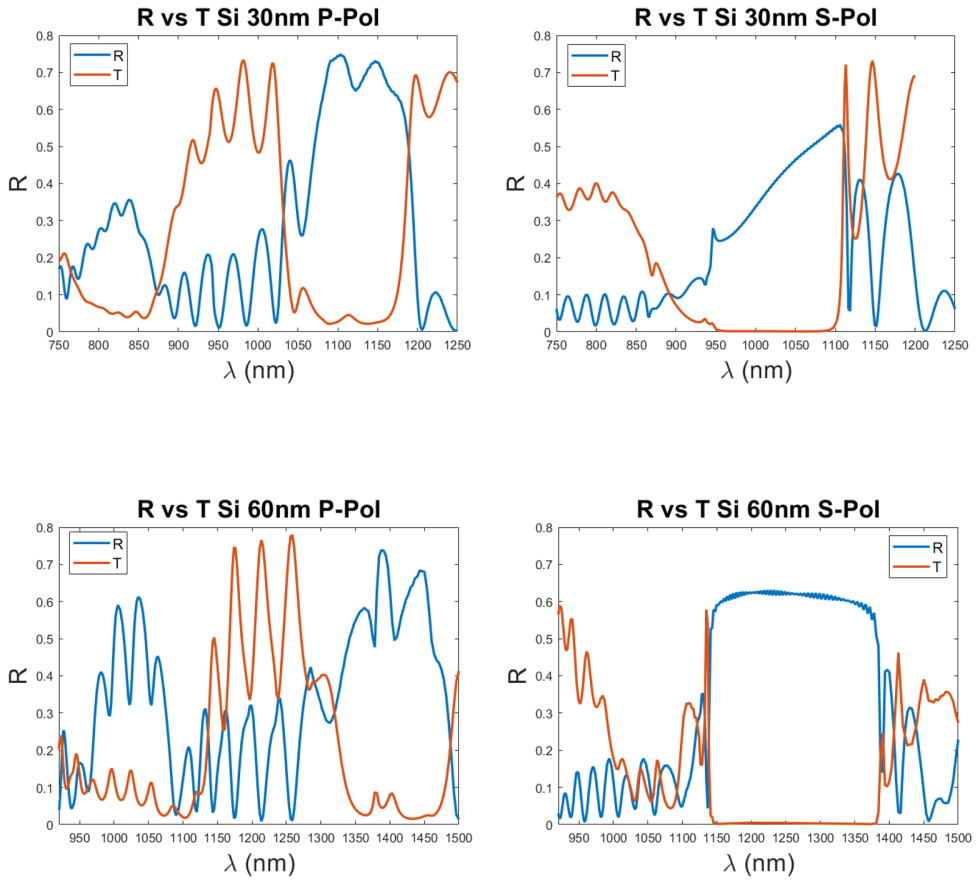

Figure A.3: Simulated reflectance (in blue) and transmittance (in orange) spectra for Si girdle band structures immersed in water for both polarizations and all three thicknesses.

Table A.1: Simulated pPBG properties at normal incidence for all three materials

	Si_3N_4			TiO_2			Si		
p-pol	6 nm	30 nm	60 nm	6 nm	30 nm	60 nm	6 nm	30 nm	60 nm
λ_{peak} (nm)	794.9	857.0	872.7	812.7	868.1	1001.4	844.8	1126.2	1395.6
FWHM (nm)	29.9	26.0	37.8	33.4	35.6	67.3	51.6	134.3	150.8
	Si_3N_4			TiO_2			Si		
s-Pol	6 nm	30 nm	60 nm	6 nm	30 nm	60 nm	6 nm	30 nm	60 nm
λ_{peak} (nm)	791.5	854.9	863.9	806.6	872.3	969.3	857.5	1061.7	1167.2
FWHM (nm)	25.8	16.5	35.9	29.5	36.2	118.8	18.9	163.5	146.8

A.2 Angular reflectance

- **Silicon nitride**

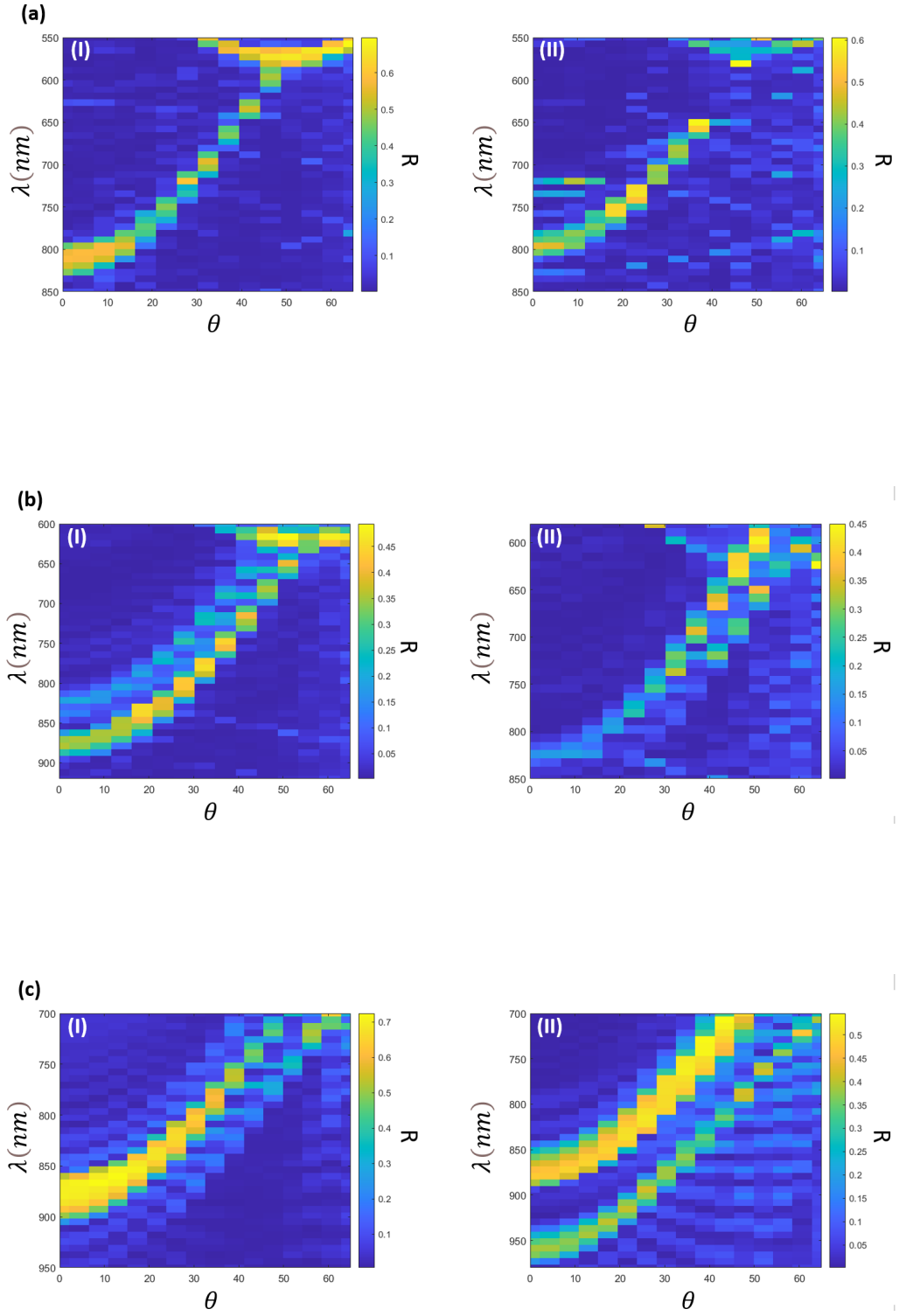

Figure A.4: Simulated angular reflectance for Si_3N_4 coated girdle band structures immersed in water. Coatings have thicknesses of (a) 6 nm, (b) 30 nm and (c) 60 nm. Items (I) and (II) correpond to *p*- and *s*-polarizations, respectively.

- **Titanium dioxide**

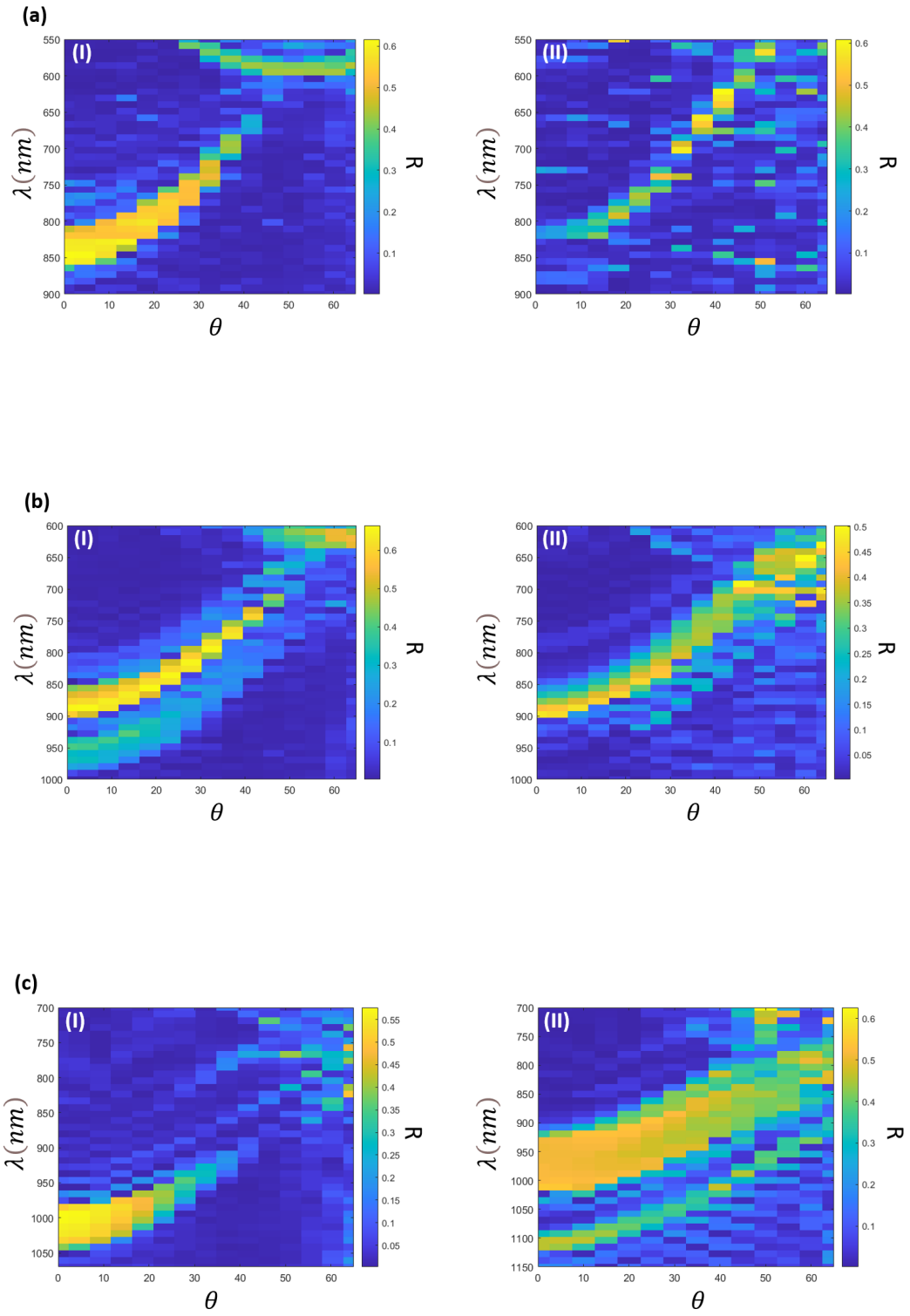

Figure A.5: Simulated angular reflectance for TiO_2 coated girdle band structures immersed in water. Coatings have thicknesses of (a) 6 nm, (b) 30 nm and (c) 60 nm. Items (I) and (II) correpond to *p*- and *s*-polarizations, respectively.

- **Silicon**

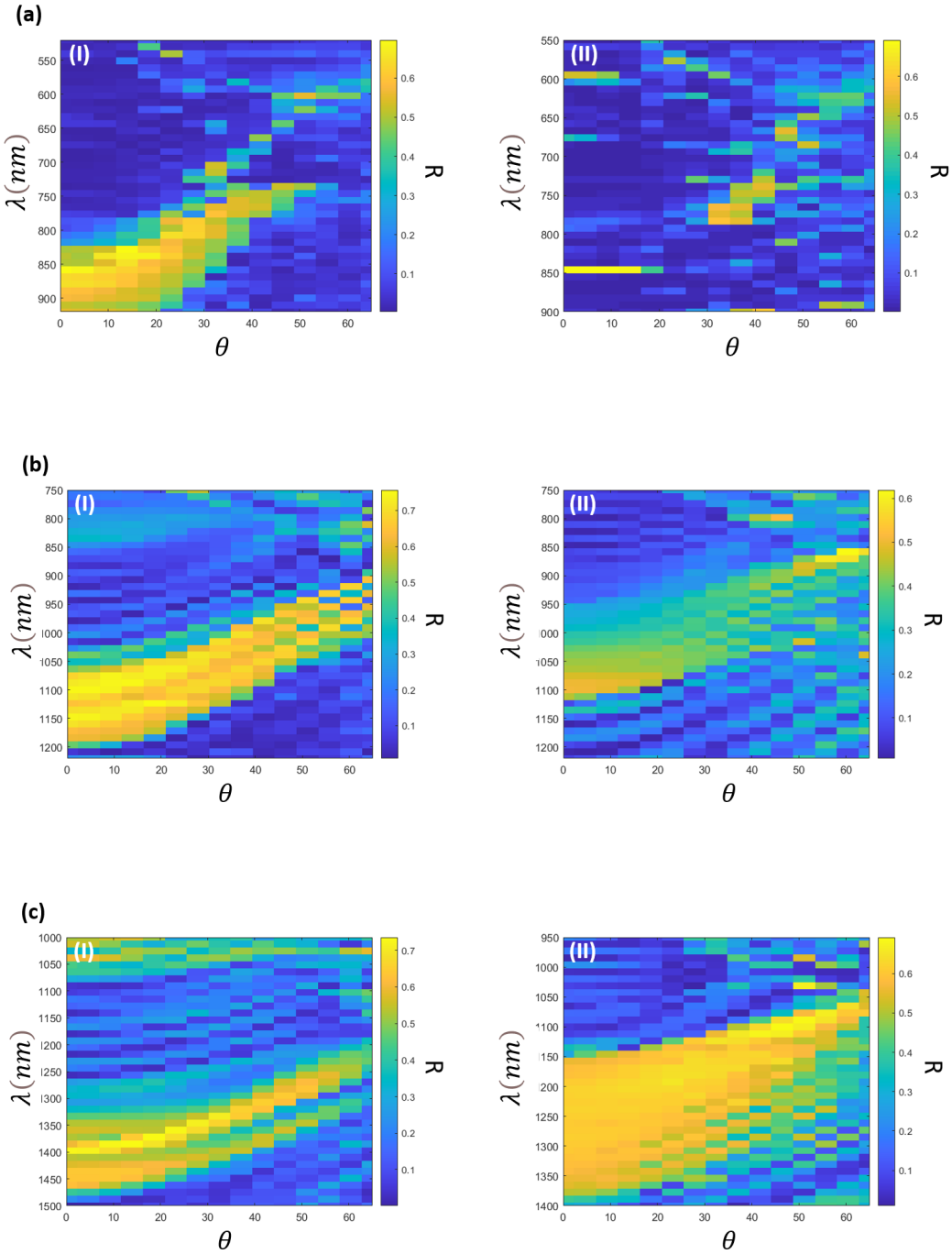

Figure A.6: Simulated angular reflectance for Si coated girdle band structures immersed in water. Coatings have thicknesses of (a) 6 nm, (b) 30 nm and (c) 60 nm. Items (I) and (II) correpond to *p*- and *s*-polarizations, respectively.

As stated in Subsection 2.2.5, in Chapter 2, the refractive index is extracted by using a linear fit on a plot containing the squared values of the central wavelengths and the squared sines of the respective angles, $\lambda^2 = \lambda^2(\sin\theta^2)$. The values displayed in Table A.2 correspond to the effective refractive index calculated for both polarizations in the form of average and standard deviation

$$n = \bar{n} \pm \sigma$$

where

$$\bar{n} = \frac{n_p + n_s}{2}$$

is an average from the refractive indices from *p*- and *s*-polarizations, n_p and n_s respectively, and

$$\sigma = \sqrt{\frac{(n_p - \bar{n})^2 + (n_s - \bar{n})^2}{2}}$$

is the standard deviation of the "sample".

Table A.2: Effective refractive indices for all three materials

	Si_3N_4	TiO_2	Si
6 nm	1.41 ± 0.01	1.47 ± 0.01	1.49 ± 0.02
30 nm	1.50 ± 0.04	1.57 ± 0.01	1.925 ± 0.004
60 nm	1.538 ± 0.005	1.73 ± 0.02	2.33 ± 0.12

A.3 Bandstructures

The bandstructures of the studied structures were calculated by simplifying the complex geometry of the pores into a two-dimensional problem, i.e. by approximating them as cylinders that occupy the same volume in a unit cell with an average-weighted refractive index $\tilde{n}$. The steps are illustrated in Figure A.7. As known from Goessling *et al* [62], a single pore occupies about 30% of the total volume of a unit cell.

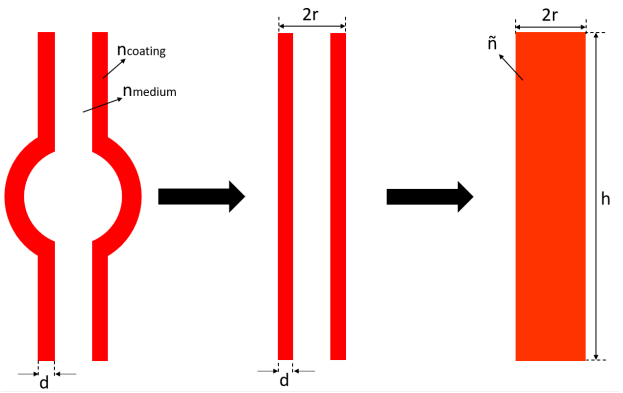

Figure A.7: Transformation process of girdle bands pores into equivalent cylinders.

The volume of a unit cell is

$$V_{cell} = a^2 h$$

where a is the lattice constant and h the height, which corresponds to the height of the pore. From this, the radius of the equivalent cylinder (in orange) can be calculated, knowing that its volume, $V_{pore} = \pi r^2 h$ where r is the radius of the cylinder, is 30% of the cell's volume, $V_{pore} = 30\% V_{cell}$, and solving for r

$$r = \sqrt{30\% \times \frac{a^2}{\pi}}$$

The refractive index of the cylinder is a weighted-average of the coating material and immersion medium refractive indices, $n_{coating}$ and n_{medium}, respectively

$$\tilde{n} = \frac{\sum_i n_i w_i}{\sum_i w_i} \tag{A.1}$$

The weights in Equation A.1 are the volume fractions occupied by the coating, V_{coat} and by the immersion medium sans coating, V_{medium}, over the total volume of the equivalent pore (middle sketch in Figure A.7). From this, the weighted-average refractive index of the equivalent cylindrical pore can be calculated:

$$\begin{aligned} \tilde{n} &= (n_{medium}.V_{medium} + n_{coating}.V_{coating}) \times \frac{1}{V_{pore}} \\ &= n_{medium}.\frac{V_{medium}}{V_{pore}} + n_{coating}.\frac{V_{pore} - V_{medium}}{V_{pore}} \end{aligned} \tag{A.2}$$

where $V_{medium} = \pi(r-d)^2 h$. This way, $\tilde{n}$ is a function of the refractive index and thickness of the coating material. Below are displayed the calculated bandstructers following this approach.

- **Silicon nitride**

(a)

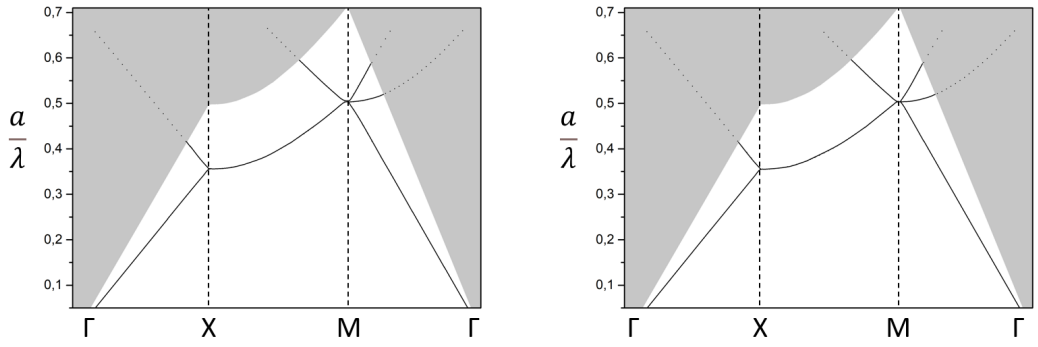

(b)

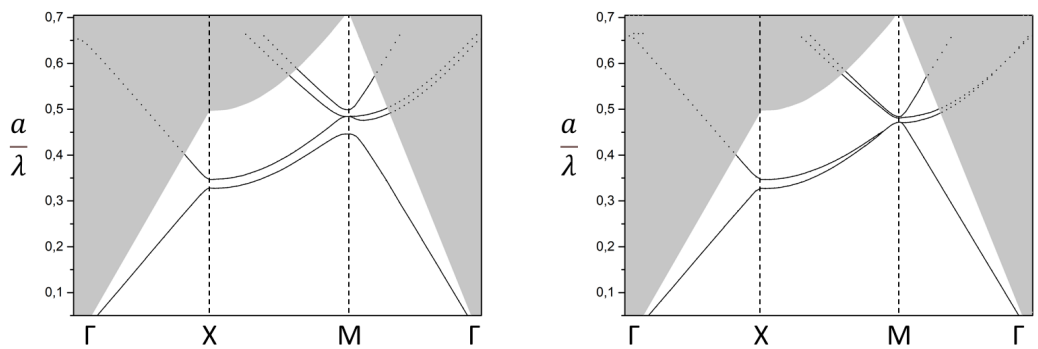

(c)

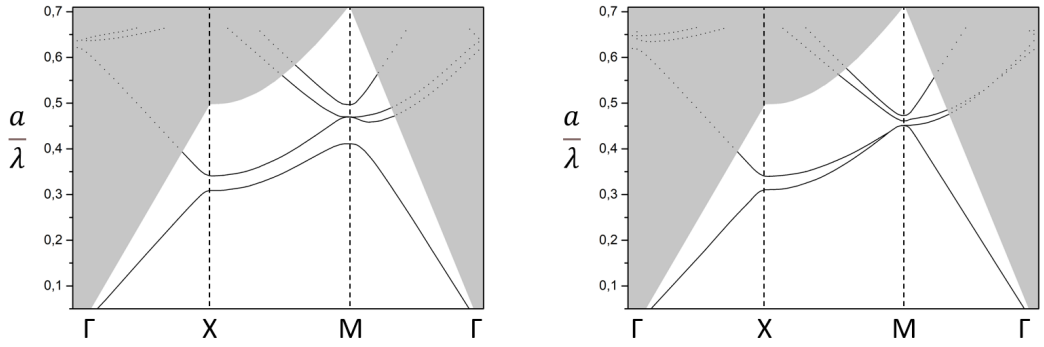

Figure A.8: Bandstructures for Si_3N_4 coated girdle bands (with the aforementioned conditions and immersed in water), displaying guided modes (solid lines), below the light cone, and modes that couple with radiation modes (dashed lines) in the light cone region. TE modes are displayed at the left and TM modes at the right. Coating thicknesses: (a) 6 nm, (b) 30 nm and (c) 60 nm.

- **Titanium dioxide**

(a)

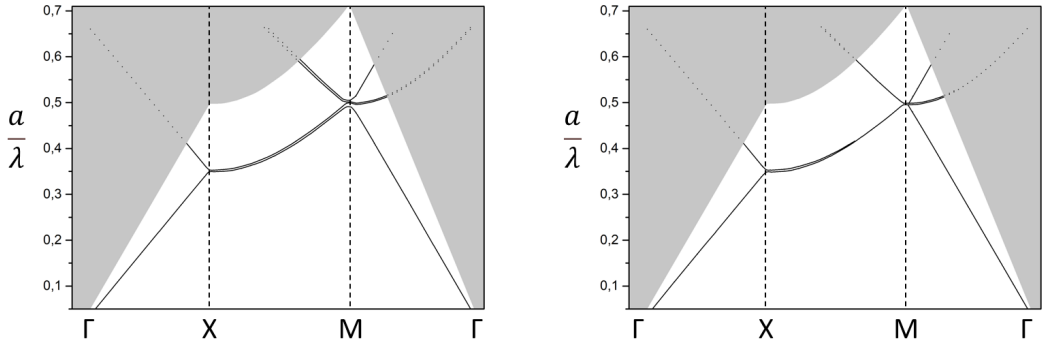

(b)

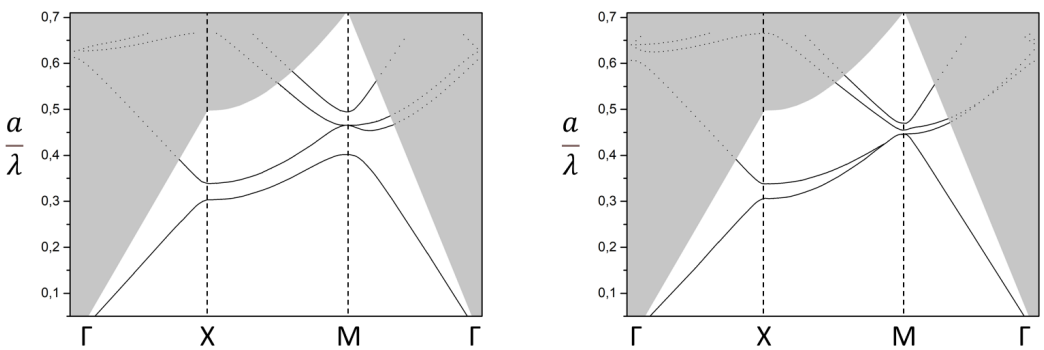

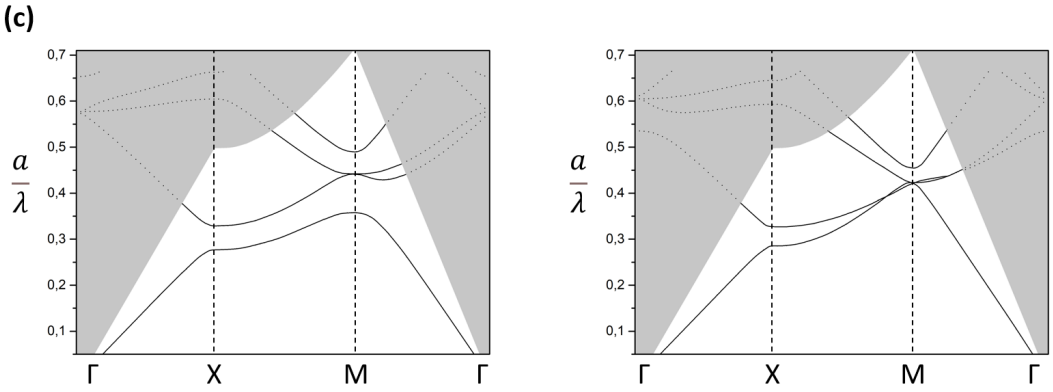

Figure A.9: Bandstructures for TiO_2 coated girdle bands (with the aforementioned conditions and immersed in water), displaying guided modes (solid lines), below the light cone, and modes that couple with radiation modes (dashed lines) in the light cone region. TE modes are displayed at the left and TM modes at the right. Coating thicknesses: (a) 6 nm, (b) 30 nm and (c) 60 nm.

- **Silicon**

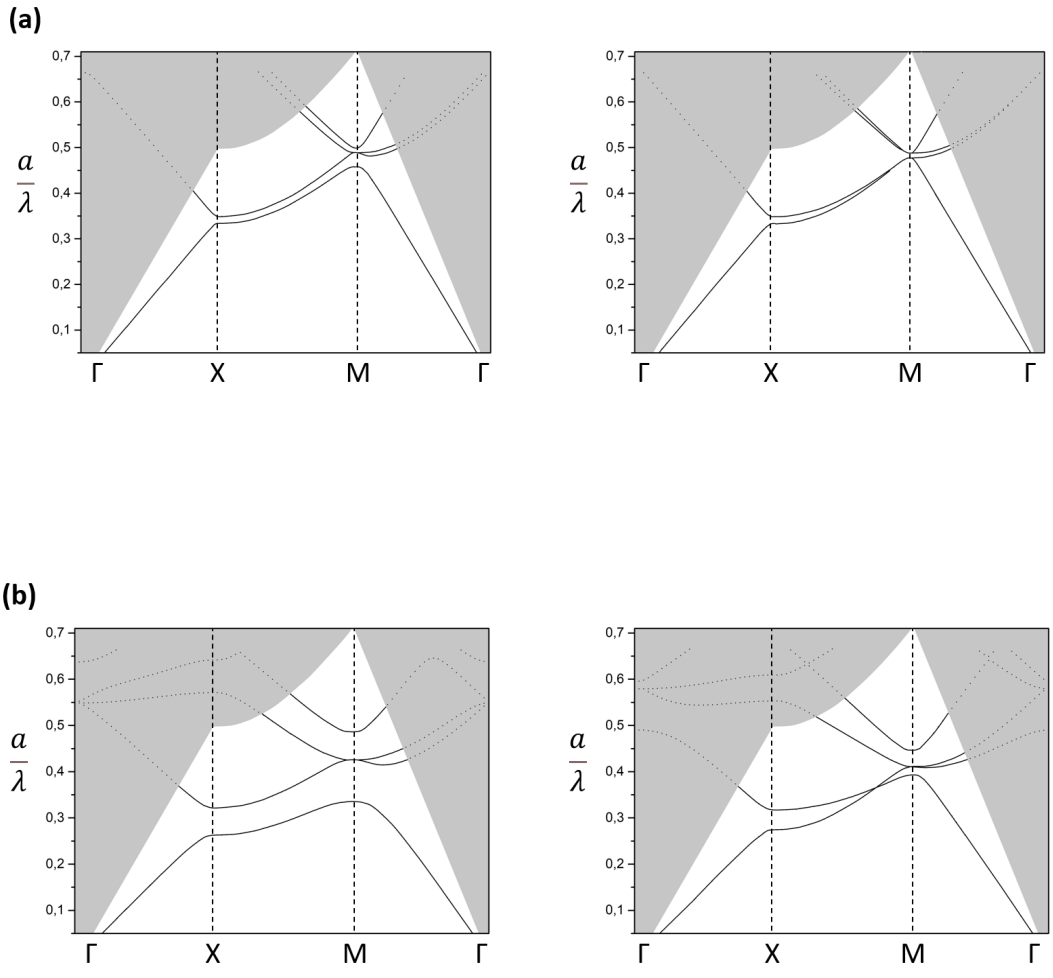

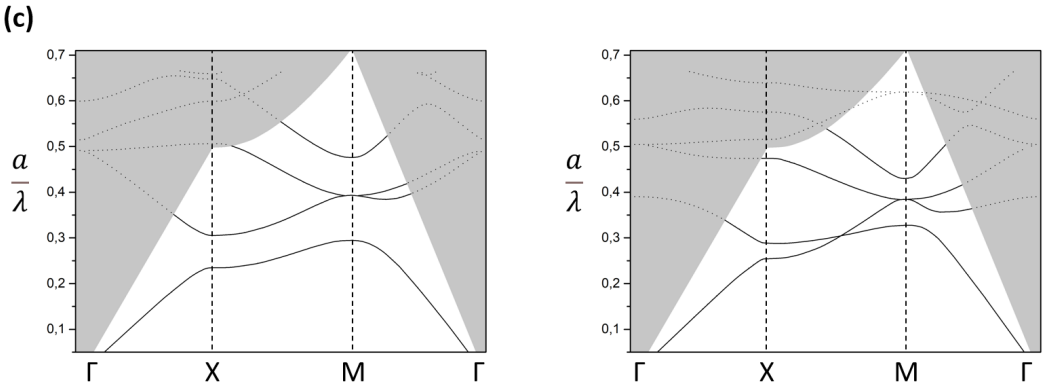

Figure A.10: Bandstructures for Si coated girdle bands (with the aforementioned conditions and immersed in water), displaying guided modes (solid lines), below the light cone, and modes that couple with radiation modes (dashed lines) in the light cone region. TE modes are displayed at the left and TM modes at the right. Coating thicknesses: (a) 6 nm, (b) 30 nm and (c) 60 nm.

B

Methods and preparation for measurements and additional work

Here are how some solutions were prepared, as well as some brief explanations on how the equipments used for measurements work. It is also prsented the poster presentation developed for the NASCADIA project.

B.1 Preparation of solutions

This Section talks about the prepare of some of the solutions that played a role throughout the Thesis, mainly in the frustule cleaning and surface functionalization protocols.

- **HCl**

  The HCl concentration available at the lab was of 37%, hence dilution was needed in order to prepare 10% HCl to carry out with the experiments. Using the dilution formula (Equation B.1)

  $$c_i v_i = c_f v_f \tag{B.1}$$

  where c_i is the initial concentration of solute (37 % HCl), v_i the initial volume of HCl to be used, c_f the final concentration (10% HCl) and v_f the volume of the diluted solution, the desired concentration was prepared, considering $v_f = 50$ ml and obtaining an initial volume $v_i = 13.5$ ml. The final volume is such that:

  $$v_f = \begin{cases} 13.5\text{ml HCl} \\ 36.5\text{ml MilliQ water} \end{cases} = 50\text{ml} \tag{B.2}$$

  The sample was then taken to a vortex /mixer for about 30 minutes at 500 rpm.

- **$KMnO_4$ and $(COOH)_2$**

  The preparation of $KMnO_4$ and $(COOH)_2$ solutions were similar. 8 grams of $KMnO_4$ were added to 100 ml of MilliQ water contained in a beaker, while 10 grams of $(COOH)_2$ were added to another

beaker containing 100 ml of MilliQ water as well. These solutions were then placed on a magnetic stirrer for 60-90 minutes.

- **TiO_2 NPs**

  The provided TiO_2 NPs in the citrate buffer had an initial concentration of 13 mg ml^{-1}. The protocol, however, reported the use of a concentration of 0.2 mg ml^{-1}. For simplification, the NPs solution was diluted in MilliQ water: an initial volume of 0.5 ml of NPs was used which, according to Equation B.1, the final volume of the diluted solution was

$$v_f = 32.5\text{ml} = \begin{cases} 0.5\text{ml of NPs} \\ 32.0\text{ml of MilliQ water} \end{cases} \tag{B.3}$$

  The sample was then put on a vortex/mixer for 90 minutes at 500 rpm.

B.2 Fourier Image Spectroscopy

The FIS setup used throughout is explained in Chapter 3, Subsection 3.1.5.1. Before proceding with the measurements themselves, several pictures of girdle bands were taken with 40x and 100x objective lenses, as well as multimode optical fibers with diameters of 50, 105 and 400 µm. Below, are the images taken with these components.

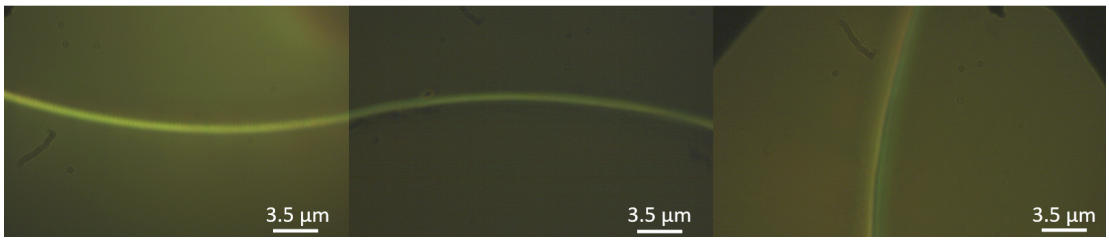

Figure B.1: Images of girdle bands taken with a 400 µm fiber and 100x oil immersion lens.

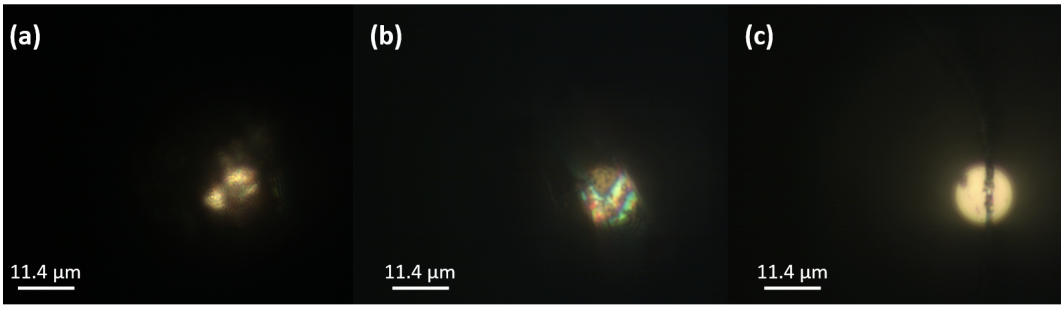

Figure B.2: Images of girdle bands taken with a 105 µm fiber and 40x objective lens.

B.3 Dynamic light scattering

Detection of scattered light from matter is a useful technique in the study of specific properties of macromolecules in a solution. Conventional DLS experiments use a monochromatic wave of light that shines on an exposed sample and a detector that receives the incoming signal, i.e. the scattered light [109], as depicted in Figure B.3. DLS measures the Brownian Motion of particles in a dispersion in order to

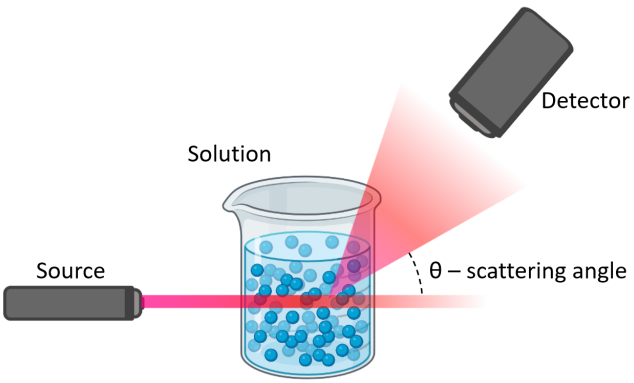

Figure B.3: Basic principle of a DLS measurement.

determine their hydrodynamic size. When incident light of some wavelength shines on particles staying still, the measured scattering intensity is constant. In a solution, however, the intensity of scattered light fluctuates over time due to the scattering of randomly diffusing particles, resulting in a fluctuating intensity signal. Several snapshots are taken rapidly one after another, in the range of ns-µs, and comparisons are constantly made with the original snapshot, in a process called auto-correlation and will generate an auto-correlation function. The further in time snapshots are, less similarities and therefore less correlation.

The generated auto-correlation function enables the extraction of diffusion coefficients, D, which are related to the hydrodynamic size of the particles by the Einstein-Stokes equation:

$$d_H = \frac{k_B T}{3\pi\eta D} \tag{B.4}$$

where d_H is the hydrodynamic size of the particles at a corresponding diffusion coefficient D, $k_B = 1.38 \times 10^{-23}\, m^2\, kg\, s^{-2}\, K^{-1}$ is the Boltzmann constant, T is the temperature and η the viscosity of the medium. DLS measurements were carried out at a temperature of 25°C, with a medium viscosity of 0.895 mPa.s.

B.4 Scanning electron microscopy and energy dispersive x-ray analysis

SEM, alongside EDX measurements, provided additional information about the composition of girdle bands and served to ensure that the modified samples had been successfully functionalized. A schematic of

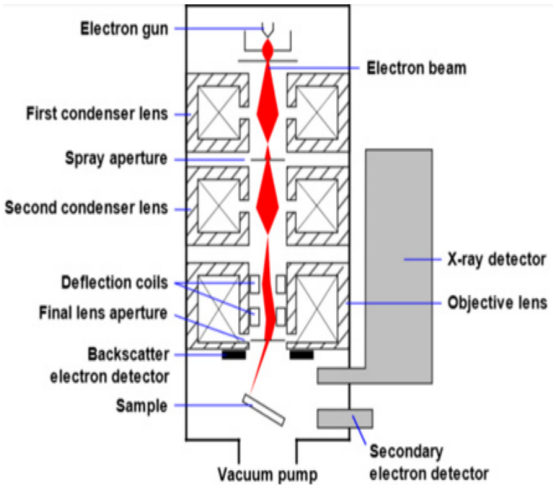

Figure B.4: Schematic of a scanning electron microscope. Reprinted from A. Mohammed *et al* [110].

the scanning electron microscope is displayed in Figure B.4, reprinted from A. Mohammed *et al* [110]. The electron gun is responsible for generating a high energy electron beam. The condenser lenses will decrease the beam spot, in order to produce sharper images, and direct it onto the sample. The electrons collected from the final lens interact with the sample itself and will generate the signals to produce an image. The coils are responsible for the raster-scanning of the sample, by moving the beam to discrete locations in the form of straight lines until a rectangular raster is produced on the surface. The interaction between the electron beam and the sample generates two types of electrons: secondary electrons (SE) and backscattered electrons (BSE). These are collected by their respective detectors. Both will be collected if the voltage on the collector is positive, whereas for negative voltage only backscattered electrons are collected. Figure B.5 shows two images of the same girdle band taken with SE, (a) and BSE, (b). BSE result in the elastic collision between electrons and atoms. An atom with a high atomic number scatters a higher number of electrons resulting in a higher signal. BSE help detect different phases in a specimen by providing imaging that carries information on its composition. SE result from collisions between the primary electron beam and the sample and have lower energy than BSE. These are more useful for topological analysis. The X-ray detector will collect the x-ray photons generated when the electron beam

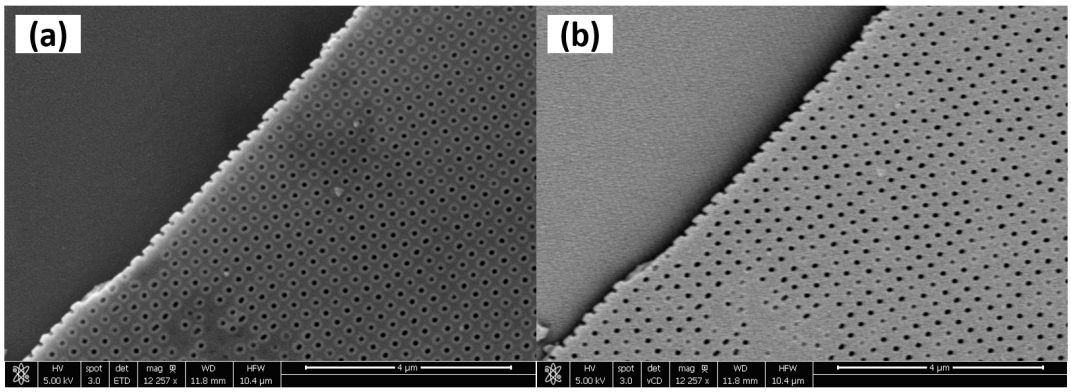

Figure B.5: SEM images with two types of electrons. (a) Secondary electrons. (b) Backscattered electrons.

penetrates and interacts with the volume beneath the surface of the specimen. These photons have particular energies to constituent elements of the analyzed specimen. The EDX detector separates the characteristic x-rays of various elements within the specimen into an energy spectrum, which is then analyzed by a computer software to determine the amplitude of a specific element. EDX serves as a tool to determine both qualitatively and quantitatively the chemical composition of a certain sample.

B.5 Plasma-enhanced chemical vapour deposition

PECVD is a chemical vapour deposition technique where chemical reactions occur after the creation of a plasma. Figure B.6.a shows a schematic of the inside of a PECVD machine. The plasma is created by an AC or DC discharge between two electrodes that ionize the mixture of the inert and reactant gases that fill the space between. The ionized molecules of the inert gas will help in the dissociation of the reactant gases, which in turn can react with other gas molecules or on the substrate material to form a new compound at the surface. The main reasons that lead to the choice of PECVD for the deposition of Si_3N_4 were its low working temperature (ranging from 250 to 350 ° C [111]) and the uniform and conformal depositions, with low porosity, that can be able to fit the complex and porous geometry of girdle bands. The process was also relatively quick, with the machine reaching a deposition rate of *ca.* 45 nm/min. Figure B.6.b shows the samples attached to a silicon wafer after the deposition.

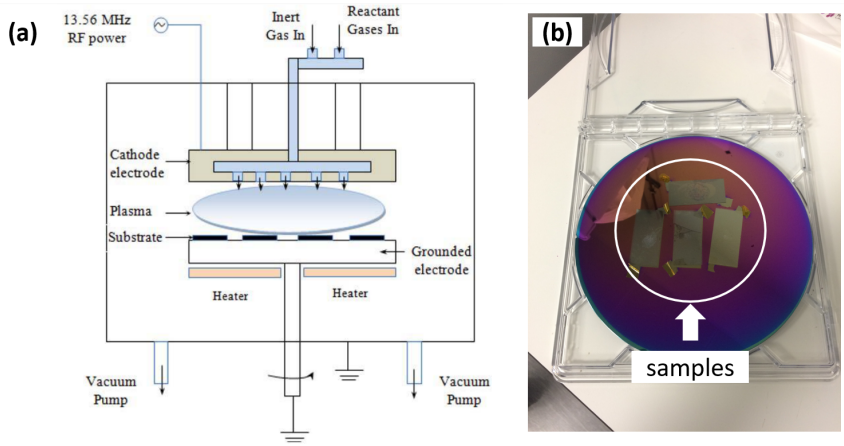

Figure B.6: (a) Schematic of a PECVD machine. Reprinted from [111]. (b) Samples in a silicon wafer after deposition.

B.6 Poster presentation

Below is the poster presentation developed and presented at the 12th Ibero-American Congress on Sensor, Ibersensor 2022, at the University of Aveiro.

MODIFICATION OF NATURAL PHOTONIC CRYSTALS BY TAILORING OF THE REFRACTIVE INDEX CONTRAST

Rafael Vilarinho[1], Rita Rocha[2], Vera Cardoso[2], Johannes W. Goessling[2], Martin Lopez Garcia[1],

[1]Natural and Artificial Photonic Structures and Devices Group, International Iberian Nanotechnology Laboratory, Av. Mestre José Veiga, Braga 4715-330, Portugal
[2] Centro de Estudos do Ambiente e do Mar (CESAM), Department of Biology, University of Aveiro, Campus de Santiago, Aveiro 3810-193, Portugal

Introduction

Photonic crystals (PhCs), nanostructures characterized by defined periodic wavelength-scale patterns, are commonly produced in cleanrooms involving precise nanofabrication techniques. Recent research confirmed that natural PhCs also exist in the silicon dioxide shells of diatoms, *i.e.* abundant microalgae that can precipitate silicic acid from water. The highly ordered natural lattices open photonic bandgaps with reproducible and well-defined spectral properties, enabling utilization as environmentally friendly photonic materials. Here we show the preparation and modification of the natural photonic structures, by tailoring refractive index contrast enabling a variety of applications including sensing by colorimetry or refractive index change detection.

Diatoms are living photonic crystals

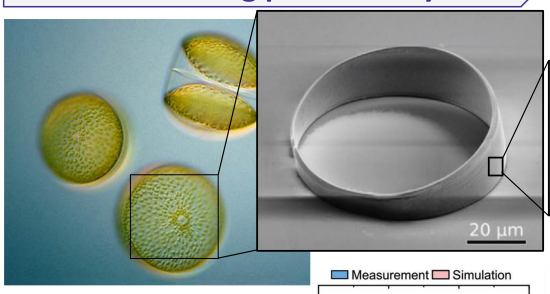

Diatom microalgae live in lakes and rivers. They precipitatate silicic acid forming silica exosqueletons called frustules, composed by valves and girdle bands.

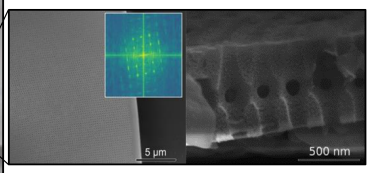

Girdles are circular silica slabs perforated with periodically separated pores arranged in various geometries, including square and hexagonal lattices.

The volume occupied by pores determine the effective refractive index of the sPhC. Tuning the refractive index contrast between the bulk and the immersion medium modifies the photonic response of the system.

Pore separation is defined by the lattice constant, which differs between diatom species, but is highly preserved for different indivudals of the same species [1].

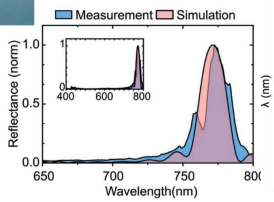

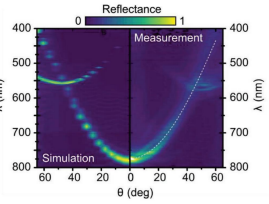

Main Goals

- ❑ Introduce diatom biosilica as biomaterial for light-harvesting applications
- ❑ Tunability via bio-silica doping with higher refractive index materials (*e.g.* TiO2)
- ❑ Eco-friendly and cost-effective alternative to nanofabricated photonic crystals

Effect of refractive index changes

FDTD simulations
Simulations of the photonic response for the doped structure are performed in the comercial tool Lumerical for the species *C. granii* with Si_3N_4 and TiO_2.

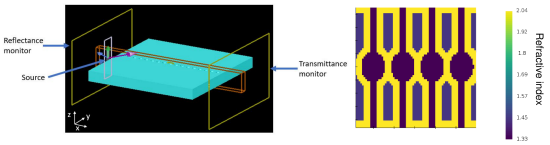

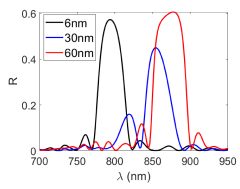

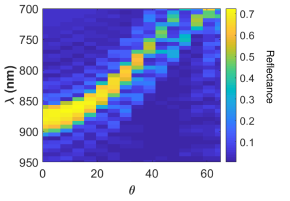

Sample preparation:
A full methodology for girdle band extraction and its preparation for photonics applications was developed earlier [2]

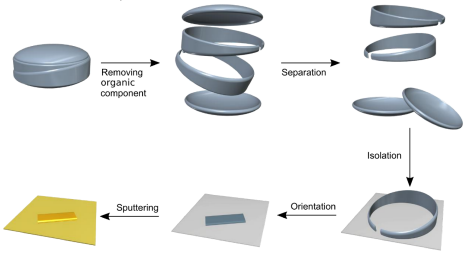

Deposition of thin-film materials will allow the tuning of the photonic properties according to the simulations

Key results

- ❑ Red-shift in the position of the bandgap and increase of its width as the refractive index contrast increases
- ❑ Deposition of 60 nm of Si_3N_4 and TiO_2 enhance light absorption
- ❑ Bandgaps located in the near infrared region (NIR)
- ❑ Sample processing methodology ready

Conclusions

- ❑ Tunability of natural photonic properties by tailoring the refractive index contrast, with doping of higher refractive index materials
- ❑ High availability of diatom species accounts for a larger use of biomaterials in light harvesting applications, serving as an alternative to cleanroom nanofabricated PhCs
- ❑ The red-shift of the photonic bandgaps opens the door for applications for the NIR such as gas sensing and telecommunication

References

[1] Johannes W. Goessling, William P. Wardley, and Martin Lopez-Garcia. "Highly Reproducible, BioBased Slab Photonic Crystals Grown by Diatoms". In: Advanced Science 7.10 (2020), p. 1903726.
[2] William P. Wardley, Johannes W. Goessling, and Martin Lopez-Garcia. Plasmonic crystals with highly ordered lattice geometries using continuous metal films on diatom bio-silica as both scaffolds and sources of tuneability. 2021
[3] Chien-Jang Wu, Ya-Chang Hsieh, and Heng-Tung Hsu. Tunable photonic band gap in a doped semiconductor photonic crystal in near infrared region. Progress In Electromagnetics Research, 114, 01 2011

Acknowledgements

The authors thank the Fundação para a Ciência e a Tecnologia for support through grant no. PTDCBTA-BTA20612021.